



UNIVERSIDAD NACIONAL AUTÓNOMA DE MÉXICO
POSGRADO EN CIENCIA E INGENIERÍA DE MATERIALES
INSTITUTO DE INVESTIGACIONES EN MATERIALES
ZERNIKE INSTITUTE FOR ADVANCED MATERIALS

FABRICATION AND CHARACTERIZATION OF ELECTROLUMINESCENT DEVICES
BASED ON METAL CHALCOGENIDES AND HALIDE PEROVSKITES

TESIS
QUE PARA OPTAR POR EL GRADO DE:
DOCTORA EN CIENCIAS E INGENIERÍA DE MATERIALES

PRESENTA:
M. en C. MARTHA JUDITH RIVERA MEDINA

DR. JUAN CARLOS ALONSO HUITRÓN
INSTITUTO DE INVESTIGACIONES EN MATERIALES

PROF.DR. MARIA ANTONIETTA LOI
ZERNIKE INSTITUTE FOR ADVANCED MATERIALS

DR. VOJTECH JANCIK
INSTITUTO DE QUÍMICA

DRA. ELSI VIOLETA MEJÍA URIARTE
INSTITUTO DE CIENCIAS APLICADAS Y TECNOLOGIA

CIUDAD DE MÉXICO SEPTIEMBRE 2021



Universidad Nacional
Autónoma de México



UNAM – Dirección General de Bibliotecas
Tesis Digitales
Restricciones de uso

DERECHOS RESERVADOS ©
PROHIBIDA SU REPRODUCCIÓN TOTAL O PARCIAL

Todo el material contenido en esta tesis esta protegido por la Ley Federal del Derecho de Autor (LFDA) de los Estados Unidos Mexicanos (México).

El uso de imágenes, fragmentos de videos, y demás material que sea objeto de protección de los derechos de autor, será exclusivamente para fines educativos e informativos y deberá citar la fuente donde la obtuvo mencionando el autor o autores. Cualquier uso distinto como el lucro, reproducción, edición o modificación, será perseguido y sancionado por el respectivo titular de los Derechos de Autor.

JURADO DE GRADO ASIGNADO

Dr. Juan Carlos Cheang Wong
Presidente

Dr. Juan Carlos Alonso Huitrón
Primer Vocal

Prof. Dr. Maria Antonietta Loi
Segundo Vocal

Dr. Mayo Villagrán Muniz
Tercer Vocal

Dra. Rosalba Castañeda Guzmán
Secretaria



rijksuniversiteit
 groningen

Fabrication and characterization of electroluminescent devices based on metal chalcogenides and halide perovskites

Proefschrift

ter verkrijging van de graad van doctor aan de
 Rijkuniversiteit Groningen
 op gezag van de
 Rector Magnificus prof. dr. C. Wijmenga
 en volgens besluit van het College voor Promoties

De openbare verdediging zal plaatsvinden op

vrijdag 9 juli 2021 om 11:00 uur

door

Martha Judith Rivera Medina

geboren on 2 juni 1989
 te Veracruz-Llave, Mexico

Promotores

Prof. dr. M.A. Loi

Prof. dr. J.C. Alonso-Huitrón

Beoordelingscommissie

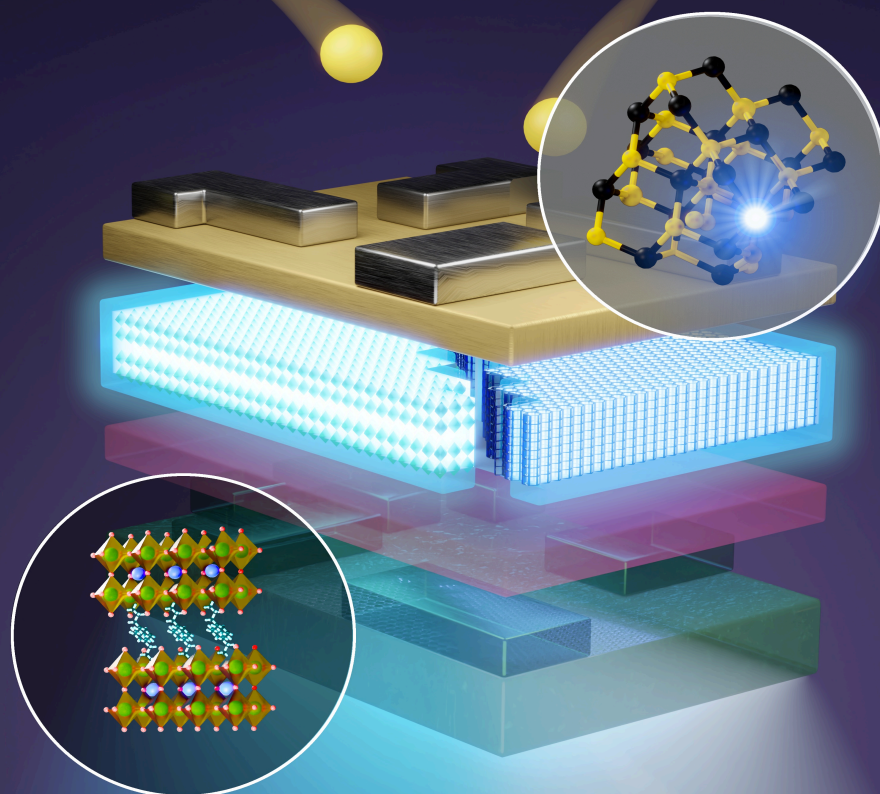
Prof. dr. P. Rudolf

Prof. dr. D. Solis-Ibarra

Prof. dr. R. Hildner

Prof. dr. G. Gigli

Fabrication and characterization of electroluminescent devices based on metal chalcogenides and halide perovskites



Martha Judith Rivera Medina

Thesis cover (printed version) used for the defense at the University of Groningen.

Al reverso se muestra la cubierta exterior utilizada para la versión impresa de la tesis por parte de la Universidad de Groninga. La figura representa un dispositivo electroluminiscente compuesto de una capa activa a base de un calcogenuro metálico (derecha) y perovskitas de haluro (izquierda). Al activar el dispositivo se puede observar la electroluminiscencia correspondiente a cada material dentro de la capa activa (blanco y azul).

El diseño de la cubierta exterior para el libro impreso fue realizado por Filiberto A. Bautista Moreno (The Figure Wizard).

La primera versión de la tesis fue impresa por la empresa Gildeprint en Países Bajos.

Este trabajo fue defendido públicamente ante un panel de expertos en el área, el día 9 de julio de 2021, en la Sala de Cermonias dentro del Edificio Académico de la Universidad de Groninga. Asimismo, fueron defendidas las siguientes ocho hipótesis académicas.

(Hipótesis académicas)

Stellingen

Behorende bij het proefschrift

Fabrication and characterization of electroluminescent devices based on metal chalcogenides and halide perovskites

Van

Martha Judith Rivera Medina

1. Europium can be reduced to its divalent state in a zinc sulfide matrix under aerobic conditions; its presence leads to broad-blue photoluminescence. (chapter 2)
2. White electroluminescence in an alternate-current device result upon the deexcitation of the excited levels of the luminescent centers and the intrinsic point defects residing close to the emissive – dielectric layer interfaces. (chapter 3)
3. Ruddlesden-Popper phases perovskites are good candidates as active layers to efficient green and blue light-emitting diodes. (chapter 4)
4. By carefully controlling the microstructure and the energetic landscape of Ruddlesden-Popper phases perovskites their photophysical properties are tuned, leading to enhanced performance in light-emitting diodes. (chapter 4)
5. “If I have seen further, it is by standing on the shoulders of giants.”
-Isaac Newton (1675)
6. Uncertainty is wrongly perceived as a moment of doubt disguised as fear and worry; the truth is, it can be a moment of reflection for new beginnings.
7. We are much more than the work we do every day. Letting our occupations define us completely can limit us, dilute our true potential, and hide our true selves.
8. Teamwork resembles a train, the engine helps the wagons to keep moving forward, and the wagons are held together by gears; if a gear is missing or malfunctioning, then its final destination is hampered.

Fabrication and characterization of electroluminescent devices based on metal chalcogenides and halide perovskites

Martha Judith Rivera Medina



university of
 groningen

faculty of science
 and engineering

zernike institute for
 advanced materials

Fabrication and characterization of electroluminescent devices based on metal chalcogenides and halide perovskites

Martha Judith Rivera Medina

PhD thesis

Zernike Institute PhD thesis series: 2021-17

ISSN: 1570-1530



CONACYT

Consejo Nacional de Ciencia y Tecnología

The work described in this thesis is a bilateral collaboration between Universidad Nacional Autónoma de México and University of Groningen for the obtainment of a double degree. The research activities were performed at both Instituto de Investigaciones en Materiales (Mexico City, Mexico) and at the Zernike Institute for Advanced Materials (Groningen, the Netherlands). This work was founded by CONACYT, UNAM, the Faculty of Science and Engineering (RUG), and the Executive Board of the University of Groningen.

*To my parents,
for their endless love and support.*

In memory of my grandmother.

Acknowledgments

I have received great support, assistance, advice, and encouragement from many people in the academic scene and personally, throughout my journey as a PhD student.

My first and foremost acknowledgments go to my supervisors, Prof. Dr. Maria A. Loi and Dr. Juan Carlos Alonso Huitrón. Both of you have supported and encouraged me along this journey and without your assistance this project could not be possible. I am grateful for it.

Maria, I have always admired your commitment to science. The way you are able to see *that* missing piece of the giant puzzle (science projects) is remarkable. Thanks for accepting me to be part of the Photophysics and Optoelectronics research group (POE) as my supervisor at the University of Groningen. You placed your trust and confidence in me to be the first PhD student to start investigating PeLEDs in your group. Even with such limited time, thanks to your help and support we achieved important results. I am sure that under your guidance even better results will be reached in the future. Your immense knowledge, productive work, your outstanding personality are truly inspirational to me.

Juan Carlos, I walked to your office as a master student candidate looking for a project in thin-film semiconductors; you asked me several questions about my academic curriculum and what kind of research I have performed for my bachelor's dissertation. You invited me to a meeting with Dr. Efrain to discuss the recent projects. I suggested few changes to the recipe according to my "*instintos en la química*" and they were correct. I started to work full-time in your group even before becoming an official master student, and later on, I continued as a PhD student. You gave me the tools and transmitted the confidence to freely explore my ideas, many of which ended up as bachelors' projects. I have certainly learned so much from you.

Special thanks to my tutor committee from UNAM, Dr. Vojtech (Beto) Jancik, and Dra. Elsi Violeta Mejía Uriarte. Your guidance during the first part of my PhD was exceptional. Beto, your enthusiasm for chemistry has always been contagious, and you have inspired me

tremendously. Thanks for sharing your knowledge in working with inert atmospheres when you agreed to share with me the secrets of your unique labs. Dra. Elsi, thanks for all the academic advice related to the photophysics of europium-based systems. I sincerely appreciate all your efforts dedicated to my PhD project.

I am thankful to the assessment committee members: Prof. dr. Petra Rudolf, Prof. dr. Diego Solis-Ibarra, Prof. Dr. Richard Hildner and Prof. Dr. Giuseppe Gigli for the time devoted in evaluating this thesis. Furthermore, I am grateful to the UNAM's Jury Members: Dr. Juan Carlos Cheang-Wong, Dr. Mayo Villagrán-Muniz, and Dra. Rosalba Castañeda-Guzmán for evaluating and revisited this booklet to improve its quality through their valuable corrections.

This work has received great help from many colleagues, collaborators, and technical support in both research groups.

To my colleagues at UNAM, Angélica, Benito, Jesus, Alonso, Lorenzo and Víctor: You rock, guys! I am very grateful to you for pulling off all the work that was still required for my projects in Mexico. Angélica, you supported me tremendously by managing all the last-minute experiments. Thank you! Benito 'el presidente', I've always admired your devotion to science, to go beyond the obvious of the problems. Thank you for helping me understand many mathematical equations by providing a physical meaning to them. I wish you the best in successfully completing your PhDs.

The technical and administrative staff at IIM-UNAM and grad-school of material science: I am very grateful for the technical support of Adriana Tejada, Omar Novelo, Josue Romero, Damaris Cabrero, Carlos Flores, Miguel Angel Canseco, Fernando Silvar, Jose Barreto, Roberto Hernández, Samuel Tehuacanero, Dr. Carlos Magaña, Manuel Aguilar. Additionally, a special thanks to Benito and Erika for their contribution in designing and programming the colorimetric software that I needed. To my beloved secretaries: Diana Arias, Esther Carrillo, Isabel Gomez, and María Luisa Resendiz: your patience is incredibly remarkable when handling administrative (bureaucratic) work. Dr. Heriberto Pfeiffer and Dr. Luis Sansores, coordinators of the material science program who were involved in the process by representing the grad school: thank you.

Furthermore, I am very grateful to the Coordinación General de Estudios de Posgrado for all the international management into my double-degree process.

My story in Groningen begins at the end of June 2017, when I did a short stay as a visiting student. Jorge was so kind to give me the lab tour. At that time, I met Vlad, Irene, Honghua, Luna, and Daniel. One year and a half later, I officially became a PhD student at RUG. Musty and Sampson immediately welcomed me by inviting me to have lunch outside. We repeated this activity many times, accompanied by pleasant discussions about life and future plans. I had the opportunity to work with Qingqian and Kush under the supervision of Shuyan, guiding me at the beginning of my project at RUG. Simon, Herman and Eelco: thank you for all the hours spent in the laser lab measuring my samples. Dima and Natasha, thanks for letting me know you better outside of the academic world. We spent memorable evenings having either a Mexican dinner, a borsh, or a delicacy from Natasha. I wish you all the best in your forthcoming projects.

Matteo, our discussion about perovskites seems to be endless. We can spend hours speaking about science, cleanroom issues, electronics, chemistry and Italian food. Thanks for accepting to be my dancing partner; I really enjoyed our time hopping along with Natasha. Wytse, thanks for helping in all matters related to IT and Dutch culture. You and Crystal became a true family for me (including the kitties), and definitely, few lines are not enough to express my gratitude. Now it is official: you are one of my paranympths! Lorenzo, you are the exception regarding knowing device fabrication and spectroscopy characterization. I'd call it the whole. Dr. Di Mario, as I usually referred to you, we began to collaborate at the end of my PhD, and you came to support me on those specific questions I had in spectroscopy. I am greatly indebted to you. Nonetheless, our collaboration is not restricted to work, but also to personal matters. Thank you for allowing me to know the great human being you are.

To all of the group members (past and present): Artem, Azi, Vicent, Marten, Nutifafa, Karolina, Jacopo, David, Jiale, Riccardo, Jun, Lijun, Bart, Unnati, Xuwen: thank you for all gratifying conversations and my best wishes in your research projects (or future careers). To the students whom I had the privilege to supervise at UNAM and RUG: thank you. I have definitely learned from you.

Special thanks to Prof. Andrea Mura, Prof. Loredana Protesescu, and Prof. Giuseppe Portale for all the support given to my project at RUG.

Building a new characterization setup from scratch requires constant technical assistance. Teo and Arjen (my lovely technicians), this could not be possible without your help. Renate, Jeannette and Annelies were always very supportive in many local administrative affairs. Joyce, Fiorella, Prof. Petra Rudolf, Luis (RUG member at UNAM), and those I did not have the opportunity to personally meet, thank you so much for your constant support in international subjects regarding bilateral collaboration in double-degree obtainment!

This PhD project could not be tangible without the financial support of the Mexican Government through CONACYT under Beca Nacional and Beca de Movilidad, PAEP-UNAM, PAPPIT-UNAM (IG100614-2), the University of Groningen, and the Faculty of Science and Engineering.

Last but not least to my dearest families in Mexico and the United States: my deep and sincere gratitude to you. Your unparalleled love and support have always been my source of encouragement to keep going. Having two families is the most rewarding incident of my life. Double the love!

Mamá, mi más grande guerrera. Gracias por demostrarme que poder es querer y si lo quieres a por ello. ¡Lo logramos! El momento que me enteré de tu diagnóstico fue la noticia más devastadora que he recibido; pero tu valentía, tu amor a la vida, me daban esas fuerzas que ni yo sabía que tenía. Espero disfrutarte muchos años más. Papá, gracias por siempre apoyarme en cada uno de mis proyectos. Eres fuente de inspiración para mi y esto es producto de tus enseñanzas a lo largo de mi vida.

A mi familia en Groningen: Antonio y Gerardo. Mudarte a un país nuevo siempre requiere de mucho esfuerzo, pero unidos logramos hacer una pequeña familia. Tantas aventuras vividas, charlas, noches de película, platillos mexicanos, reuniones con amigos, tardes de pláticas con

un buen vino, son algunas de nuestras actividades y resume la gran armonía que era vivir con ustedes.

Thank you,

Bedankt,

Gracias,

Martha Judith Rivera Medina

Groningen, the Netherlands

June 2021 (edited August 2021)

Table of Contents

List of Figures	i
List of Tables	v
Summary	vii
Resumen	xi
Samenvatting	xv
Motivation & Objectives	3
1. Introduction	7
1.1 Electroluminescence	8
1.2 Light-emitting devices	9
1.2.1 p-n junction	9
1.2.2 p-i-n junction	13
1.2.3 Thin-film electroluminescent devices (TFEL devices)	15
1.3 Materials for light emission	17
1.3.1 Metal chalcogenides matrices	17
1.3.2 Metal halide perovskites	21
1.4 Devices characterization	23
1.4.1 Colorimetry	23
1.4.2 External quantum efficiency and Luminous power	26
1.5 Thesis outline	29
1.6 References	32
2. A chalcogenide-based phosphor: Europium-doped ZnS nanocrystalline thin films with strong blue PL	37
2.1 Introduction	38
2.2 Experimental section	39
2.2.1 Preparation of the thin films	39
2.2.2 Characterization of the thin films	39
2.3 Results and discussion	40
2.3.1 Film growth	40
2.3.2 Structure, morphology and chemical composition	43
2.3.3 Optical properties	47
2.4 Conclusions	50
2.5 References	51

3. AC-driven electroluminescent devices: White-emission from the phosphor ZnS:Eu	57
3.1 Introduction	58
3.2 Experimental section	59
3.2.1 Materials, ultrasonic spray coating conditions, and device fabrication	59
3.2.2 Characterization of the thin films and MISIM devices	60
3.3 Results and discussion	61
3.3.1 Device structure and composition	61
3.3.2 EL modulation and colorimetric characteristics	62
3.3.3 Origin of the white emission	67
3.4 Conclusions	69
3.5 References	70
4. Metal-halide perovskites as emitters: Bright blue-emitting PeLED through the incorporation of small spacer cation	75
4.1 Introduction	76
4.2 Experimental section	77
4.2.1 Chemicals	77
4.2.2 Preparation of thin films	78
4.2.3 Optical spectroscopy	78
4.2.4 Structural measurements	79
4.2.5 Fabrication of the PeLEDs	80
4.2.6 Characterization of the PeLEDs	80
4.3 Results and discussion	81
4.3.1 Perovskite active layer and their physical properties	81
4.3.2 Charge carrier dynamics	86
4.3.3 Structural and morphological characterizations	93
4.3.4 Device performance	98
4.4 Conclusions	102
4.5 References	104
Curriculum Vitae	107

List of Figures

Figure 1.1	(a) Schematic illustration of a p-n junction diode at equilibrium conditions and (b) the diode symbol as represented in electronics	11
Figure 1.2	Band model of a p-n junction (top) and representation of its electric field and net potential (bottom) at (a) equilibrium conditions, (b) forward bias, and (c) reverse bias. At equilibrium conditions, the net charge flow is balanced at the depletion region, when a forward bias is applied the energy barrier decrease prompting a current to flow. The opposite behavior occurs when a reverse bias is applied	12
Figure 1.3	Schematic illustration of a p-i-n junction diode and (b) the diode symbol as depicted in electronics	14
Figure 1.4	Band gap model for p-i-n junction diode. At forward bias, heavily doped semiconductors begin to inject charge carriers towards the intrinsic region, allowing charges to recombine	14
Figure 1.5	TFEL devices band diagram and working principle. Interface full circles are occupied traps, whereas hollow circles are empty traps. Tunneling is followed by an acceleration of the trapped electrons promoting impact-excitation in the luminescent centers (empty squares) and an avalanche process in the phosphor layer. Re-trapping will occur at the opposite dielectric interface	16
Figure 1.6	Zinc blende (left) and wurtzite (right) structures of ZnS	18
Figure 1.7	The symmetry of the Mn^{2+} ions in ZnS	20
Figure 1.8	Schematic representation of AMX_3 metal halide perovskite crystal	22
Figure 1.9	From left to right: Ruddlesden Popper (RP) phase $n=1$, Quasi -2D RP phases $\langle n=2 \rangle$, and $\langle n=3 \rangle$, 3D perovskite crystal	22
Figure 1.10	Luminous efficacy curve of the human eye with photopic vision	25
Figure 1.11	The CIE 1931 space chromaticity diagram. The color coordinates of a sample are represented by (x_s, y_s) . The locus curve contains all the possible hue wavelengths, where the dominant wavelength can be extracted (x_d, y_d) . All qualitative color measurements are measured with respect to an illuminant with coordinates (x_i, y_i)	26

Figure 1.12	Example of typical J-V-L curve in semi-logarithmic scale. It pictures the relationship of the density current flowing through the device and the luminous power as function of the voltage applied across the LED	28
Figure 2.1	TG-DTG curves for the (a) 1,3-Dimethyl-2-thiourea; (b) zinc acetate dihydrate and (c) europium (III) chloride hexahydrate precursors, evaluated at 10 and 20 °C/min heating rate for a,b and c, respectively. The measurements were carried out in a dry air atmosphere	41
Figure 2.2	X-ray diffraction patterns for the ZnS and ZnS:Eu ²⁺ films, as deposited by ultrasonic spray pyrolysis, at substrate temperature of 450 °C	44
Figure 2.3	SEM micrographs for the ZnS and ZnS:Eu ²⁺ films deposited by USP. Top row: ZnS film (a) planar view and (b) cross view with a rotation of 188.4° and 6.1° of tilt angle. Bottom row: ZnS:Eu ²⁺ film (c) planar view and (d) cross view with a rotation of 94.6° and 8.0° of tilt angle	45
Figure 2.4	Electron spin resonance (ESR) spectrum of the ZnS:Eu ²⁺ film measured at 113 K (-160°C) using a resonance frequency of 9.1 GHz and a magnetic field centered at 330 mT. The ESR line of Eu ²⁺ is observed at 325.2 mT	46
Figure 2.5	Optical characteristics of ZnS:Eu ²⁺ and ZnS. (a) UV-vis absorbance spectra. The inset shows the absorbance spectrum for Eu ²⁺ . (b,c) Photographs of ZnS and ZnS:Eu ²⁺ thin films being excited with a UV radiation of 254 nm, in a bright and dark room, respectively. (d) Steady-state PL for both films with an excitation wavelength of 325 nm. The inset shows a close-up for the ZnS film. (e) Steady-state PL for ZnS:Eu ²⁺ at different excitation energies and PLE with λ_{em} of 455 nm is displayed in the inset	47
Figure 2.6	Simplified energy band and energy levels diagram for Eu ²⁺ ions incorporated in ZnS films	50
Figure 3.1	(a) Illustration of the AC-TFEL MISIM device fabricated by ultrasonic spray pyrolysis. (b) Cross-sectional image of the structure showing layer-by-layer stacking	61
Figure 3.2	EL spectra of one of our AC-TFEL device incorporating ZnS:Eu ²⁺ as phosphor. The rms-voltages are: V ₁ =56 V, V ₂ =70 V, and V ₃ =77 V. A photograph of our working device is display on the top right corner	62

Figure 3.3	CIE chromaticity diagram of the color space coordinates of our AC-TFEL device. (a) Variation of the color coordinates as function of V_1 , V_2 , and V_3 rms-voltages with respect to the D65 illuminant. (b) Dotted line traced for the determination of the colorimetric properties at an applied rms-voltage of V_3	62
Figure 3.4	Normalized EL spectra of D65 illuminant and the three EL spectra at the corresponding operating rms-voltages of $V_1=56$ V, $V_2=70$ V, and $V_3=77$ V	66
Figure 4.1	Schematic illustration of $\langle n=2 \rangle$ perovskite used as the active layer of the blue PeLED. On the left side is depicted the composition $\text{PEA}_2(\text{Cs}_{0.75}\text{MA}_{0.25})\text{Pb}_2\text{Br}_7$ [neat] and on the right side the composition $\text{PEA}_2(\text{Cs}_{0.75}\text{MA}_{0.25})\text{Pb}_2\text{Br}_7:\text{iPAm}$ obtained using isopropylammonium [iPAm] as an additive	81
Figure 4.2	Steady-state optical characteristics of 3D ($\text{Cs}_{0.75}\text{MA}_{0.25}\text{PbBr}_3$), 2D ($\text{PEA}_2\text{PbBr}_4$), and quasi-2D perovskites deposited on quartz substrates. Absorbance (Abs) and photoluminescence (PL) spectra of thin films of different nominal $\langle n \rangle$ value for neat (a) and iPAm-modified (b) perovskites	83
Figure 4.3	Photoluminescence characteristics of $\langle n=2 \rangle$ thin films deposited on quartz and PEDOT:PSS. (a) PL spectra of the $\langle n=2 \rangle$ [neat] films, and of (b) of iPAm-modified ones. (c) influence of PEDOT:PSS on neat (green color) and iPAm-modified films (blue color), and (d) PLQYs for the two samples on PEDOT:PSS	85
Figure 4.4	Time-resolved photoluminescence (TRPL) of $\langle n=2 \rangle$ thin films deposited on PEDOT:PSS. PL spectra at different times after excitation of (a) neat film and (b) films with the addition of iPAm. PL decays measured at different wavelengths, corresponding to the emission of different N-phases, in (c) neat film and (d) film with the addition of iPAm	87
Figure 4.5	Fast transient absorption spectroscopy (FTAS) characterization of $\langle n=2 \rangle$ thin films deposited on PEDOT:PSS. Transient spectra at different delay times between pump and probe for (a) neat film and (b) film with the addition of iPAm. Time dependence of the normalized FTAS signal at different wavelengths, corresponding to the main absorption bleaching features on the spectra, for (c) neat film and (d) film with the addition of iPAm: experimental data (colored dots) and best fitting models (colored lines)	90

Figure 4.6	SEM and AFM micrographs of nominal $\langle n=2 \rangle$ samples. SEM micrographs of the (a) neat perovskite and (b) iPAm-modified films. The insets show magnification of the surface morphology. AFM micrograph of (c) neat film (scan size of $10 \mu\text{m} \times 10 \mu\text{m}$) and (d) iPAm-modified film (scan size of $5 \mu\text{m} \times 5 \mu\text{m}$). On the right-side of (d) is shown a zoom-in of the iPAm film (size $2 \mu\text{m} \times 2 \mu\text{m}$)	94
Figure 4.7	Powder X-ray diffraction patterns (XRD) of 2D and nominal $\langle n=2 \rangle$ layered perovskite thin films for neat and iPAm films. (a, b) Films deposited on quartz (c,d) and on PEDOT:PSS	95
Figure 4.8	GIWAXS patterns of thin films of (a) $\text{PEA}_2\text{PbBr}_4$, (b) $\text{PEA}_2(\text{Cs}_{0.75}\text{MA}_{0.25})\text{Pb}_2\text{Br}_7$, (c) $\text{PEA}_2\text{PbBr}_4$:i-PAm and (d) $\text{PEA}_2(\text{Cs}_{0.75}\text{MA}_{0.25})\text{Pb}_2\text{Br}_7$:iPAm deposited on PEDOT:PSS	96
Figure 4.9	Comparison of the GIWAXS intensity cuts along the quasi vertical qz direction for the 2D and the $\langle n=2 \rangle$ thin films without and with the iPAm addition.....	97
Figure 4.10	Schematic illustration of the structure of the perovskite LED (a) and the energy level alignment of the materials composing the device structure (b)	99
Figure 4.11	Performance of PeLEDs. (a) CIE color coordinates of different types of devices investigated (b) JVL curves of one the best performing devices (c) EL of PeLEDs using as emissive layer $\langle n=2 \rangle$ neat and with iPAm the spectra are recorded with the device bias at 7V, (d) EL spectra of the blue-emitting LED at different bias, and (e) current efficiency of $\langle n=2 \rangle$ neat and with iPAm PeLEDs	101

List of Tables

Table 3.1	CIE photometric and colorimetric characteristics of one of our AC-TFEL devices at operating rms-voltages: $V_1=56$ V, $V_2=70$ V, and $V_3=77$ V using the D65 illuminant as reference	64
Table 4.1	Photoluminescence peaks. Peak position and FWHM of the main emission signals in the steady state PL spectra reported in Figure 4.3. The values are obtained fitting the spectra with multiple gaussians components	85
Table 4.2	PL lifetimes obtained by fitting with a multi-exponential decay function the time-resolved PL signal at different wavelengths for both neat and iPAm-modified films. For the film with the additive signals at 475, 491 and 510 nm show a long tail with a decay much longer than the time range of the measurements	88
Table 4.3	FTAS fit results. Time constants obtained by fitting the dynamics of the main absorption bleaching features on the transient absorption spectra of both neat and iPAm-modified films. Signals fitted by a combination of exponential rising (τ_R) and decays (τ_1 , τ_2 and τ_3). Errors are evaluated considering the instrument response function of the experimental setup and the parameters used for the measurements	91
Table 4.4	Colorimetric characteristics for neat and iPAm-modified PeLEDs using as reference the standard illuminant E	102

Summary

The imperative quest for efficient self-emissive displays and large-area illumination technologies has led the scientific community to investigate novel and promising semiconductors for the so-called next generation of solid-state light-emitting devices. The standardized requirements to fulfill for the next generation of light-emission technology strongly depend on the application. For instance, a better color gamut and viewing angles are necessary for display technology; whereas, large-emitting areas resembling natural daylight without sacrificing brightness are essential in illumination. The overall performance of light-emitting devices relies upon many variables, including materials, fabrication processes, and device architecture. Hence the synthesis and characterization of the semiconductor material together with a study of its implementation in electroluminescent devices are just a first, but still fundamental, step towards possible future commercialization of a novel light-emitting technology.

Despite the great advances already made in the forthcoming generation of displays and illumination devices, there are still challenges to be addressed. The manufacturing cost for self-emissive displays and illumination technologies is considerably high and increases rapidly as the active area becomes larger since expensive fabrication techniques are presently required. Low-cost manufacturing processes, i.e., those based on solution methods, are a promising alternative to the current technology. While efficient green and red light-emitting devices have been obtained by solution-processable methods, even in large areas, the performance of the blue-emitting devices is still lagging behind due to the difficulty to achieve defect-free semiconductors with such a wide bandgap. The lack of efficient blue emitters has hampered the progress for full-color displays (or has required creative solutions as in OLED displays) and white-emitting illumination sources. For the above reasons, intense research is going on to fabricate efficient blue-emitting inorganic and hybrid semiconducting materials by solution-processable methods.

This thesis focuses on fabricating two prospective blue luminescent semiconductors prepared by low-cost techniques and their application in multilayered electroluminescent devices, namely thin-film electroluminescent devices and light-emitting diodes.

Thin-film electroluminescent devices (TFEL) are comprising of a phosphor between two insulating layers and contacted by front and rear electrodes, of which one has to be transparent for the light to scape. Thus, it is arranged in a MISIM (metal-insulator-semiconductor-insulator-metal) structure. The phosphor is a wide band gap semiconductor that serves as a host material for impurities, namely color centers. They are activated upon the application of an alternating voltage with the delivering of a constant light emission at high electric fields. In **chapter 2**, we present the synthesis of a phosphor based on a well-known metal chalcogenide semiconductor doped with europium chloride (III). Herein, zinc sulfide (ZnS), in its wurtzite crystal structure, was ultrasonically pyrolyzed (pyrosol) on top of glass substrates forming a dense thin film. By carefully controlling the synthesis of the europium-doped ZnS films, we were able to reduce our europium source to its divalent state forming europium sulfide (EuS) bonding. The presence of divalent europium (Eu^{2+}) was confirmed by EPR spectroscopy. Eu^{2+} is responsible for the broad-blue band photoluminescence when is excited with an energy of 3.75 eV, i.e., the band gap of the ZnS:Eu^{2+} . The emission mechanism is governed by $5d \rightarrow 4f$ transitions of the Eu^{2+} first excited state.

In **chapter 3**, we present results after the incorporation of our phosphor material in TFEL devices. We used zirconium oxide (ZrO_2) as insulating layers due to its relatively high κ -dielectric constant, and antimony-doped tin oxide (ATO) and aluminum as transparent and metallic electrodes, respectively. The device was fabricated using a low-cost, relatively fast, and straightforward spray pyrolysis technique. White-emitting electroluminescence is the result of the application of an alternating voltage at a fixed 10kHz sinusoidal frequency. We analyzed the colorimetric characteristics of the white light by modulating the square root of the mean (rms) AC-voltage spanning from a range of 56 V up to 77 V. The resultant white light at 77 V is

comparable to the CIE illuminant D65, which correspond to the standard illumination of natural noon daylight in many countries in Northwestern Europe. The origin of the white emission was speculated to arise from a contribution of the bulk phosphor material, impurities of Eu^{3+} in built-in ZnO sublayers due to the inherent pyrosol process, and intrinsic defects upon the formation of these sublayers.

Light-emitting diodes (LEDs) are, as par excellence, the most studied devices for illumination applications. Contrary to TFEL, LEDs operate by direct voltage and relatively low electric fields. The emission color is directly determined by the energy of the band gap of the semiconductor. In a p-i-n structure, holes and electrons are injected into the intrinsic layer, namely, the emissive semiconductor, to prompt radiatively recombination of charges. In **chapter 4**, we fabricated LEDs using hybrid metal halide perovskites, which are promising hybrid semiconductors for optoelectronic applications. We used a quantum-confined system provided by 2D-3D Ruddlesden-Popper perovskites phases (RP), which allow us to tune the band gap toward the blue, further enhancing its quantum yields (PLQYs) compared to its purely 3D counterparts. Nonetheless, this approach has inherent inconveniences regarding control phase distribution and their orientation to favor charge transport in a light-emitting diode. Consequently, an ideal situation will require both parameters to be in a good agreement to guarantee a blue emission without sacrificing the transport of holes and electrons to the recombination region. We fabricated perovskites-based light emitting-diodes (PeLEDs) using an active layer of nominal composition $\text{PEA}_2(\text{Cs}_{0.75}\text{MA}_{0.25})\text{Pb}_2\text{Br}_7$, which we compare to active layers incorporating isopropylammonium (iPAm) as an additive. A device structure comprising ITO/PEDOT:PSS/perovskite/TPBi/LiF/Al was used. Our results show a bright blue-emitting (493 nm) device with luminance as high as 8260 cd m^{-2} at an applied bias of 6.5 V (20.6 mA cm^{-2}). The colorimetric characteristics were also assessed, showing a high color purity of 88% for our champion device. Furthermore, an intriguing external quantum efficiency of up to 6% was reached. PLQYs of 64%, on average, were achieved when the active layer with the addition of iPAm was deposited on PEDOT:PSS substrates (as in the PeLED structure), a 3-fold enhancement compared to the neat $\text{PEA}_2(\text{Cs}_{0.75}\text{MA}_{0.25})\text{Pb}_2\text{Br}_7$ system. Optical and structural investigations were performed to unveil such behavior, indicating that RP of predominantly $n=3$

domains are surrounded by higher dimensionality phases, localizing the radiative recombination in very small crystalline domains with random orientation; thus, benefiting the PeLEDs performances.

Resumen

La búsqueda imperativa de pantallas autoemisivas eficientes y tecnologías de iluminación de gran superficie ha llevado a la comunidad científica a investigar semiconductores novedosos y prometedores para la llamada próxima generación de dispositivos emisores de luz de estado sólido. Los requisitos estandarizados que deben cumplirse para la próxima generación de tecnología de emisión de luz dependen en gran medida de la aplicación. Por ejemplo, una mejor gama de colores y ángulos de visión, son necesarios para la tecnología de visualización; mientras que áreas de mayor tamaño de emisión que se asemejan a la luz natural del día, sin sacrificar el brillo, son esenciales en la iluminación. El rendimiento general de los dispositivos emisores de luz depende de muchas variables, incluidos los materiales, los procesos de fabricación y la arquitectura del dispositivo. Por lo tanto, la síntesis y caracterización del material semiconductor junto con un estudio de su implementación en dispositivos electroluminiscentes son solo un primer paso, pero aún fundamental, hacia la posible comercialización futura de una nueva tecnología de emisión de luz.

A pesar de los grandes avances que ya se han logrado en la próxima generación de pantallas y dispositivos de iluminación, aún quedan desafíos por abordar. El costo de fabricación de las tecnologías de iluminación y pantallas autoemisivas es considerablemente alto, y aumenta rápidamente a medida que el área activa aumenta, ya que actualmente se requieren técnicas costosas de fabricación. Los procesos de fabricación de bajo costo, es decir, aquellos basados en métodos de solución, son una alternativa prometedora a la tecnología actual. Si bien se han obtenido dispositivos eficientes con emisión en el verde y de luz roja mediante métodos procesables en solución, incluso en áreas extensas, el rendimiento de los dispositivos emisores de luz azul todavía está rezagado debido a la dificultad de lograr semiconductores sin defectos con una banda prohibida tan amplia. La falta de emisores azules eficientes ha obstaculizado el progreso de las pantallas a todo color (o ha requerido soluciones creativas como en las pantallas OLED) y fuentes de iluminación

que emiten luz blanca. Por las razones anteriores, se está llevando a cabo una intensa investigación para fabricar materiales semiconductores híbridos e inorgánicos eficientes que emitan luz azul mediante métodos procesables en solución.

Esta tesis se centra en la fabricación de dos prospectivos semiconductores luminiscentes azules preparados mediante técnicas de bajo costo y su aplicación en dispositivos electroluminiscentes multicapa, a saber, dispositivos electroluminiscentes de película delgada y diodos emisores de luz.

Los dispositivos electroluminiscentes de película delgada (TFEL por sus siglas en inglés) están compuestos por un fósforo entre dos capas aislantes y electrodos delantero y trasero, de los cuales uno tiene que ser transparente para que la luz escape. Así, el dispositivo se agrupa en una estructura MISIM (metal-aislante-semiconductor-aislante-metal). El fósforo es un semiconductor de banda ancha que sirve como material anfitrión de impurezas, es decir, centros luminiscentes. Se activan mediante la aplicación de un voltaje alterno con la entrega de una emisión de luz constante bajo campos eléctricos elevados. En el **capítulo 2**, presentamos la síntesis de un fósforo basado en un conocido semiconductor de calcogenuro metálico dopado con cloruro de europio (III). Aquí, el sulfuro de zinc (ZnS), en su estructura cristalina de wurtzita, fue pirolizado ultrasónicamente (pirosol) sobre sustratos de vidrio, formando una película delgada y densa. Al controlar cuidadosamente la síntesis de las películas de ZnS dopadas con europio, pudimos reducir nuestra fuente de europio a su estado divalente formando enlaces de sulfuro de europio (EuS). La presencia de europio divalente (Eu^{2+}) fue confirmada por espectroscopia EPR. Eu^{2+} es responsable de la fotoluminiscencia azul de banda ancha cuando se excita con una energía de 3,75 eV, en otras palabras, la banda prohibida de ZnS: Eu^{2+} . El mecanismo de emisión está gobernado por transiciones $5d \rightarrow 4f$ del primer estado excitado de Eu^{2+} .

En el **capítulo 3**, presentamos los resultados tras la incorporación de nuestro material de fósforo en los dispositivos TFEL. Usamos óxido de circonio (ZrO_2) como capas aislantes debido a que tiene una constante dieléctrica κ relativamente alta; y óxido de estaño dopado con antimonio (ATO) y aluminio como electrodos transparentes y metálicos,

respectivamente. El dispositivo se fabricó utilizando la técnica de rocío pirolítico, cuya es de bajo costo, relativamente rápida y sencilla. Se obtuvo emisión electroluminiscente blanca bajo la aplicación de un voltaje alterno a una frecuencia sinusoidal fija de 10 kHz. Analizamos las características colorimétricas de la luz blanca modulando la raíz cuadrada del voltaje (rms) de CA (corriente alterna) que abarca desde un rango de 56 V hasta 77 V. La luz blanca resultante a 77 V es comparable al iluminante CIE D65, que corresponde a la iluminación estándar de la luz natural del mediodía en muchos países del noroeste de Europa. Se especuló que el origen de la emisión blanca surgía de una contribución del Eu^{2+} incorporado en el material fosfor, Eu^{3+} en las subcapas de ZnO incorporadas debido al proceso de pirosol inherente y defectos intrínsecos en la formación de estas subcapas.

Los diodos emisores de luz (LEDs por sus siglas en inglés) son, por excelencia, los dispositivos más estudiados para aplicaciones de iluminación. A diferencia de los TFELs, los LEDs funcionan con voltaje directo y campos eléctricos relativamente bajos. El color de emisión está directamente determinado por la energía de la banda prohibida del semiconductor. En una estructura p-i-n, se inyectan huecos y electrones en la capa intrínseca, es decir, el semiconductor emisor, para provocar la recombinación radiativa de cargas. En el **capítulo 4**, fabricamos LEDs utilizando perovskitas híbridas de haluro metálicos, que son semiconductores híbridos prometedores para aplicaciones optoelectrónicas. Usamos un sistema confinado cuántico proporcionado por fases de perovskitas de Ruddlesden-Popper (RP) 2D-3D, que nos permiten ajustar la banda prohibida hacia el azul, mejorando aún más sus rendimientos cuánticos (PLQY) en comparación con sus contrapartes 3D. No obstante, este enfoque tiene inconvenientes inherentes con respecto al control en la distribución de la fases y su orientación para favorecer el transporte de carga en un diodo emisor de luz. En consecuencia, una situación ideal requerirá que ambos parámetros estén de acuerdo para garantizar una emisión azul sin sacrificar el transporte de huecos y electrones a la región de recombinación. Fabricamos diodos emisores de luz (PeLED) a base de perovskitas utilizando una capa activa de composición nominal $\text{PEA}_2(\text{Cs}_{0.75}\text{MA}_{0.25})\text{Pb}_2\text{Br}_7$, que comparamos con capas activas cuando se incorpora el isopropilamonio (iPAm) como aditivo. Se utilizó una estructura de dispositivo que comprende ITO / PEDOT: PSS / perovskita / TPBi / LiF / Al. Nuestros resultados muestran un dispositivo emisor de azul brillante (493 nm) con una

luminancia alta de 8260 cd m^{-2} con una polarización aplicada de 6.5 V (20.6 mA cm^{-2}). También se evaluaron las características colorimétricas, que muestran una alta pureza de color del 88% para nuestro dispositivo campeón. Además, se alcanzó una asombrosa eficiencia cuántica externa de hasta el 6%. Se lograron PLQY de 64%, en promedio, cuando la capa activa con la adición de iPAm se depositó en sustratos PEDOT:PSS (como en la estructura PeLED), una mejora de 3 veces en comparación con el sistema puro $\text{PEA}_2(\text{Cs}_{0.75}\text{MA}_{0.25})\text{Pb}_2\text{Br}_7$. Se realizaron investigaciones ópticas y estructurales para develar tal comportamiento, indicando que RP de dominios predominantemente $n=3$ están rodeados por fases de dimensionalidad más alta, localizando la recombinación radiativa en dominios cristalinos muy pequeños con orientación aleatoria; beneficiando así el funcionamiento de los PeLEDs.

Samenvatting

De noodzakelijke zoektocht naar efficiënte zelfemitterende schermen en verlichtingstechnologieën voor grote oppervlakten heeft de wetenschappelijke gemeenschap ertoe gebracht nieuwe en veelbelovende halfgeleiders te onderzoeken voor de zogenaamde volgende generatie van halfgeleiderlichtbronnen. De gestandaardiseerde eisen waaraan moet worden voldaan voor de volgende generatie licht-emitterende technologie hangen sterk af van de toepassing. Zo zijn bijvoorbeeld een beter kleurengamma en betere kijkhoeken noodzakelijk voor de schermtechnologie, terwijl bij verlichting met grote uitzendoppervlakten die natuurlijk daglicht nabootsen het essentieel is dat dit niet ten koste gaat van de helderheid. De algemene prestaties van lichtgevende apparaten zijn afhankelijk van vele variabelen, waaronder materialen, fabricageprocessen en apparaatarchitectuur. Vandaar dat de synthese en karakterisering van het halfgeleidermateriaal samen met een studie van de toepassing ervan in elektroluminescerende apparaten slechts een eerste, maar nog steeds een fundamentele stap is naar de mogelijke toekomstige commercialisering van nieuwe licht-emitterende technologie.

Ondanks de grote vooruitgang die reeds geboekt is bij de komende generatie beeldschermen en verlichtingsapparaten, zijn er nog steeds uitdagingen die moeten worden aangepakt. De fabricagekosten voor zelfemitterende beeldschermen en verlichtingstechnologieën zijn hoog en nemen snel toe naarmate het actieve oppervlakte groter wordt, aangezien dure fabricagetechnieken momenteel vereist zijn. Goedkope fabricageprocessen, d.w.z. processen die gebaseerd zijn op oplossingsmethoden, zijn een veelbelovend alternatief voor de huidige technologie. Terwijl efficiënte groene en rode lichtemitters zijn verkregen met in oplossing verwerkbaar methoden, zelfs op grote oppervlakten, blijven de prestaties van blauwe lichtemitters nog achter wegens de moeilijkheid om defectvrije halfgeleiders met zo'n brede bandkloof te verkrijgen. Het gebrek aan efficiënte blauwe lichtemitters heeft de vooruitgang belemmerd op het gebied van volledig gekleurde displays (of heeft creatieve oplossingen vereist zoals bij OLED-schermen) en wit-emitterende verlichtingsbronnen. Om bovenstaande redenen

wordt intensief onderzoek verricht om efficiënte blauw-emitterende anorganische en hybride halfgeleidende materialen te vervaardigen met behulp van in oplossing verwerkbare methoden.

Dit proefschrift richt zich op de fabricage van twee aanstaande blauw-luminescerende halfgeleiders bereid met goedkope technieken en hun toepassing in meerlagige elektroluminescerende apparaten, namelijk elektroluminescerende dunnelaagsapparaten en licht-emitterende diodes.

Elektroluminescerende dunnelaagsapparaten (EDLA) bestaan uit een fosfor tussen twee isolatielagen en worden gecontacteerd door elektroden aan de voor- en achterzijde, waarvan er één transparant moet zijn om het licht door te laten schijnen. Zij zijn dus aangebracht in een metaal-isolator-halfgeleider-isolator-metaal structuur. De fosfor is een halfgeleider met een brede bandkloof die dient als gastmateriaal voor onzuiverheden, namelijk kleurcentra. Deze worden geactiveerd bij de toepassing van een wisselspanning met als resultaat een constante lichtemissie bij hoge elektrische velden. In **hoofdstuk 2** presenteren we de synthese van een fosfor op basis van een bekende metaal-chalcogenide halfgeleider gedoteerd met europiumchloride (III). Hierbij werd zinksulfide (ZnS), in zijn wurtziet kristalstructuur, ultrasoon gepyrolyseerd (pyrosol) bovenop glazen substraten, waardoor een dichte dunne laag werd gevormd. Door de synthese van de met europium gedoteerde ZnS lagen zorgvuldig te controleren, konden we onze europiumbron reduceren tot zijn tweewaardige toestand en zo europiumsulfide (EuS) bindingen vormen. De aanwezigheid van tweewaardig europium (Eu^{2+}) werd bevestigd door EPR-spectroscopie. Eu^{2+} is verantwoordelijk voor de brede blauwe bandfotoluminescentie wanneer het geëxciteerd wordt met een energie van 3.75 eV, d.w.z. de bandkloof van ZnS:Eu^{2+} . Het emissiemechanisme wordt bepaald door $5d \rightarrow 4f$ overgangen van de eerste aangeslagen toestand van Eu^{2+} .

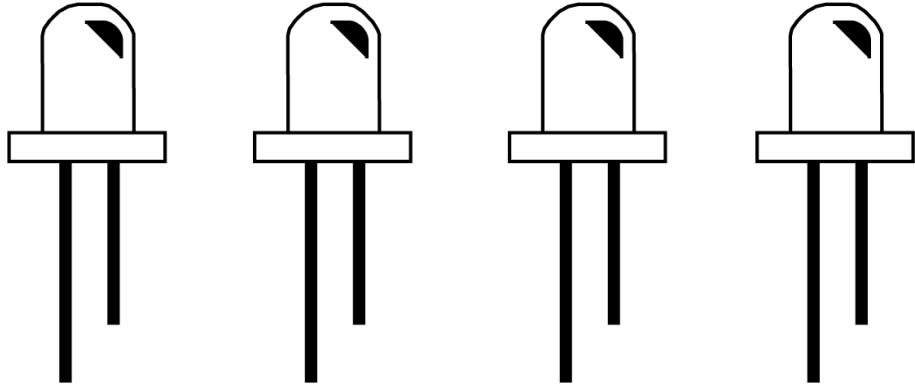
In **hoofdstuk 3** presenteren we de resultaten na de integratie van ons fosfor materiaal in EDLA-apparaten. Wij gebruikten zirkoniumoxide (ZrO_2) als isolerende lagen wegens zijn relatief hoge κ -diëlektrische constante, en gebruikten antimoon-gedoteerde tin oxide (ATO) en aluminium respectievelijk als transparante en metaalelektroden. Het apparaat werd vervaardigd met behulp van een goedkope, relatief snelle en eenvoudige spuitpyrolysetechniek. Wit-emitterende

elektroluminescentie is het resultaat van het toepassen van een wisselspanning bij een vaste 10kHz sinusoïdale frequentie. Wij hebben de colorimetrische kenmerken van het witte licht geanalyseerd door het kwadratisch gemiddelde van de wisselspanning te moduleren over een bereik van 56 V tot 77 V. Het resulterende witte licht bij 77 V is vergelijkbaar met de CIE-lichtsoort D65, die overeenkomt met de standaardverlichting van natuurlijk middagdaglicht in veel landen in Noordwest-Europa. Er werd gespeculeerd dat de oorsprong van de witte emissie voortkwam uit een bijdrage van het bulkfosformateriaal, onzuiverheden van Eu^{3+} in de ingebouwde ZnO-onderlagen inherent aan het pyrosolproces, en intrinsieke defecten bij de vorming van deze onderlagen.

Licht-emitterende dioden (leds) zijn bij uitstek de meest bestudeerde apparaten voor verlichtingstoepassingen. In tegenstelling tot EDLA werken leds met gelijkspanning en relatief lage elektrische velden. De emissiekleur wordt rechtstreeks bepaald door de energie van de bandkloof van de halfgeleider. In een p-i-n overgang worden gaten en elektronen geïnjecteerd in de intrinsieke laag, namelijk de emitterende halfgeleider, om een radiatieve recombinatie van ladingen te veroorzaken. In **hoofdstuk 4** hebben we leds gemaakt met hybride metaalhalogenide perovskieten, die veelbelovende hybride halfgeleiders zijn voor opto-elektronische toepassingen. We gebruikten een ingesloten kwantumsysteem dat wordt geleverd door 2D-3D Ruddlesden-Popper perovskieten fasen (RP), die ons in staat stellen om de bandkloof af te stemmen op het blauw, waardoor de foto-luminescerende kwantumopbrengsten (PLQYs) verder worden verbeterd in vergelijking met de zuivere 3D tegenhanger. Niettemin heeft deze benadering inherente ongemakken met betrekking tot de fasedistributie en hun oriëntatie om het ladingstransport in een led te bevorderen. In een ideale situatie moeten beide parameters dus goed op elkaar zijn afgestemd om een blauwe emissie te garanderen zonder het transport van gaten en elektronen naar het recombinatiegebied op te offeren. We hebben op perovskieten gebaseerde leds (Pe-leds) gefabriceerd met een actieve laag met de nominale samenstelling $\text{PEA}_2(\text{Cs}_{0.75}\text{MA}_{0.25})\text{Pb}_2\text{Br}_7$ die we vergelijken met actieve lagen die isopropylammonium (iPAm) als additief bevatten. Een apparaat architectuur bestaande uit ITO/PEDOT:PSS/perovskiet/TPBi/LiF/Al werd gebruikt. Onze resultaten tonen een helder blauw-emitterend (493 nm) apparaat met een luminantie tot 8260 cd m^{-2} bij een toegepaste spanning van 6,5 V ($20,6 \text{ mA cm}^{-2}$). De colorimetrische kenmerken werden ook beoordeeld,

waaruit een hoge kleur zuiverheid van 88% blijkt voor ons best presterende apparaat. Bovendien werd een intrigerende externe kwantumefficiëntie van maximaal 6% bereikt. PLQYs van gemiddeld 64% werden bereikt wanneer de actieve laag met de toevoeging van iPAm werd afgezet op PEDOT:PSS substraten (zoals in de Pe-leds), een drievoudige verbetering ten opzichte van het zuivere $\text{PEA}_2(\text{Cs}_{0.75}\text{MA}_{0.25})\text{Pb}_2\text{Br}_7$ systeem. Optische en structurele onderzoeken werden uitgevoerd om dit gedrag te onthullen, die aangeven dat RP van overwegend $n=3$ domeinen zijn omgeven door fasen met een hogere dimensionaliteit, waarbij de radiatieve recombinatie wordt beperkt tot zeer kleine kristallijne domeinen met willekeurige oriëntatie die de Pe-leds prestaties ten goede doen.

Translated by Eelco Tekelenburg



Motivation & Objectives

Displays full of rich and vibrant colors are acquired conveniences in modern times where devices as smartphones, tablets, and TVs have become indispensable for our daily routine. At the same time, efficient artificial lights reshaped the illumination design indoors and outdoors. However, for these technologies to be settled as commercially available products, they had to fulfill standardized requirements. This demanded significant time of research to address the multiple challenges associated with the development of such technologies. For instance, punctual white-emitting sources became accessible thanks to the invention of an efficient blue component, which required more than three decades in development. This invention was so relevant that it was awarded a Nobel prize in Physics in 2014. Nowadays, the scientific community is moving towards the so-called next generation of solid-state light emitters for displays and illumination. The next generation is seeking efficient semiconductors, especially for large-area applications, at lower manufacturing costs. Presently, the technologies comprising organic-based and quantum confined materials are achieving promising results for large-area self-emissive displays and white-light emitters. Nonetheless, one of the major obstacles is to reach an efficient blue-emitting semiconductor feasible for the aforementioned applications. Therefore, extensive investigations are being carried out to find potential semiconductors able to meet the standardized requirements. Additionally, the manufacturing processes are highly oriented toward cheaper fabrication techniques, such as solution-processed methods as spin coating, blade coating, and spray pyrolysis. These techniques have the potential to lead to large-area, cost-effective, ultrathin, and lightweight emitting devices. In particular, devices comprising either organic materials, halide perovskites, and inorganic electroluminescent thin film are of importance for the development of large-area self-emissive displays and white emitters.

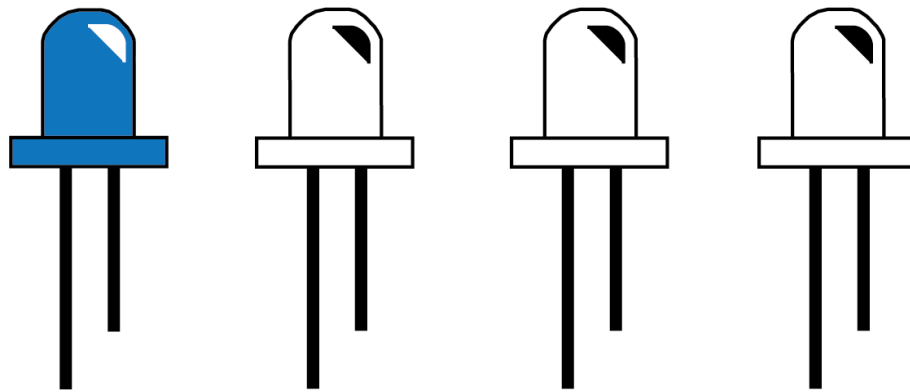
Objectives of the thesis

The general objective of this thesis was to synthesize blue-emitting semiconductors, namely metal chalcogenide and hybrid halide perovskites, deposited by low-cost techniques using solution-processable methods, to subsequently incorporate them in electroluminescent devices.

The specific objectives were:

- Reproducible synthesis of ZnS:Eu thin film phosphor with strong blue emission by spray pyrolysis technique and incorporation in thin film electroluminescent (TFEL) devices.
- Reproducible fabrication and characterization of perovskite light-emitting diodes (PeLEDs) with strong blue emission using 2D-3D Ruddlesden-Popper perovskite phases, with nominal composition $\text{PEA}_2(\text{Cs}_{0.75}\text{MA}_{0.25})\text{Pb}_2\text{Br}_7$ and iPAm as additive.

Chapter 1



Introduction

This chapter provides the background about electroluminescent devices useful to understand the experimental work performed in this thesis. First, it introduces a short review of the physical process named electroluminescence and explains how the first findings unveil the mechanisms, which are nowadays used in large part of the lighting and display technologies. Then, it digs into the working principles of light emitting devices of different structures, starting from the prototypical p-n junctions, till p-i-n and metal-insulator-metal structures. A brief discussion on different driving schemes for these devices is also provided, where the most common direct current (DC) is compared to the uncommon, but potentially very useful alternating current driving (AC). Furthermore, a brief description of the emissive materials incorporated in the investigated light-emitting devices is provided, especially focusing on metal chalcogenides phosphors and metal halide perovskites. At the end, a discussion on the main characterization methods utilized to benchmark the electroluminescent devices fabricated for this thesis is reported. The chapter concludes with an outline of the thesis.

1.1 Electroluminescence

-Electroluminescence-, or “Losev - Light,” the latter term proposed by George Destriau, names the observed phenomenon of light emission from crystals of zinc sulfide (ZnS) under an applied electrical potential. Contrary to the incandescent emission of light bulbs, this new type of light is not accompanied by heat. The phenomenon was initially described in 1907 by H. J. Round, announcing it as a collateral result of his research on cat’s whisker detectors of carborundum (silicon carbide).^[1] But it was not until 1927 when Oleg Losev first published the principle of electroluminescence in a comprehensive collection of his observations while working carborundum crystal detectors followed by multiple publications and patents to describe what we know as the basis of the light-emitting diode (LED)^[2]. Initially, the phenomenon was associated with contact rectification and a great deal of uncertainty as to whether the emission of light raised from some “new process in the crystal itself” or it was arguably a form of “resultant photoluminescence of localized production of high energy radiation.” The latter seemed to clarify the concern as many publications on crystals mainly composed of III-V^[3-5] and II-VI^[6,7] semiconductors were reporting the same – *non-thermal* – light-emission phenomena when an electrical potential was applied. Intriguingly, theories on the working principle of electroluminescence were extensively disputed for ZnS crystals, whether the emission arose intrinsically within the semiconductor or by the charge injection.^[8]

Modernly, electroluminescence is defined as an optoelectronic process in which a semiconductor emits light in response to the application of an electric field. The produced light is the result of the radiative recombination of charge carriers, i.e., electrons and holes, within the semiconductor. Prior to the recombination, and depending on the composition and device structure, the charges are either i) injected in the conduction and valence band (for example, in the p-n junction) or ii) are generated by impact-excitation of a high-energy electron accelerated by a strong electric field as in metal-insulator-semiconductor-insulator-metal (MISIM) type devices. The process of electroluminescence for i) occurs when a forward bias is applied to a p-n junction generating a diffusion current flow; photons will be emitted (with an energy equal to the semiconductor band gap) when the minority carriers (electrons and holes) will recombine in the proximity of the depletion region. Whereas for ii), electrons with high energy are accelerated

by the presence of a strong electric field, colliding with luminescent centers in the active medium and consequently exciting them. The energy gained by the electrons is then released in the form of light.

Direct Current (DC) vs Alternating Current (AC)

Both driving mechanisms for electroluminescence, namely DC and AC, are in principle acceptable. However, depending on the device type, this two-driving mechanism will provide some advantages or some challenges. For example, in p-n junction, the electric field is localized in the recombination zone, and its magnitude is in the order of a few volts/cm (section 1.2.1). The p-n junction diode geometry allows electric current only in one direction (forward - bias) and strongly limits the current in reverse direction (reverse - bias) till breakdown; therefore, a direct voltage source is the most natural solution for these devices. However, this requires a separate circuit to convert the network alternating current in a DC one. For the MISIM type of devices, the electric field can be as high as into 10^6 V/cm,^[9] and they are preferred to be operated by alternating current (AC) to sustain the light emission (section 1.2.3) and limit heating. The following sections will delve into the different types and working principles of the electroluminescent devices fabricated in this thesis.

1.2 Light - emitting devices

1.2.1 p-n junction

A p-n junction is formed through doping of a semiconductor crystal defining a p-type doped region next to an n-type doped one. The p-n junction is at the basis of several semiconductor electronic devices, such as rectifiers, transistors, solar cells, LEDs, and the diode laser. In the following, we will focus on how to use the p-n junction for LEDs describing its working principle.

Working principle

A p-n junction diode is fabricated as schematically shown in figure 1.1 (a); namely, the p-type and the n-type semiconductors encounter in a sharp junction, and each one is also connected to the corresponding metal contact. The symbol representing the diode is reported in figure 1.1 (b).

In equilibrium conditions, the Fermi level is constant, and the bands are tilted in the transition zone due to the built-in electric field [figure 1.2 (a)]. At the junction, free carriers diffuse to their opposite charge region because of the concentration gradient of electrons and holes, leaving behind immobile space charges. This emerges in a localized barrier potential V_0 , also known as the depletion region, acting as a zone that repels the mobile charges away from the junction through the built-in electric field. Simultaneously, the built-in electric field is felt by the holes and the electrons provoking charge drifts across the junction. In equilibrium, the resultant current drifts and diffusion are balanced.

If we connect the diode to an external source supplying a potential difference (bias voltage), then the drifts and diffusion currents are no longer balanced, inducing a net current flow. The bias voltage can be supplied in forward or reverse mode.

Forward bias ($V > 0$)

In forward bias mode, the p-side is connected with the positive terminal, and the n-side is connected with the negative terminal. Consequently, there is a reduction of the barrier potential ($V_0 - V_{rwd}$) and strength of the electric field (ϵ). The reduction of the potential results on the majority charges to move towards the opposite doping side, leading to a current to begin to flow. Herein the diffusion currents ($I_{\text{diffusion}}$) overcome the opposing drift currents (I_{drift}) as shown in figure 1.2 (b).

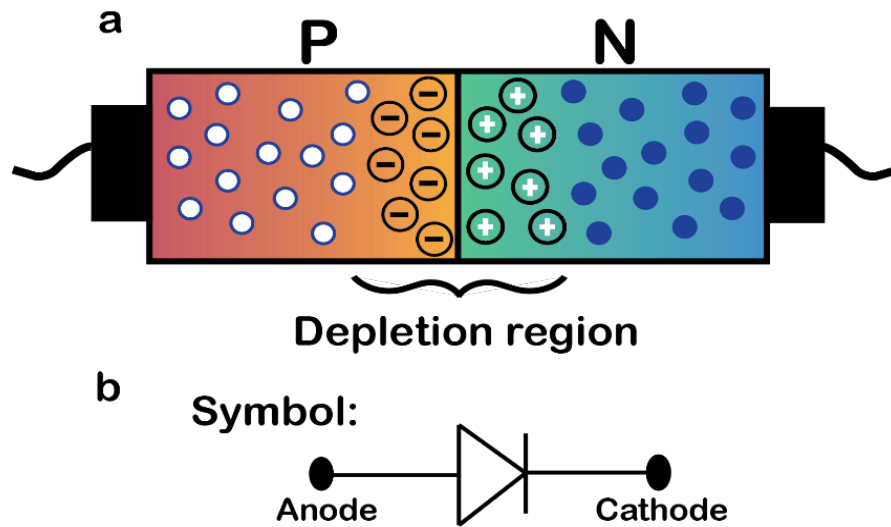


Figure 1.1 (a) Schematic illustration of a p-n junction diode at equilibrium conditions and (b) the diode symbol as represented in electronics.

In this condition, the recombination of charge carriers across the band-gap may happen, hence giving rise to light emission. The average travel distance, particularly of electrons towards the P-type semiconductor before recombination, is called diffusion length. Obviously, a smaller diffusion length is desirable for light emission applications, often to block charge carriers and increase the probability of recombination the so-called double heterojunction is fabricated.^[10]

Reverse bias ($V < 0$)

In reverse bias, the p-side is connected to the negative terminal and the n-side to the positive terminal. By doing so, the magnitude of the potential barrier increases, as well as the electric field, leading to a widening of the depletion region. The drift currents (I_{drift}) dominate against the diffusion currents ($I_{\text{diffusion}}$); hence, there is a high resistance for flow of charges, allowing minimal current to cross the p-n junction. The depletion region behaves as an insulating zone forbidding electrons and holes to recombine. Thus, a LED cannot be operational when a reverse bias is applied. Conversely, if in this condition the junction is illuminated by light of energy larger than the band gap, a substantial photocurrent will be obtained.^[11]

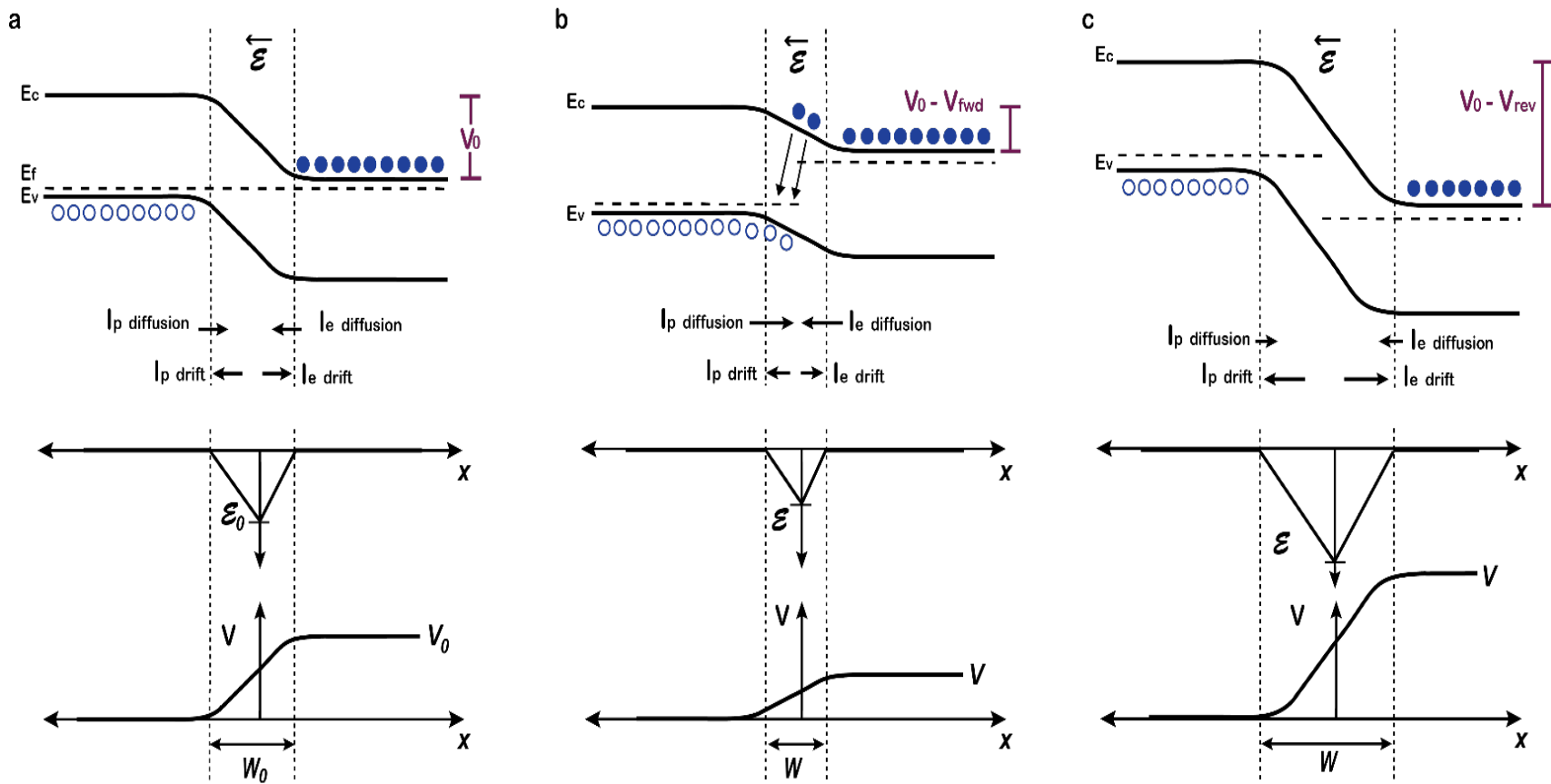


Figure 1.2 Band model of a p-n junction (top) and representation of its electric field and net potential (bottom) at (a) equilibrium conditions (b) forward bias, and (c) reverse bias. At equilibrium conditions, the net charge flow is balanced at the depletion region, when a forward bias is applied the energy barrier decrease prompting a current to flow. The opposite behavior occurs when a reverse bias is applied.

1.2.2 p-i-n junction

A p-i-n diode is a device structure comprising of three units; a heavily doped p-type and a n-type semiconductors, which serve as ohmic contacts, and an intrinsic semiconductor between them. A schematic illustration of the device structure is shown in figure 1.3 (a), including the corresponding symbol used in electronics (b). Contrary to the p-n junction diode, the addition of such intrinsic layer makes the device a poor rectifier but increases the suitability for other applications as photodetectors and for high-power electronics applications. The p-i-n structure is also more flexible and is often used in emerging semiconductor devices, where traditional doping is not achievable. It is the main device structure used nowadays in metal halide perovskite optoelectronics.

Working principle

The working principle of a p-i-n diode is very similar to that of the p-n junction diode, with the exception of a modified depletion region, due to the inclusion of an intrinsic layer, where no charge carriers are to be found. This intrinsic layer creates a certain degree of separation between both heavily doped semiconductor, but still allowing the formation of a junction. At equilibrium conditions (unbiased) charge carriers will diffuse towards the i-layer until both holes and electrons are in equilibrium. In forward bias, the heavily doped semiconductors will begin to inject free charges into the intrinsic layer hence a current flow will begin. Here the concentration of the injected charges is greater than the one that could possibly hold the intrinsic layer; consequently, the electric field extends further into the region.

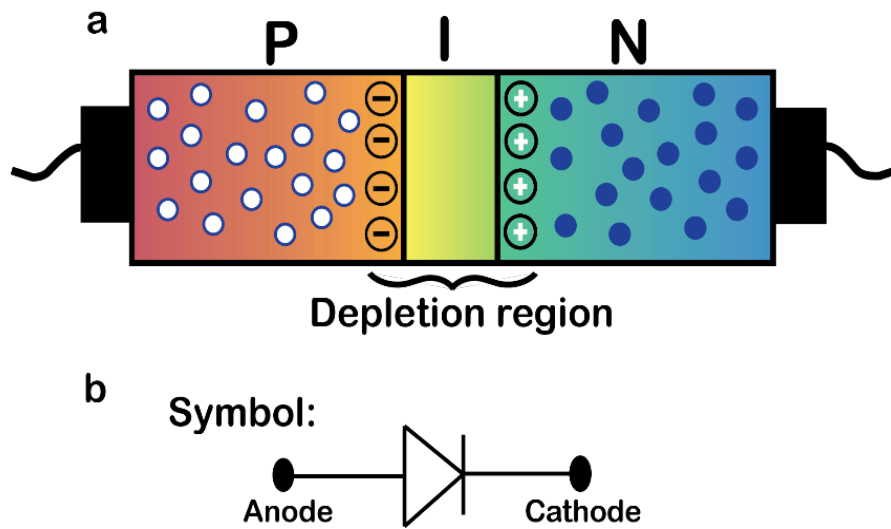


Figure 1.3 (a) Schematic illustration of a p-i-n junction diode and (b) the diode symbol as depicted in electronics.

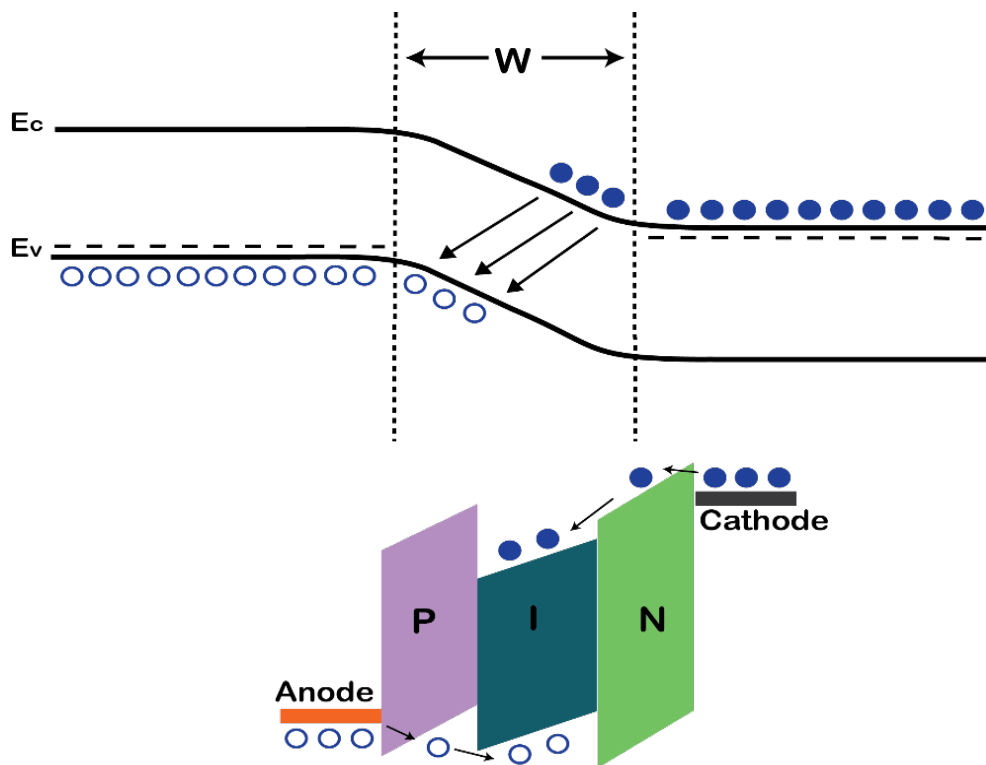


Figure 1.4 Band gap model for p-i-n junction diode. At forward bias, heavily doped semiconductors begin to inject charge carriers towards the intrinsic region, allowing charges to recombine.

For p-i-n junction LED, the intrinsic layer is mainly defined as the emissive layer, which is responsible for the light emission. The energy of the photons is strictly given by the energy band gap of the intrinsic semiconductor. In LEDs, the p-i-n structure has the advantage to separate the transport and recombination region reducing the probability of non-radiative recombination and favoring charge carriers confinement in the material with the highest quantum yield. Figure 1.4 shows the band gap model for p-i-n junction LEDs, where the p-type and n-type semiconductors are selected to allow charge transport but simultaneously block the crossing of the opposite charge carriers.

1.2.3 Thin-film electroluminescent devices (TFEL devices)

In thin-film electroluminescent devices (TFEL), a host band gap polycrystalline semiconductor with luminescent impurities is typically used as a phosphor material, which is enclosed between two insulating layers of high dielectric constant (κ). Historically, two dielectric layers enveloping the phosphor layer, have been widely used for TFEL devices forming a metal–insulator–semiconductor–insulator–metal (MISIM) structure, albeit multiple dielectric layers have been also reported.^[12] Here, the phosphor corresponds to the semiconductor and the insulator layers are the high dielectric thin layer. One of the metal contacts has to be transparent to allow the EL - light to scape whilst the other is commonly a reflecting metal. As introduced in section 1.1, this type of device usually requires a strong electric field to accelerate electrons to excite the luminescent centers, followed by photon emission. The energy of the photons emitted is associated with the nature of the luminescent centers.

Working principle

A TFEL device begins to operate when a bias is being applied through the electrodes, generating a high electric field in the phosphor layer. This allows the trapped electrons at the insulating and the phosphor layer interfaces to tunnel to the conduction band of the latter. Due to the presence of the electric field, they are accelerated and prompt to impact several of the luminescent centers. The impurity's outer valence band electrons get excited; thereupon, they return to their ground state by emitting light. Yet some accelerated electrons continue their path

in the conduction band, reaching the opposite insulator layer; getting trapped there. The process is reversed when the polarity of the bias is changed. It is important to emphasize that the accelerated electrons in the conduction band may also excite some valence band electrons into the conduction band of the phosphor semiconductor in a process known as an avalanche. These additional electrons may also interact with the luminescent impurities further sustaining the emission of light. This process is also occurring when the polarity is changed.

To sustain the operation of the TFEL is required an AC voltage; therefore, the light emission is also modulated with the same frequency of the voltage.^[13] In figure 1.5 is depicted a schematic representation of TFEL device and its working principle.

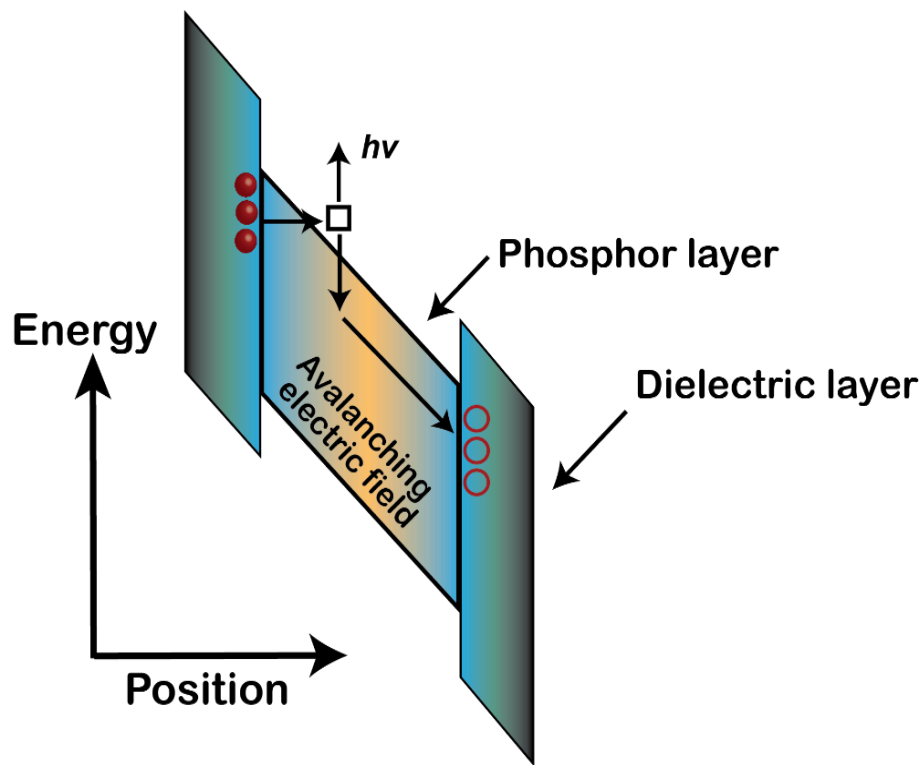


Figure 1.5 TFEL devices band diagram and working principle. Interface full circles are occupied traps, whereas hollow circles are empty traps. Tunneling is followed by an acceleration of the trapped electrons promoting impact-excitation in the luminescent centers (empty squares) and an avalanche process in the phosphor layer. Re-trapping will occur at the opposite dielectric interface.

1.3 Materials for light emission

1.3.1 Metal chalcogenides matrices

The term phosphor covers a wide range of solids that emit visible light when excited either by a beam of electrons or by short-wavelength photons.^[14] Metal chalcogenides are compounds consisting of two monovalent metals or one divalent and one chalcogenide anion (mainly; S, Se, Te, rather than O), which have been widely used as phosphor materials in photo-, cathode-, and electro-luminescent applications.^[15] The photoluminescence and electroluminescence performance of a phosphor depends on the phosphor matrix's electronic and optical properties and the properties of the optically active impurities that act as luminescent centers. Upon doping with transition metals or rare earth elements, the luminescence of the metal chalcogenides can be varied over the entire visible region by appropriately selecting the chalcogenide composition host and the type of dopant. Since the middle of the 1980s, several metal sulfides phosphors with different color emissions, such as ZnS:Mn (orange), ZnS:Cu (green), CaS:Ce (green), SrS:Ce (blue-green), CaS:Eu (red), and SrS:Eu (orange), have been intensively investigated.^[9,16,17] Among these combinations of metal sulfides and dopants, ZnS:Mn and ZnS:Cu resulted in some phosphors with efficient photoluminescence and electroluminescence (EL). The main successful application of these phosphors has been in flat-panel monochromatic displays based on thin-film electroluminescence, field emission displays, and ZnS-based powder electroluminescence for backlights. In more recent years, ZnS:Eu has also gained increasing interest due to its intense blue photoluminescence.^[18,19]

Host chalcogenide: ZnS

ZnS belongs to an important class of the first phosphors used in cathode ray television tubes and is surely one of the most investigated metal chalcogenides. It is demonstrated to show one of the highest performances as a host phosphor as it can house a number of different luminescent centers. This is largely because ZnS meets most criteria that must satisfy a phosphor to enable efficient light emission.^[20] These are: i) It must be transparent to the wavelength of light being

emitted. ii) It has to contain impurities having localized quantum states, act as an electrical insulator, and iii) exhibit an avalanching-type breakdown process once a critical electric field is reached. iv) The critical field must be of the order of 10^8 V/m. Namely, for a typical thickness of 1 micrometer, it means that this critical field is reached when about 100 V falls across it. v) Finally, the electrons responsible for light emission must be able to fall into a localized ground state even in the presence of a high electric field.

ZnS belong to the II-VI semiconductor family and has an energy gap of 3.6 eV and it is therefore transparent to photons with energies in the visible range (1.7 - 3.1 eV). The ZnS lattice is formed from sp^3 hybrid orbitals, and it gives rise to ZnS bonds with a covalency of 0.377 and a fractional ionic character of 0.623. Two structural variants exist, i.e., the cubic (zinc blende) and the hexagonal (wurtzite), each Zn^{2+} ion is coordinated by four S^{2-} ions in a tetrahedral configuration, as shown in figure 1.6. ZnS is a relatively stable sulfide in that it may be stored in ambient atmospheric conditions without degradation. Moreover, it does not require moisture protection when subjected to high electric fields in an EL device.

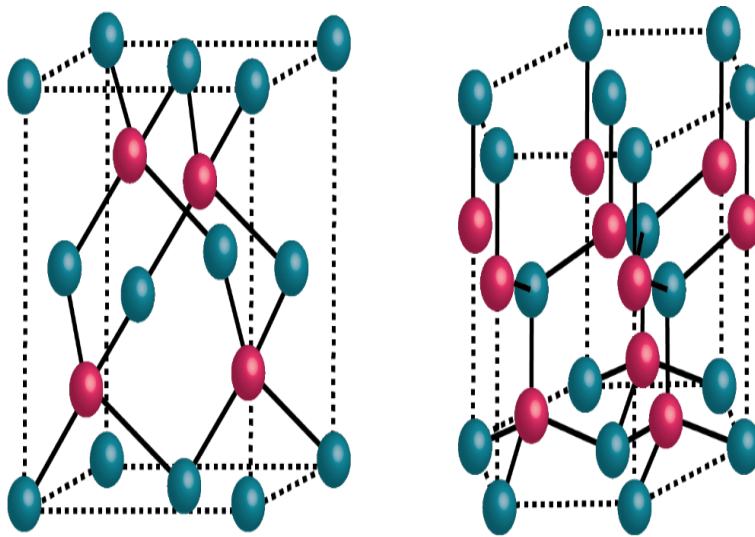


Figure 1.6 Zinc blende (left) and wurtzite (right) structures of ZnS.

Luminescent centers

As mentioned in the previous section, the photoluminescent and electroluminescent performance of a phosphor depends strongly on the optical activity of the impurities lodged in the phosphor matrix, serving as luminescent centers. The main dopants that act as efficient luminescent centers in metal chalcogenide and metal oxide phosphors are transition metal ions and rare-earth ions, commonly occurring in divalent or trivalent forms. Generally, the positively dopant ions are positioned on a lattice site, substituting a divalent or trivalent cation of the phosphor host matrix. In transition metal luminescent centers with electronic configurations of $[\text{Ar}] 3d^n 4s^2$ ($n = 1-9$), the divalent dopant ions are formed by losing the outermost 4s electrons, and the trivalent valency is possible if one of the electrons of the external 3d levels is also lost. In the rare-earth with electronic configuration $[\text{Xe}] 4f^n 6s^2$ ($n = 1-13$), divalent or trivalent ions are formed by losing the 6s electrons first and then one of the $4f^n$ electrons.^[14]

The optical properties of free ions in the gas phase are characterized by sharp emission and absorption lines, with wavelengths determined by their energy levels. However, when the same ions are doped into a crystalline host, the optical properties are modified because their external energy levels can be shifted by the interaction of the electric field produced by the surrounding negative ions. This interaction is known as the crystal field effect. If the crystal field effect is weak, the emission and absorption spectra will remain discrete lines, but perhaps with their frequencies slightly shifted and certain degeneracies lifted. On the other hand, if the interaction is strong, the frequencies of the transitions will be quite different from those of the isolated atoms, and the spectra may be broadened into a continuum.

For example, for transition luminescent center such as Mn with an electronic configuration: Mn ($Z=25$): $[\text{Ar}]3d^5 4s^2$, the $\text{Mn}^{2+}:[\text{Ar}]3d^5$ ion is substitutional positioned on a divalent lattice site of $\text{Zn}^{2+}:[\text{Ar}]3d^{10}$. This is because the chemical nature of Mn^{2+} and Zn^{2+} are similar. The only difference in the electronic configuration between the Zn and Mn atoms is that Zn has a fully occupied $3d^{10}$ shell, and Mn has a half occupied $3d^5$ shell. The Mn $3d^5$ energy level lies about 3 eV below the valence band maximum. Therefore, the ground state for $3d^5$ intra-shell transitions of the Mn luminescent centers is well isolated from those corresponding to the matrix. This may

be one reason why the Mn^{2+} centers in ZnS are mainly excited by direct electron impact excitation when incorporated in electroluminescent devices.^[21,22] Since the energy levels of the $3d^5$ excited state of Mn^{2+} are affected by the crystal field, the emission color will depend on the host lattice. In ZnS, the Mn^{2+} center is surrounded by four S^{2-} anions in a tetrahedral configuration (see figure 1.7) and will show yellowish-orange luminescence peaking at 585-590 nm.^[23,24]

As will be addressed in more detail in chapter 2, when the luminescent centers incorporated in ZnS are divalent rare-earth ions such as Eu^{2+} substituting the Zn^{2+} , the large energy difference (energy gap) between the 5d and 4f energy levels for the free Eu^{2+} (4.2 eV) is decreased. This is because the excited 5d orbitals are strongly affected by surrounding S^{2-} anions; while, the well-shielded 4f levels are less affected. The combination of the crystal field effect with the nephelauxetic¹ and Stokes shift effects give rise to a blue luminescence peaking at 454 nm (2.73 eV).^[25,26]

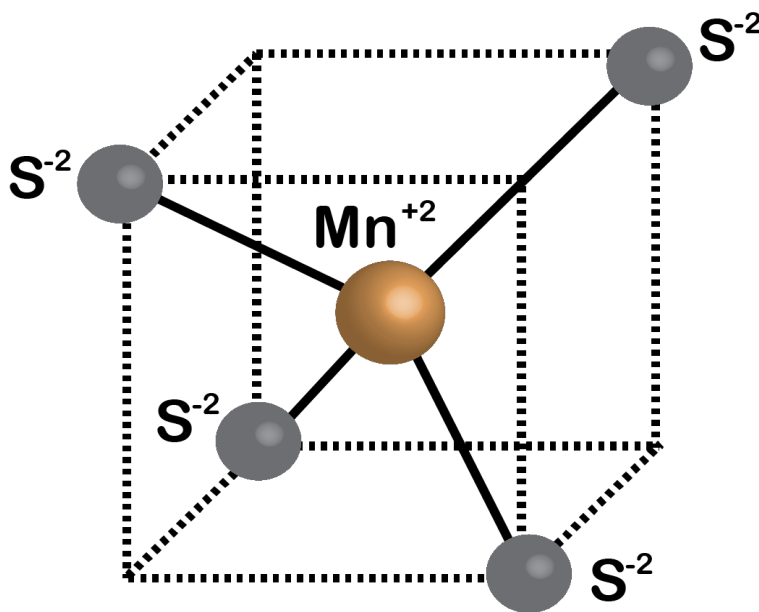


Figure 1.7 The symmetry of the Mn^{2+} ions in ZnS.

¹ Nephelauxetic effect refers to the decrease in interelectronic repulsion caused by the presence of more than one electrons in d-orbital of a free metal-ion and its interaction with its surrounding in a complex-ligand configuration.

1.3.2 Metal halide perovskites

Metal halide perovskites have become one of the most promising semiconductors for light emission due to their excellent optoelectronic properties, possibility of chemical manipulation, and solution processability. Perovskite-based light-emitting diodes (PeLEDs), comprising a multilayer p-i-n junction, have been recently explored as the next generation of light emitters. It has been only eight years since the first PeLED paper was published,^[27] and the race to understand, improve, and fully develop a perovskite-based light-emitting technology is still going on.

Conventional metal halide perovskites exhibit a three-dimensional (3D) structure with a chemical formula of AMX_3 , where A is a monovalent cation (methylammonium MA $CH_3NH_3^+$, formamidinium FA $NH_2CH=NH_2^+$, or cesium Cs^+), M is a bivalent metal cation (lead Pb^{2+} , tin Sn^{2+}) and X is a halide monovalent anion ($X=Cl^-$, Br^- or I^-). As figure 1.8 shows, in a single unit cell of an AMX_3 crystal, the bivalent cation M is enveloped by an octahedron comprising six halide monovalent anions X, and the monovalent cations A reside between these corner shared octahedra. Each monovalent anion X is face-centered of the cube formed by the monovalent cations A.

It has been demonstrated that bandgap tailoring can be achieved with two main strategies, namely, i) using different halides, and ii) the reduction of dimensionality of the electronic delocalization going from 3D to 2D, 1D, and 0D.^[28–30]

In $MAPbX_3$ single crystals it has been shown that by replacing the halide, the bandgap is modified from 1.53, 2.24, 2.97 eV for I, Br, Cl, respectively.^[31] In other words, the interchange of smaller halides widens the energy gap, delivering the possibility to tune the emission towards higher energies. The second possibility is when the size of the crystal is restricted either by impeding the growth of the 3D cluster by imposing capping ligands leading to the formation of nanocrystals^[32] or separating the corner-sharing BX_6 octahedral along different crystallographic planes by the incorporation of larger cations (mostly organic one).^[33] The latter gives rise to the formation of layered perovskites, which are also known as 2D Ruddlesden-Popper phases.

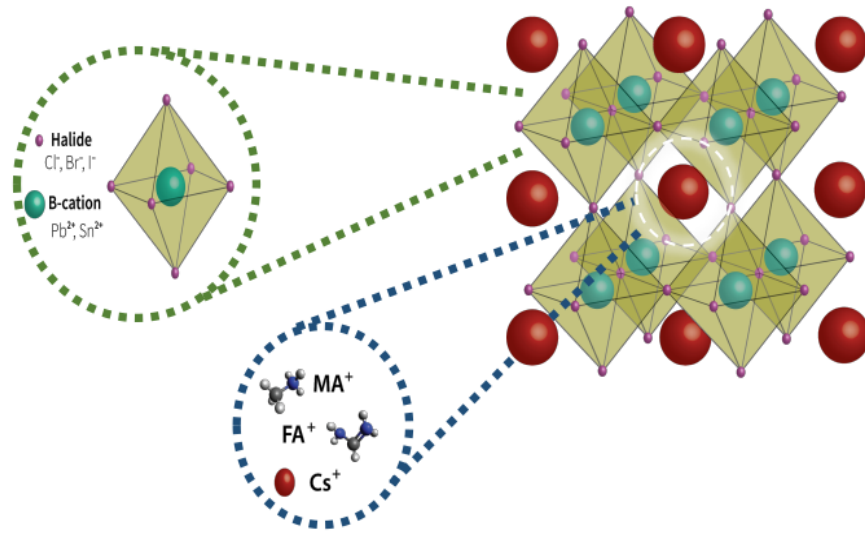


Figure 1.8 Schematic representation of AMX_3 metal halide perovskite crystal.

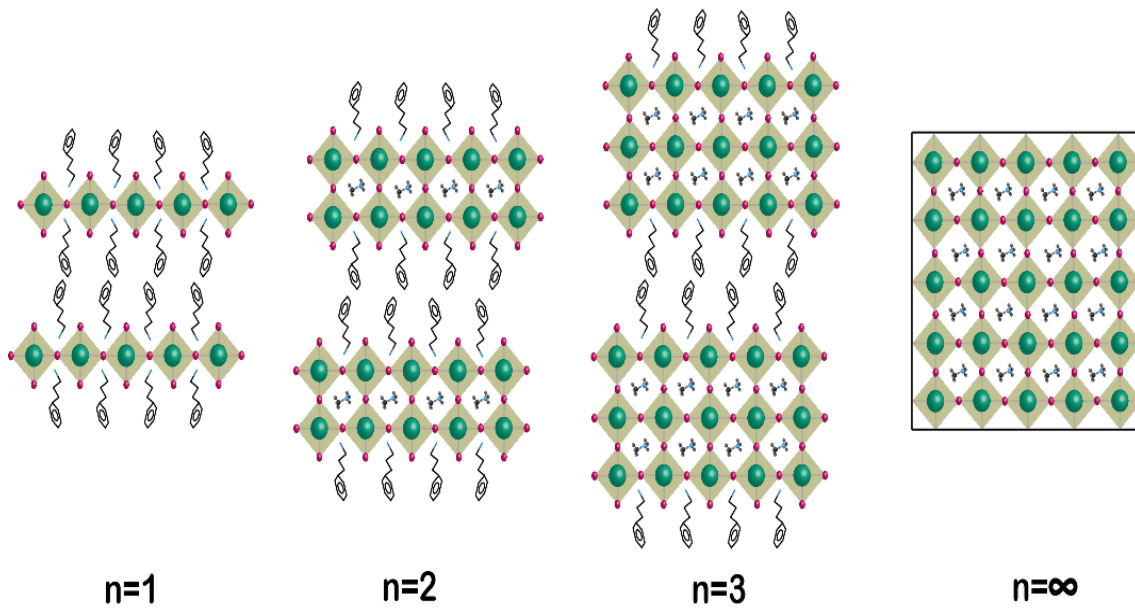


Figure 1.9 From left to right: Ruddlesden Popper (RP) phase $n=1$, Quasi-2D RP phases $\langle n=2 \rangle$, and $n=3 \rangle$, 3D perovskite crystal.

2D and quasi 2D perovskite

2D perovskites are formed when a larger cation breaks the 3D structure of the perovskite crystals, resulting in the formation of layered perovskites. This layered system is defined as from the number of corners shared octahedra layers; for instance, $n=1$ is a Ruddlesden-Popper (RP) phase with structural formula L_2MX_4 ; where L is the large spacer cation and X the halides. When a small cation is introduced into this perfectly 2D system, quasi - 2D phases are formed; for example, $\langle n=2 \rangle$ with structural formula becoming $L_2AM_2X_7$, further continuing increasing the number of RP layers to n , the general structural formula becomes $L_2A_{n-1}M_nX_{3n+1}$ (see figure 1.9).

Quasi 2D perovskites' optical properties are enhanced in terms of light-emitting applications. Their inherent quantum-well structure enlarges the exciton binding energy due to the dielectric and quantum confinement effects. Additionally, the engineering of different phases in the same thin film can favor efficient energy transfer, consequently boosting the quantum yield (QY). Importantly, long organic cations, depending on their chemical properties, can enhance the stability of the perovskite layers, making of quasi 2D perovskites a perfect candidate for the next generation of light emitters.

1.4 Device characterization

1.4.1 Colorimetry

Colorimetry is the science that allows quantifying and describing the human perception of an object's color or of a light source. While spectrometry is caring about absolute units, colorimetry has as a reference detector the human eye.

According to the Colorimetry Committee of the Optical Society of America, "Color is made up of those measurable characteristics of light other than those of space and time; light being that aspect of the radiant energy that man perceives through the visual sensations that are

produced by the stimulation of the retina.” The characteristics of light alluded to in this definition are three: *hue, saturation and brightness*.

Hue refers to that characteristic that allows a color to be classified as red, blue, orange, yellow, etc. For example, gray is an indeterminate hue; thus, it has no hue.

Saturation describes the degree to which a color separates from neutral gray and approaches to a pure color. A neutral gray is completely unsaturated, while a pure spectral color is completely saturated. Taken together, the hue and saturation characteristics constitute the chromatic characteristics of the visual perception. Brightness is the characteristic of any color sensation that allows it to be classified as equivalent to the sensation produced by some element of a neutral gray scale, ranging from white at one end of the scale to black at the other. But how bright is a color? In order to answer this question, it has to be taken into consideration the human eye's perception of radiant light. For instance, a radiant flux being emitted from a sample is invariable. Still, the effectiveness of its brightness depends on how it is distributed in the emitted spectra. Thus, equal amounts of radiant flux do not produce a visual sensation of equal brightness. The relationship between radiant flux and its perception at the human eye is called the luminous efficacy, as shown in figure 1.10.

The science that studies the measurement of light weighted by the human eye is called photometry. It is a field derived from the radiometry discipline, which is responsible for measuring electromagnetic radiation. The eye can detect only visible radiation with a significant susceptibility for the green color at 555 nm with a maximum efficacy of 683 lm/W.

The international lighting commission (CIE from French Commission internationale de l'éclairage) in 1931 agreed to express and quantify the characteristics of light referred to above (brightness, hue, and saturation) in a chromaticity diagram, in terms of the achromatic characteristic of brightness or luminous flux and of two other characteristics that refer to the chromaticity of light, which are: the dominant wavelength and purity.

The dominant wavelength corresponds to the color sensation's characteristic called hue, and the color purity is the saturation.

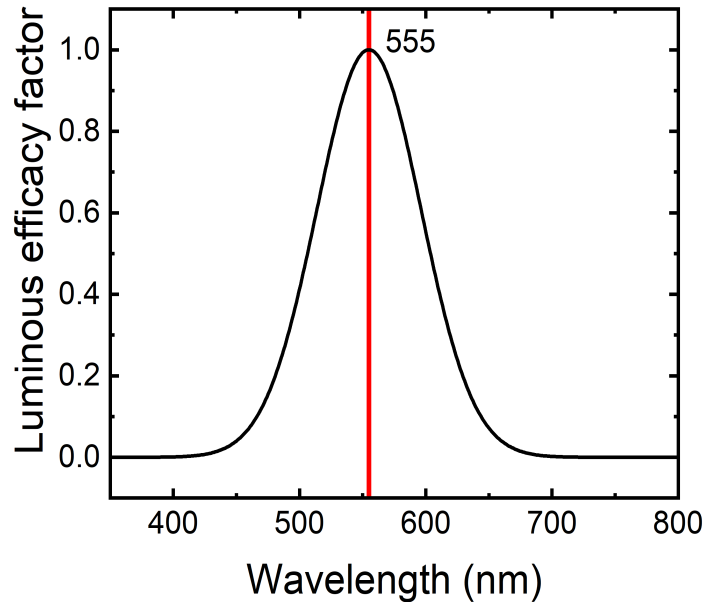


Figure 1.10 Luminous efficacy curve of the human eye with photopic vision.

The spectral responses of the cones of the human eye (mostly active during day vision) are known as l , m , s (long, medium, and short) are linear combinations of the color coupling-functions,^[34] and are represented as the standard functions: \underline{x} , \underline{y} , and \underline{z} as used for a CIE 1931 2nd Standard Observer. The CIE in 1931 agreed to make a description of the chromaticity of light in a 2D color space or CIE coordinate diagram (see figure 1.11) using mixtures of these three coupling functions.^[35] A more detailed explanation of the coupling-functions can be found in chapter 3.

The CIE 1931 diagram shows the locus coordinates with labeled hue wavelengths (saturated colors). Each color perceived by the human eye can be described using this chromaticity diagram and it is represented with the color coordinates (x_s, y_s) . A standard observer with coordinates (x_i, y_i) is used to evaluate the color of a sample qualitatively. For instance, the dominant wavelength (x_d, y_d) is given by the intersection between a straight line from illuminant

to locus curves passing through the sample. The saturation, or color purity, is given by the ratio between the distance from the illuminant to the sample point and the distance from the illuminant to the dominant wavelength.

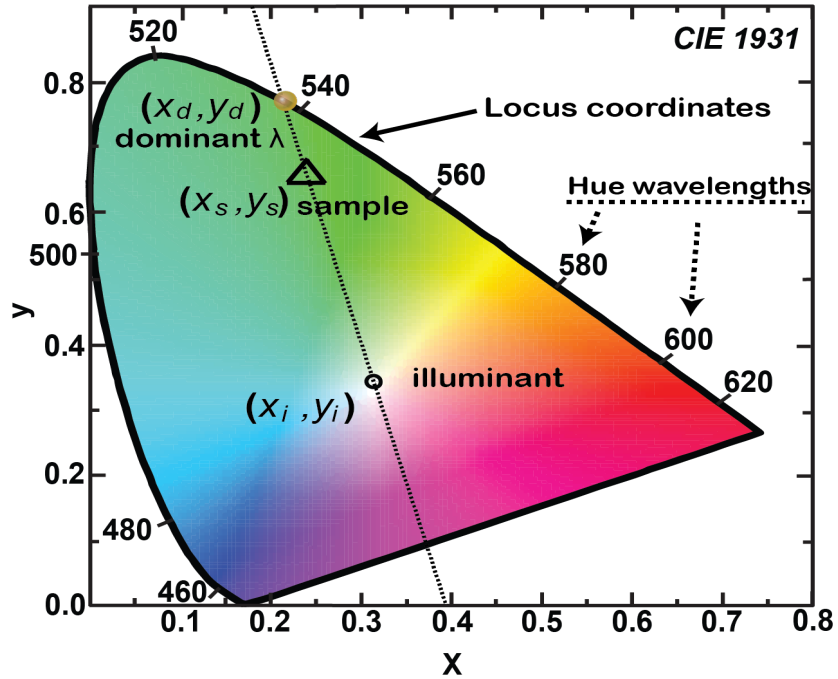


Figure 1.11 The CIE 1931 space chromaticity diagram. The color coordinates of a sample are represented by (x_s, y_s) . The locus curve contains all the possible hue wavelengths, where the dominant wavelength can be extracted (x_d, y_d) . All qualitative color measurements are measured with respect to an illuminant with coordinates (x_i, y_i) .

In chapter 3, we provide a fully practical example of the calculation of the colorimetric properties, including the color purity and the dominant wavelength of a white-emitting device.

1.4.2 External quantum efficiency and Luminous power

The efficiency of a light-emitting device describes how effectively the electrical current is transformed into photons. It has been widely debated which procedures should be followed to accurately determine the efficiency of a device as discrepancies may arise amongst different research groups (especially in the first stage of an emerging technology). The external quantum efficiency (EQE) is one of the most used figures of merits. The most important points to notice

are the need to use calibrated detectors to precisely count the photons emitted and to collect photons emitted at every angle.

The following procedure was used to determine the EQE of our perovskite-based light-emitting diodes (Chapter 4).

We assembled a setup that involved two photodetectors attached to an integrating sphere (IS) wall. Both photodetectors were previously calibrated using a known irradiance spectrum of a commercial light source. The electroluminescent devices to characterize were attached to the walls of the IS in a 90-degree configuration. Additionally, we use a shadow mask to only expose the LED area; hence, no waveguided light by the substrate can participate in the absolute amount of light collected. The samples were adjusted to the IS entrance, assuring the light path (view direction) within the area of the aperture of the IS. For more complete details, please refer to the experimental details of chapter 4.

The EQE can be calculated using the following equation:

$$EQE = \frac{PC_{det}}{I_{LED}} \times \frac{I}{R} \times \frac{e}{hc} \times \frac{\int \lambda EL_{norm}(\lambda) d\lambda}{\int EL_{norm}(\lambda) d\lambda} \quad (1)$$

Where PC_{det} is the photocurrent collected through the calibrated photodiode, I_{LED} is the current passing through the device. R is the photoresponsivity of the diode, e is the elemental charge of an electron, h is the Planck constant, and c is the speed of light. The weight average integral represents the emission spectra of the device, and for these the electroluminescence spectra were collected by coupling an optical fiber to the IS.

The luminous power is the radiant flux being emitting by the diode adjusted to the human eye sensitivity. When the light is emitted from the device, it travels in a given direction (solid angle). The photometry unit, which describes the relationship of the luminous power as a function of the solid angle per square unit, is called luminance (L) per square meter unit. The

correlation between the luminous power of the device with its electrical characteristics is performed through the J-V-L curve, as displayed in Figure 1.12.

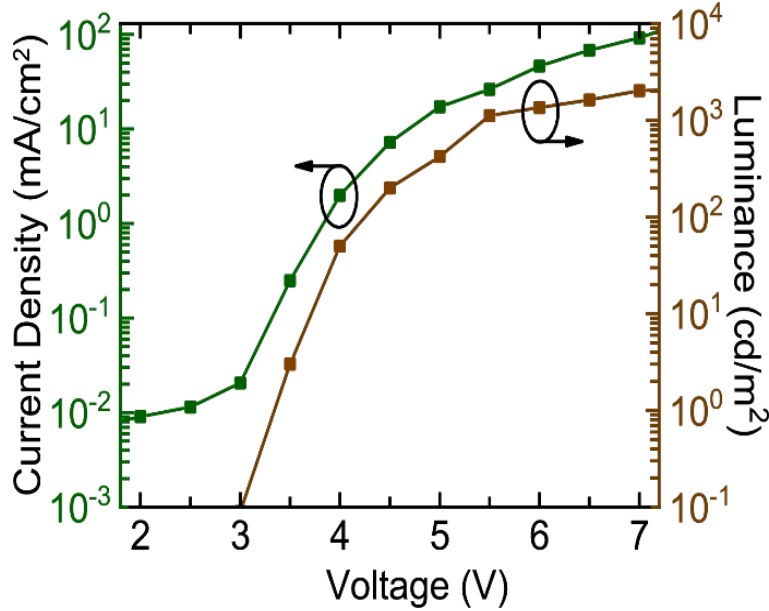


Figure 1.12 Example of typical J-V-L curve in semi-logarithmic scale. It pictures the relationship of the density current flowing through the device and the luminous power as function of the voltage applied across the LED.

The luminance is extracted from the following equation:

$$\phi_v = \frac{1}{f} 683 \frac{\text{lm}}{\text{W}} \int V(\lambda) PC_{det}(\lambda) \frac{1}{R(\lambda)} d\lambda \quad (2)$$

Where the factor 683 lm/W is the peak photonic response of the eye evaluated at 555 nm. $V(\lambda)$ is the luminous efficacy curve as a function of the wavelength, PC_{det} is the photocurrent of the photodetector, $R(\lambda)$ is the responsivity of the photodetector and f coupling factor between the source and the photodetector. The latter mainly depends on the setup configuration.

Finally, we can extract two other efficiencies to evaluate our LED performance, namely the current efficiency n_L and the luminous efficacy n_p . The current efficiency describes the amount

of current passing through the device necessary to produce a certain amount of luminance. The units for current efficiency are cd/A. It can be calculated using equation 3.

$$n_L = \frac{L}{J} = \frac{LS}{I} \quad (3)$$

Where L is the luminance, J is the density current, I is the current and S is the area of the our emitting source.

Through the current efficiency, the luminous efficacy can also be calculated using equation 4. The luminous efficacy determines the light output per unit of electrical power (lm/W).

$$n_p = \frac{n_L D\pi}{V} \quad (4)$$

Where V is the electrical potential difference, D is the angular distribution of the light being emitting by the diode in a given direction with θ and φ angles and the light intensity (I) as follow:

$$D = \frac{1}{\pi I_0} \int_0^{\pi/2} \int_{-\pi}^{+\pi} I(\theta, \varphi) \sin(\theta) d\varphi d\theta \quad (5)$$

1.5 Thesis outline

Display technology and large-area lighting technologies continuously seek efficient and low-cost manufacturing techniques to be implemented in ‘never-old fashion’ next-coming generation of light-emitting devices. This drives the light-emitting community to search for the best semiconductors to fulfill the prerequisite of the NTSC² for self-emissive displays and the committee of white emitters. Great progress has been made to achieve punctual emitters,

² NTSC refers to the National Television System Committee. This association is responsible to set the color standards to meet for display technology.

especially after the development of GaN as blue emitter, which has allowed us to have brighter white emitting lamps. However, for self-emissive large area displays, which are used for different applications from TV screens to cell phone displays, and for more natural white light illumination, there are still some challenges to be addressed. Among these challenges, we can emphasize the need to have better and efficient blue emitters that can be synthesized by low-cost fabrication techniques, such as those based on solution-processable methods. Thus, the work presented in this thesis comprises of this search for brighter and more saturated blue emitters fabricated by relatively low-cost solution-processable techniques and their incorporation in electroluminescent devices. The overview of each chapter is given below:

Chapter 2: A chalcogenide-based phosphor, namely ZnS (in its wurtzite crystal structure) doped with europium, was synthesized by ultrasonic spray pyrolysis technique as thin films. Broad-blue photoluminescence ascribed to the presence of the Eu^{2+} , as luminescent centers in the ZnS host matrix, was confirmed by steady-state photoluminescence spectroscopy when excited with energy equals to the band gap of the system ZnS:Eu²⁺. Careful control of the synthesis allows us to reduce the europium source to its divalent state form even in aerobic conditions, presumably forming EuS bonding. Further, the presence of europium in its divalent state was corroborated by electron paramagnetic resonance. We present an emission mechanism associated with the Eu^{2+} in the ZnS matrix, concluding that the blue emission arises from the $5d \rightarrow 4f$ transition of the first excited state. These finding highlight the feasibility of fabricating large area blue emitters using a relatively simple and cheap solution-based technique, which gives them potential for their application electroluminescent displays.

Chapter 3: The blue emitter ZnS:Eu²⁺ was incorporated in MISIM-type alternating current thin film electroluminescent devices. Comprising zirconium oxide as high dielectric insulator layers and envelop the phosphor and antimony indium oxide and aluminum as front and rear electrodes, respectively. The devices were assessed at three different operational voltages (rms) of 56 V, 70 V and 77 V, at fixed and at 10 kHz sinusoidal frequency to evaluate their electroluminescence and colorimetric characteristics. The devices presented a white electroluminescence, particularly at 77 V, which coordinated of the D65 illuminant, namely analogous to noon daylight. We proposed a possible origin of the white EL, concluding that it

is attributed to electron-impact excitation and subsequent relaxation of Eu^{2+} and Eu^{3+} excited states, and presumably intrinsic point defect residing close the emissive-dielectric layer interfaces. These results demonstrate the possibility of fabricating white emitters, required for the next generation of large-area illumination using low-cost precursors and fabrication techniques.

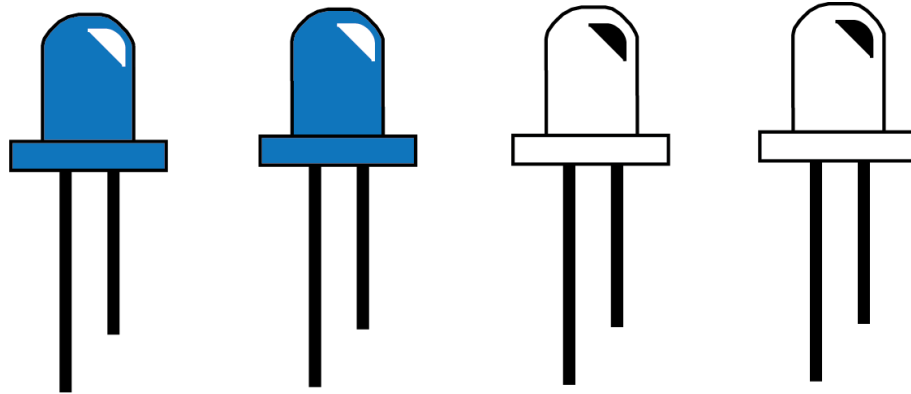
Chapter 4: Metal halide perovskites are being extensively studied due to their optoelectronic properties, making them promising for the next generation of emitters. The ability to synthesize these materials by solution-processed methods makes them particularly suitable for large-area emitting devices. We made perovskites films based on the quantum-confined system of 2D-3D Ruddlesden-Popper (RP) perovskites phases, which allows to reach emission in the blue. The spin cast films were comprised of a nominal composition of $\text{PEA}_2(\text{Cs}_{0.75}\text{MA}_{0.25})\text{Pb}_2\text{Br}_7$ as reference. By the addition of isopropylammonium (iPAm) to the perovskites, we were able to further tune the emission toward the blue and enhance the luminescence quantum yields. Both reference and iPAm-modified perovskite layers were optical and structural characterized, finding them constituted of different RP perovskite phases spanning from purely 2D to $N \geq 5$. As revealed by the optical characterization, the enhancement of the blue emission in the iPAm-modified perovskite layer is due to the suppression of energy transfer toward lower band gap phases. Moreover, the crystallization of these domains is affected by the additive's addition, which alters the relative composition of the different phases besides promoting a more random distribution of the crystallites. As a consequence, the charge transport in the direction perpendicular to the perovskite layer is improved. Fabricated perovskite-based LEDs with an iPAm-modified layer exhibit a bright blue emission with an average EL of 483 nm and a luminance above 8000 cd m^{-2} at an applied voltage of 6.5 V (20.6 mA cm^{-2}). Additionally, we evaluated the colorimetric characteristics of our champion device, finding a high color purity of 88%. Finally, this champion device reached a compelling external quantum efficiency of 6 % and a maximum current efficiency of 38 cd/A. These results suggest that using RP perovskite phases and iPAm as additive is a viable route to achieve high-efficiency blue LEDs as required for self-emissive displays and large-area illumination applications.

1.6 References

- [1] H. J. Round, *Semiconductor Devices: Pioneering Papers* **1991**, 879.
- [2] N. Zheludev, *Nat. Photonics* **2007**, *1*, 189.
- [3] S. Larach, R. E. Shrader, *Phys. Rev.* **1956**, *102*, 582.
- [4] J. Black, H. Lockwood, S. Mayburg, *J. Appl. Phys.* **1963**, *34*, 178.
- [5] G. A. Wolff, R. A. Hebert, J. D. Broder, *Phys. Rev.* **1955**, *100*, 1144.
- [6] R. W. Smith, *Phys. Rev.* **1955**, *100*, 760.
- [7] E. F. Apple, J. S. Prener, *J. Phys. Chem. Solids* **1960**, *13*, 81.
- [8] H. K. Henisch, *Reports Prog. Phys.* **1964**, *27*, 369.
- [9] P. D. Rack, P. H. Holloway, *Mater. Sci. Eng. R Reports*, **1998**, *21*, 171.
- [10] A. H. Kitai, In *Principles of Solar Cells, LEDs and Related Devices*, Jonh Wiley & Son Ltd, **2019**, pp. 111–161.
- [11] S.M. Sze, In *Physics of Semiconductor Devices*, John Wiley and Sons Inc, **1981**, pp. 743–789.
- [12] C. Munasinghe, J. Heikenfeld, R. Dorey, R. Whatmore, J. P. Bender, J. F. Wager, A. J. Steckl, *IEEE Trans. Electron Devices* **2005**, *52*, 194.
- [13] A. H. Kitai, F. Chen, In *Handbook of Visual Display Technology*, Springer Berlin Heidelberg, **2012**, pp. 1183–1192.
- [14] M. Fox, In *Optical Properties of Solids*, Oxford University Press, Oxford, **2010**, pp. 113–138.
- [15] D. A. Davies, A. Vecht, J. Silver, P. J. Marsh, J. A. Rose, *J. Electrochem. Soc.* **2000**, *147*, 765.
- [16] Y. Shi, Y. Wen, M. Que, G. Zhu, Y. Wang, *Dalt. Trans.* **2014**, *43*, 2418.
- [17] P. F. Smet, I. Moreels, Z. Hens, D. Poelman, *Materials (Basel)*. **2010**, *3*, 2834.
- [18] M. Pal, N. R. Mathews, E. R. Morales, J. M. Gracia Y Jiménez, X. Mathew, *Opt. Mater. (Amst)*. **2013**, *35*, 2664.

- [19] A. Garrido-Hernández, D. Y. Medina-Velazquez, A. S. d. I. y. d. la Torre, A. de J. Morales-Ramírez, M. Molina-Morales, M. A. Barrón-Meza, Y. Ramírez-Quirós, J. Reyes-Miranda, *Mater. Sci. Semicond. Process.* **2021**, *121*, 105403.
- [20] A. Kitai, Ed., In *Luminescent Materials and Applications*, **2008**, pp. 223–248.
- [21] S. Tanaka, H. Kobayashi, H. Sasakura, Y. Hamakawa, *J. Appl. Phys.* **1976**, *47*, 5391.
- [22] E. B. Ramírez, M. Bizarro, J. C. Alonso, *Thin Solid Films* **2013**, *548*, 255.
- [23] C. Falcony, M. Garcia, A. Ortiz, J. C. Alonso, *J. Appl. Phys.* **1992**, *72*, 1525.
- [24] H. Kobayashi, S. Tanaka, *J. Soc. Inf. Disp.* **1996**, *4*, 157.
- [25] M. J. Rivera-Medina, J. Hernández-Torres, J. L. Boldú-Olaizola, J. Barreto-Rentería, J. M. Hernández-Alcántara, V. Jancik, J. C. Alonso-Huitrón, *RSC Adv.* **2016**, *6*, 107613.
- [26] V. H. López-Lugo, M. J. Rivera-Medina, J. C. Alonso-Huitrón, *Mater. Res. Express* **2021**, *8*, 036406.
- [27] Z. K. Tan, R. S. Moghaddam, M. L. Lai, P. Docampo, R. Higler, F. Deschler, M. Price, A. Sadhanala, L. M. Pazos, D. Credginton, F. Hanusch, T. Bein, H. J. Snaith, R. H. Friend, *Nat. Nanotechnol.* **2014**, *9*, 687.
- [28] S. Adjokatse, H. H. Fang, M. A. Loi, *Mater. Today* **2017**, *20*, 413.
- [29] G. Grancini, M. K. Nazeeruddin, *Nat. Rev. Mater.* **2019**, *4*, 4.
- [30] V. D’Innocenzo, A. R. Srimath Kandada, M. De Bastiani, M. Gandini, A. Petrozza, *J. Am. Chem. Soc.* **2014**, *136*, 17730.
- [31] Y. Liu, Z. Yang, D. Cui, X. Ren, J. Sun, X. Liu, J. Zhang, Q. Wei, H. Fan, F. Yu, X. Zhang, C. Zhao, S. F. Liu, *Adv. Mater.* **2015**, *27*, 5176.
- [32] L. Protesescu, S. Yakunin, M. I. Bodnarchuk, F. Krieg, R. Caputo, C. H. Hendon, R. X. Yang, A. Walsh, M. V Kovalenko, *Nano Lett* **2015**, *15*, 39.
- [33] B. Saparov, D. B. Mitzi, *Chem. Rev.* **2016**, *116*, 4558.
- [34] D. H. Foster, In *Encyclopedia of the Eye*, **2010**, pp. 266-274.
- [35] R. J. Mortimer, T. S. Varley, *Dye. Pigment.* **2011**, *89*, 169.

Chapter 2



A chalcogenide-based phosphor: Europium-doped ZnS nanocrystalline thin films with a strong blue PL

Chalcogenides-based phosphors have played an important role in alternating current-driven electroluminescent (EL) devices. The host semiconductor (ZnS) and the dopants as color centers (europium) have to be compatible (host lattice interactions) to secure the light emission in an EL device.

This chapter describes the synthesis of europium-based ZnS thin films deposited by the pyrosol method from solution-based sources. It presents crystallographic, morphological, and optical characterization of a strong blue-emitting phosphor, namely ZnS:Eu²⁺. Additionally, it unveils the film formation and the in-situ reduction of Eu³⁺ to Eu²⁺ during the synthesis. Furthermore, it gives a general understanding of how the Eu²⁺ ion affects the surrounding of the host material, which explains the origin of the blue emission by proposing a simplified energy band and energy levels diagram for Eu²⁺ ions incorporated in ZnS as thin films.

This chapter is based mainly on the publication *Rivera-Medina M.J. et al. RCS Adv.*, **2016**, 6, 107613-107621 with the incorporation of the crystal field splitting and neuphelauxetic effect theory adapted from our recent publication *López-Lugo V.H. et al. Mater. Res. Express*, **2021**, 8, 036406.

2.1 Introduction

Rare-earth doped phosphors have been of significant importance in developing a wide variety of modern luminescent devices. By incorporating ions of europium and cerium into a host semiconductor, it is possible to make activated inorganic phosphors that emit through the whole visible spectrum.^[1] For example, divalent europium has been intensively investigated as a blue-green-emitting activator in a wide variety of host materials in the form of powders, nanoparticles or nanocrystals, and thin films; however, the origin of its blue-emission is still under study.^[2-12]

The nature of the broadband photoluminescence (PL) of Eu^{2+} ion is due to parity allowed electric dipole transition between $4f^65d^1$ excited states and $4f^7$ ground states. The energy of its first transition is around 4.2 eV (295 nm or 33871 cm^{-1}). However, when a crystalline host surrounds Eu^{2+} , its energy is perturbed. The photoluminescence spectral tuning is because the excited 5d orbitals are strongly affected by the surrounding anion ligands, whereas the well-shielded 4f levels are barely altered. In fact, an extensive compilation has been done for Eu^{2+} in more than 300 inorganic host lattices, reporting emissions in the whole visible spectrum.^[13] Surprisingly, this compilation excludes a very well-known host semiconductor, namely ZnS, despite that 35 Eu-doped sulfide compounds were studied, and pioneer investigations on Eu-doped ZnS were already published.^[14-16] These previous reports indicated the presence of Eu^{2+} in single crystals of wurtzite through electron spin resonance (ESR), suggesting that a direct substitution of Eu^{2+} to Zn^{2+} has taken place; hence, no charge compensation was required.

All these previous reports motivated us to study the PL characteristics of the $\text{ZnS}:\text{Eu}^{2+}$ system in a wide variety of nanocrystals, nanoparticles, and nanowires.^[9,17,26,18-25] These nanostructures may present green-to-blue emission (or a mixture of thereof), depending on many factors, such as the methods employed to synthesize the nanostructures and post-synthesis treatments. Nonetheless, most of the synthesis techniques involve long and complicated processes and post-synthesis treatments. Moreover, a reductant agent for the Eu ion is commonly required.

Here we report the strong blue photoluminescence from ZnS:Eu²⁺ thin films synthesized by a simple, fast and, cheap ultrasonic spray pyrolysis method. These films have potential applications for the development of high-intensity miniature electroluminescent displays.

2.2 Experimental section

2.2.1 Preparation of the thin films

The ZnS:Eu²⁺ films were deposited on glass substrates by the ultrasonic spray pyrolysis technique at atmospheric pressure. The starting precursor solution was prepared by mixing in solids 3.3 mmol of zinc acetate dihydrate, 5 mmol of 1,3-dimethyl-2-thiourea, and 0.10 mmol of europium chloride hexahydrate. The solid mixture was dissolved in anhydrous methanol (three parts), deionized water (one part), and acetic acid (5%). The substrate temperature was 450°C. The carrier and directing gas used was air at constant flow rates fixed at 1.5 L min⁻¹ and 0.3 L min⁻¹, respectively. Under these deposition conditions, ~550 nm thick ZnS:Eu²⁺ films were produced. All reagents were purchased from Sigma Aldrich and used as received without further purification. The air used during the deposition of the films was provided from an oil-free air compressor. Un-doped ZnS films were deposited under the same conditions.

2.2.2 Characterization of the thin films

The thermogravimetric analyses (TGA) were performed for all precursors salts, using a TGA Q50000 V3.15 equipment from TA Instruments. Two heating constant rates were used, 10°C min⁻¹ for 1,3-dimethyl-2-thiourea and zinc acetate and 20°C min⁻¹ for europium (III) chloride. The TGA were carried out using air as the chamber gas.

The crystalline structure of the films was characterized by X-ray diffraction (XRD) using a Bragg-Brentano Rigaku ULTIMA IV diffractometer with an X-ray source of Cu *K* α line (0.15406 nm), at a grazing beam configuration (incidence angle of 1°).

The morphology of the films was investigated by scanning electron microscopy (SEM) using a JEOL 7600 F field-emission scanning electron microscope with operating voltages of 2 kV and 3 kV for planar view, and angular view measurements, respectively.

The steady-state PL characteristics, namely excitation and emission spectra, were recorded at room temperature using a Spex Fluoromax spectrofluorometer (200 to 850 nm) using a xenon lamp as the excitation source. Additionally, some PL spectra were also obtained through a Kimmon He-Cd laser using a 325 nm unfocused beam at fixed power of 25mW coupled with an optical fiber to the spectrofluorometer.

Electron spin resonance (ESR) measurements for detecting Eu^{2+} , in the ZnS:Eu^{2+} films, were performed through a JEOL (JES-RE3X) ESR-X-spectrometer, equipped with a rectangular cavity and a gas flow cryostat with a working temperature range of 110 to 300 K. The Eu^{2+} ESR spectrum was obtained at 113 K (-160°C) using a resonance frequency of 9.1 GHz and a magnetic field centered at 330 mT. For the ESR measurements, the ZnS:Eu^{2+} films were deposited on KCl single crystalline substrates to avoid the presence of spurious ESR signals due to the paramagnetic impurities (mainly Mn^{2+} and Fe^{2+}) contained in the glass substrates.

2.3 Results and discussion

2.3.1 Film growth

One of the key parameters for depositing chalcogenides-based thin films is the temperature of the substrate. The pyrosol technique requires an optimal temperature where the salt precursors are decomposed to subsequently react, forming the desired compound. Thermogravimetric analyses (TGA), namely percentage in weight loss (TG) and its derivate (DTG) were performed to determine the optimal temperature for the substrate. The obtained TGA curves are shown figure 2.1

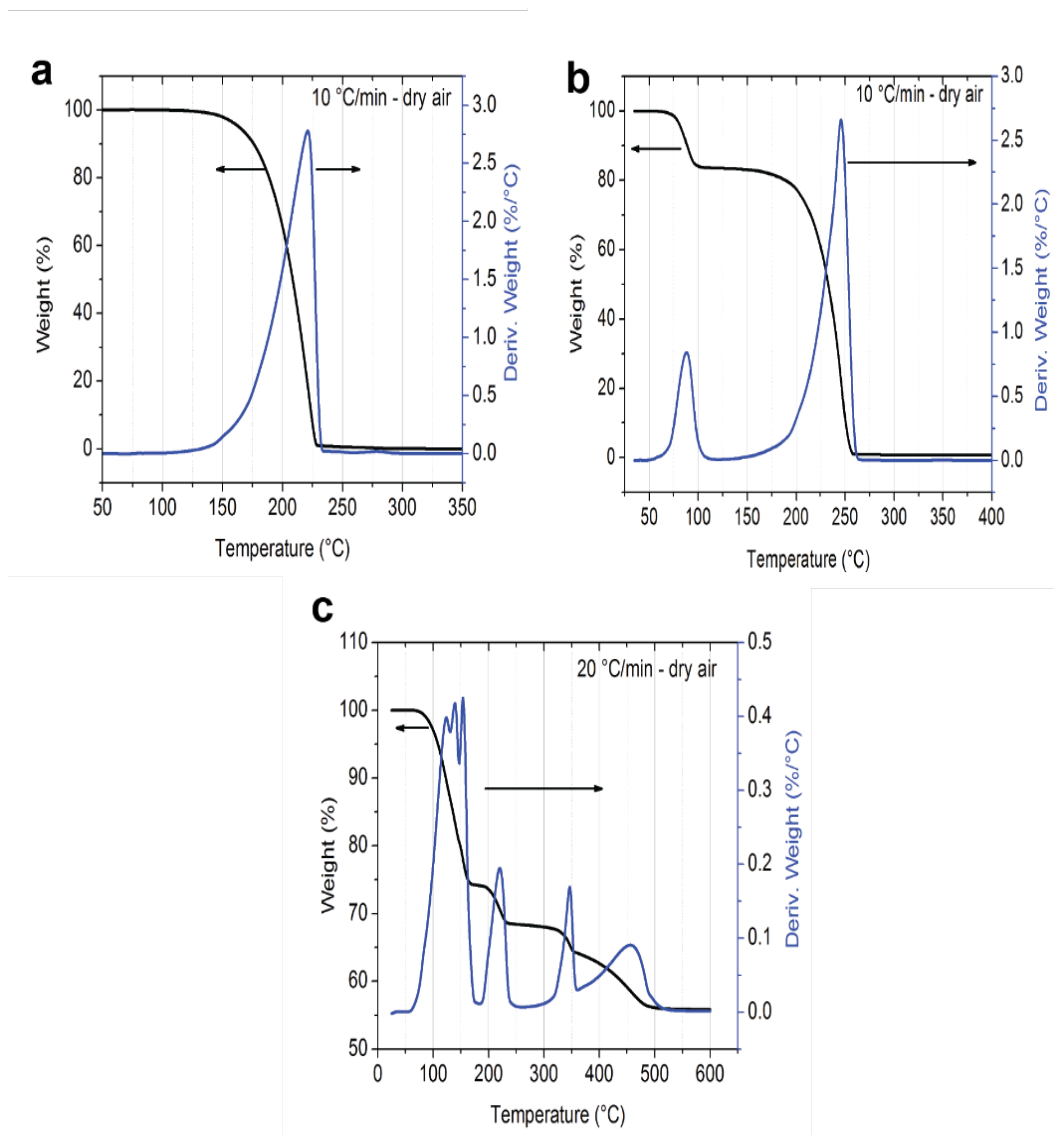


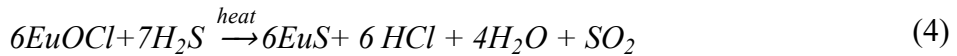
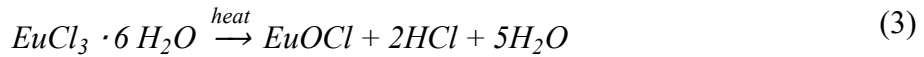
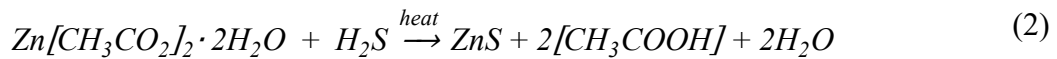
Figure 2.1 TG-DTG curves for the (a) 1,3-Dimethyl-2-thiourea; (b) zinc acetate dihydrate and (c) europium (III) chloride hexahydrate precursors, evaluated at 10 and 20 °C/min heating rate for a, b and c, respectively. The measurements were carried out in a dry air atmosphere.

The TGA curve in figure 2.1(a) shows a one-step thermal decomposition of 1,3-dimethyl-2-thiourea. A constant weight loss begins at 100°C and ends at ~235°C, where it completely decomposed. Zinc acetate dihydrate decomposes in two steps. The first mass loss corresponds to two water molecules of hydration; the remaining step corresponds to the decomposition of the molecule at ~250°C. It is noteworthy that 1,3-dimethyl-2-thiourea is commonly used as the

source of sulfur-based precursor salts for sulfide compounds deposited as thin films using the ultrasonic spray pyrolysis technique. It was proposed as the source of hydrogen sulfide as it is released by its acidic hydrolysis at high temperatures avoiding the precipitation of zinc and europium sulfides in the solution. The driving force for the hydrolysis is the difference between the C=S ($\Delta_f H^\circ_{298} = 573$ kJ/mol) and C=O ($\Delta_f H^\circ_{298} = 789$ kJ/mol) bond enthalpies.

Europium chloride has a rather complex behavior in comparison with the previous precursor salts as depict in figure 2.1 (c). First, it undergoes stepwise dehydration to $\text{EuCl}_3 \cdot \text{H}_2\text{O}$ (25% mass loss); later, complex hydrolytic reactions occur resulting in the formation of different mixed chloride hydroxide special until EuCl_2OH is formed (further 11 % mass loss). The final product at 475 °C is the solid EuOCl , which can be recovered from the crucible after the thermal analysis. This is in agreement with previously observed results.^[27,28]

When the precursor solution aerosol droplets arrive at the heated substrate, several complex hydrolytic and pyrolytic processes and reactions occur, producing many different Zn, S, and Eu species giving rise to the film formation. Based on related literature, we propose the following path to film formation of ZnS:Eu^{2+} .



In the first step, the hydrolysis of the 1,3-dimethyl-2-thiourea produces H_2S which reacts with $\text{Zn}[\text{CH}_3\text{CO}_2]_2$ and EuOCl forming the resulting ZnS:Eu^{2+} film. The europium atoms are incorporated in the ZnS framework as a substitutional impurity. An interesting event occurs during the synthesis of ZnS:Eu^{2+} as thin films. Although, we start from europium in the oxidation state III and the deposition of the films requires a certain amount of heat, plus the

presence of air, the europium gets reduced to its divalent state. This is highly counterintuitive. The exact mechanism of this behavior is, however, unclear. Nonetheless, it was recently demonstrated that from the aqueous solutions of praseodymium (III) iodine and thiourea, crystallizes an adduct of $\text{PrI}_3 \cdot 9\text{H}_2\text{O} \cdot 0.5$ thiourea. Furthermore, the thiourea has no interaction with the metal ion but rather forms hydrogen bonds with the coordinated water molecules.^[29] In acidic aqueous solutions of EuCl_3 , the europium ions form a similar hydrated cation $\text{Eu}(\text{H}_2\text{O})_6^{3+}$ and thus, direct interaction of the Eu^{3+} ions with thiourea, in the starting solution, can be discarded. On the other hand, reduction of Eu_2O_3 to EuS under H_2S atmosphere can be achieved; however, a temperature of 1150°C is needed. In this reaction, H_2S also acts as the reducing agent, and elemental sulfur is formed, but if this reaction is performed at 600°C , Eu_2S_3 and water are the only by-products.^[30] The thermal process involving H_2S generated from thiourea has been used to reduce aromatic nitro - to aminocompounds. Thus, we proposed that Eu^{3+} , most likely, in the form of EuOCl is reduced by H_2S to Eu^{2+} , forming EuS . Due to the reaction conditions, during the reduction, H_2S is probably oxidized directly to SO_2 . To the best of our knowledge, this is the first example of a direct thermal reduction of Eu^{3+} to Eu^{2+} during the synthesis of ZnS under aerobic conditions.

2.3.2 Structure, morphology and chemical composition

Figure 2.2 shows the XRD patterns for $\text{ZnS}:\text{Eu}^{2+}$ and ZnS (un-doped) thin films. These indicate that both are polycrystalline with a preferential orientation at $2\theta=28.54^\circ$, and a secondary diffraction peak at $2\theta=51.8^\circ$, which correspond to the (002) and (103) planes, respectively, of the hexagonal wurtzite ZnS crystalline structure (JCPDS card no. 80-0007). All the other smaller XRD peaks also correspond to the hexagonal phase of ZnS . The average crystallite size (D) of each film was assessed using the Debye-Scherrer formula for (002), as well as the lattice parameters for the hexagonal structure (a and c). These were found to be: $D = 24$ nm, $a=3.862$ Å, $c=6.225$ Å and $D = 24.8$ nm, $a=3.830$ Å, $c=6.240$ Å, for the $\text{ZnS}:\text{Eu}^{2+}$ and ZnS films, respectively. The structure of the $\text{ZnS}:\text{Eu}^{2+}$ film is consistent with previously reported investigations, which argued that Eu enters in the hexagonal wurtzite lattice of ZnS bulk crystals, as Eu^{2+} , substituting Zn^{2+} .^[9,15,24,26]

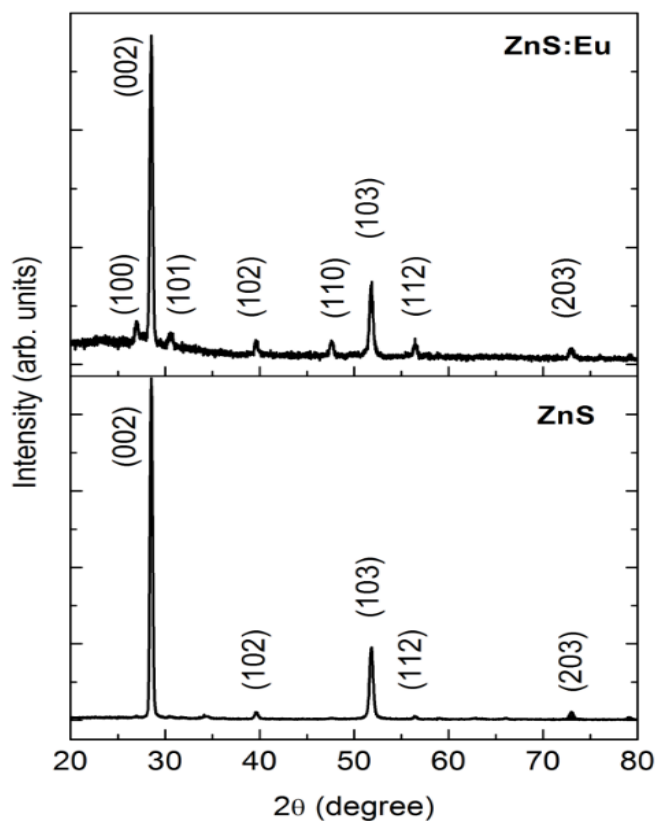


Figure 2.2 X-ray diffraction patterns for the ZnS and ZnS:Eu²⁺ films, as deposited by ultrasonic spray pyrolysis, at substrate temperature of 450 °C.

The variations in the lattice parameters are expected since the ionic radius of Eu²⁺ (0.95 Å) is larger than that of Zn²⁺ ion (0.74 Å),^[31,32] and when the Eu²⁺ ions replace the Zn²⁺ ions, a lattice distortion in the structure is produced.^[24] However, the small variations in these parameters indicate that the amount of Eu²⁺ ions incorporated in the ZnS matrix is rather small.

Figure 2.3 depicts the FE-SEM micrographs for the ZnS and ZnS:Eu²⁺ films with planar surface and angled views. ZnS thin films consist of well-packed hexagonal-shaped bars with diameters ranging from 100 to 300 nm, mainly oriented on the z-axis, perpendicular to the substrate as shown in the planar (a) and angled (b) views of figure 2.3. Similarly, ZnS:Eu²⁺ films grow in the form of hexagonal bars but with smaller diameters (50-200 nm). The micrographs

corresponding to these films are shown in figure 2.3 (c) and (d). The regular and highly oriented hexagonal structures observed in the FE-SEM images are in good agreement with the wurtzite phase and preferential orientation observed in the XRD diffractograms. Thus, both films are comprised of crystalline grains aggregates given rise to the formation of hexagonal bars with preferential growth perpendicular to the substrate.

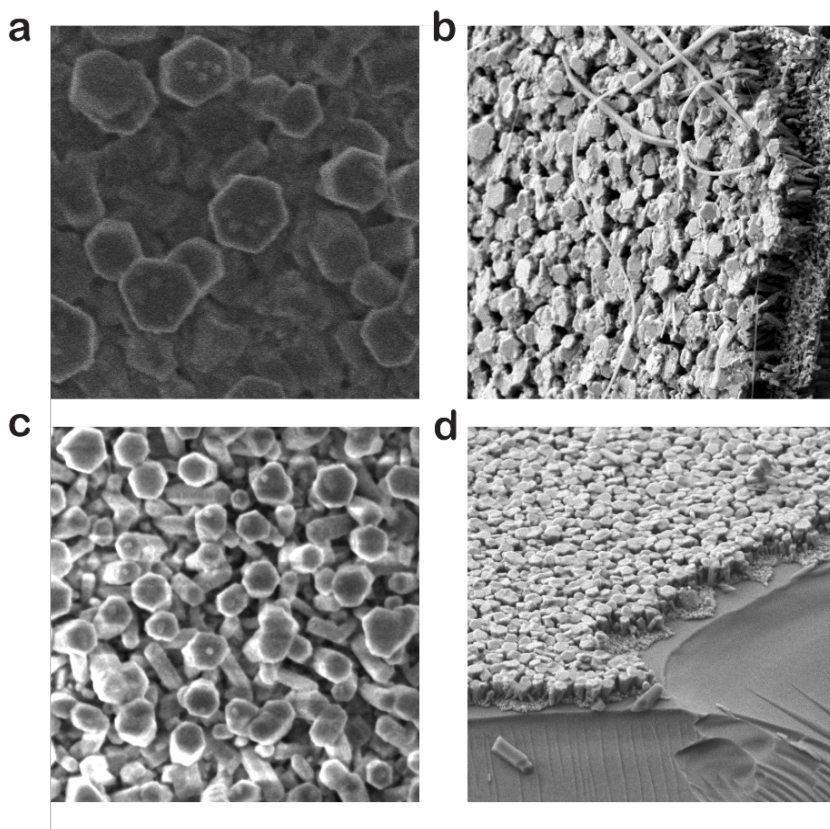


Figure 2.3 SEM micrographs for the ZnS and ZnS:Eu²⁺ films deposited by USP. Top row: ZnS film (a) planar view and (b) cross view with a rotation of 188.4° and 6.1° of tilt angle. Bottom row: ZnS:Eu²⁺ film (c) planar view and (d) cross view with a rotation of 94.6° and 8.0° of tilt angle.

An attempt was made to detect the Eu atoms incorporated the ZnS:Eu²⁺ films by techniques such as X-ray photoelectron spectroscopy and energy dispersive spectroscopy. However, the absence of any signal related to Eu in the spectra obtained for the analyzed films, indicated that the amount of Eu incorporated in the ZnS matrix of the films was below the limit of detection (~1 at.%) of the equipment utilized for these analyses. The low concentration of Eu in our ZnS:Eu²⁺ films is also consistent with the low limit of solubility reported for Eu in ZnS single

crystals.^[15] In order to confirm the existence of trace amounts of Eu^{2+} in the $\text{ZnS}:\text{Eu}^{2+}$ films, ESR measurements were carried out.

The presence of Eu^{2+} ions was confirmed as depicted in figure 2.4. The main signal is located at 325.2 mT with a g-value of 2.0, which is consistent with related studies of substituting Zn^{2+} sites, in the wurtzite phase of ZnS lattice, for Eu^{2+} sites. ^[15,22] As it is known, any ESR signal associated with europium is originated from Eu^{2+} ions in the $4f^7 [^7S_{7/2}]$ ground state configuration.^[33]

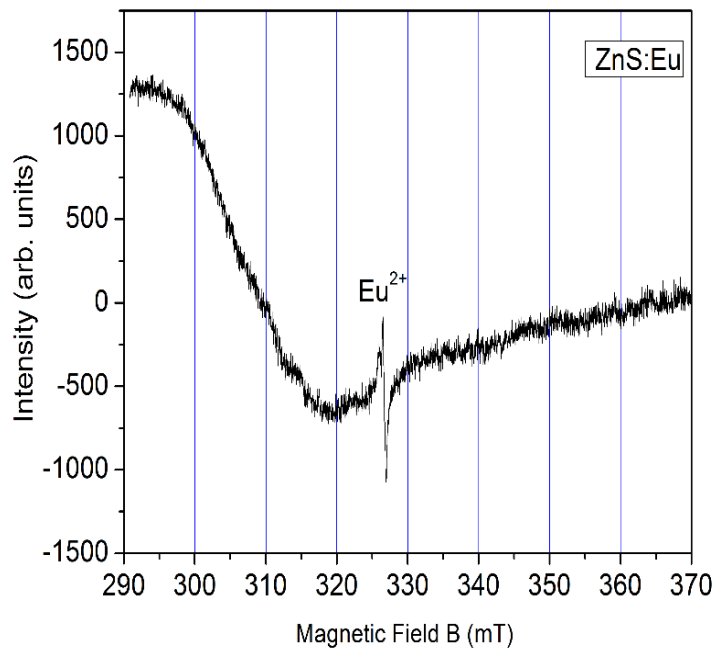


Figure 2.4 Electron spin resonance (ESR) spectrum of the $\text{ZnS}:\text{Eu}^{2+}$ film measured at 113 K (-160°C) using a resonance frequency of 9.1 GHz and a magnetic field centered at 330 mT. The ESR line of Eu^{2+} is observed at 325.2 mT.

2.3.3 Optical properties

The optical properties of both un-doped ZnS and ZnS:Eu²⁺ are shown in figure 2.5. The absorbance spectra for both films are depicted in panel (a). The sharp peaks located at 330 nm are assigned to interband or band-edge absorption of the host ZnS. In other words, photons with an energy of around 3.75 eV excite the electrons from the valance band (VB) to the conduction band (CB). Rather small variations have been observed for bulk ZnS crystals with a direct band gap of 3.68-3.77 eV.^[34-37] Nonetheless, the ZnS:Eu²⁺ peak is slightly broaden compared to the un-doped ZnS. After resolving the peak by subtracting both spectra (inset), an unknown feature appears. We assumed that after the incorporation of Eu²⁺ ions, new energy levels are created within the gap. Recently, it was observed that when Eu²⁺ ions are incorporated in compounds with charge (II) cations, they remain stable on the divalent site and the energy of the lowest Eu²⁺ 4f⁶5d level is always below the bottom of the conduction band of the compound.^{[13][38]} Additionally, our XRD and ESR results corroborate the presence of Eu²⁺ ions in the ZnS films, which are occupying the divalent Zn²⁺ sites. Therefore, we can assess the broadening to the absorption of photons that generate transitions of electrons from the valence band of the ZnS matrix to the Eu²⁺ 4f⁶5d levels located ~0.19 eV below the bottom of the conduction band of the ZnS compound.

Additionally, for the undoped-thin film, a second peak with a lower energy of 3.37 eV (367 nm) is attributed to the VB – localized donor states absorption. These donor sites tend to reside below the conduction band; they are originated by vacancies of sulfur or interstitial atoms of zinc.

The effect of Eu when doping ZnS is clearly observable with the naked eye as depicted in figure 2.5 (b) and (c). The films were excited under UV irradiation of 254 nm in a bright room and in a dark room. As can be seen, the ZnS:Eu²⁺ shows a strong blue emission even with ambient light, whereas the ZnS film only reflects and/or scatters light.

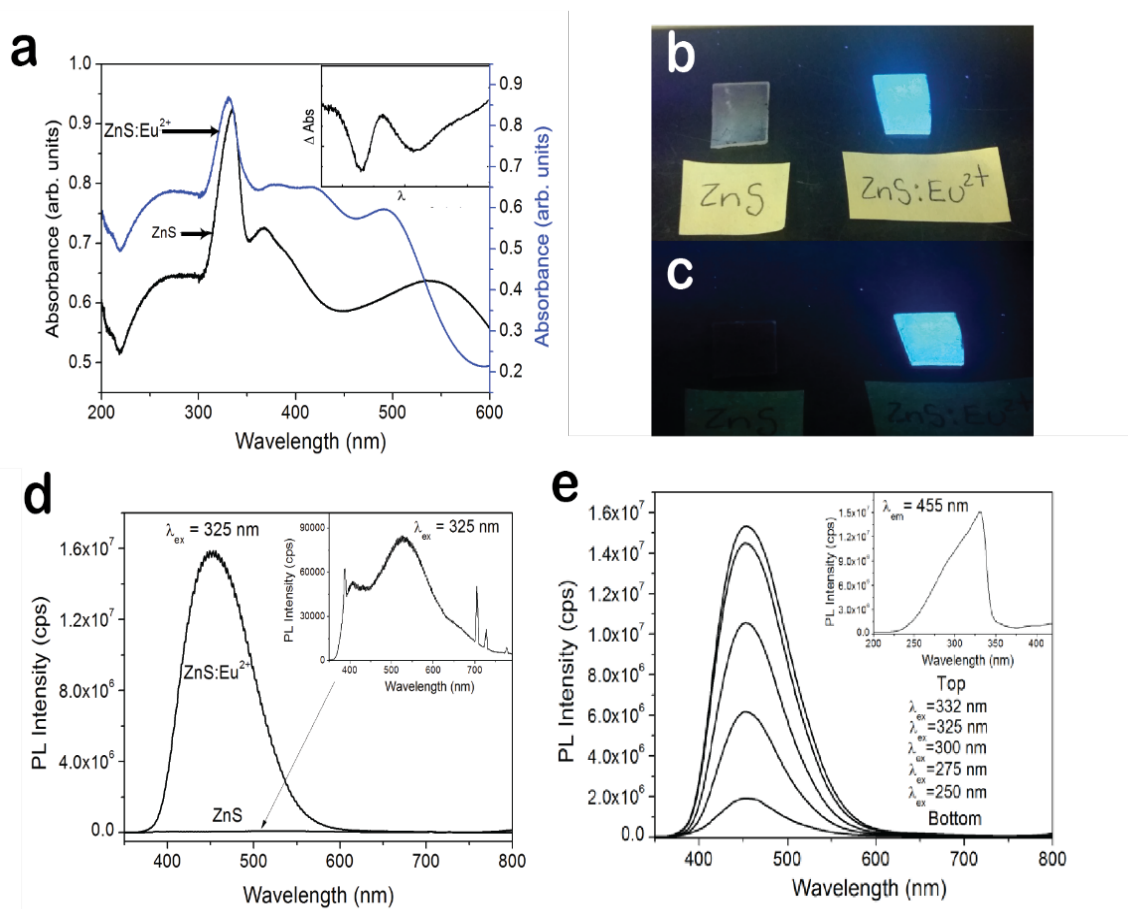


Figure 2.5 Optical characteristics of ZnS:Eu²⁺ and ZnS. (a) UV-vis absorbance spectra. The inset shows the absorbance spectrum for Eu²⁺. (b,c) Photographs of ZnS and ZnS:Eu²⁺ thin films being excited with a UV radiation of 254 nm, in a bright and dark room, respectively. (d) Steady-state PL for both films with an excitation wavelength of 325 nm. The inset shows a close-up for the ZnS film. (e) Steady-state PL for ZnS:Eu²⁺ at different excitation energies and PLE with λ_{em} of 455 nm is displayed in the inset.

The steady-state PL spectra of both films are shown in figure 2.5 (d). The PL of ZnS:Eu²⁺ is 185-times fold higher compared to ZnS. The intensity is considerably high that superimposed the broad emission located at 527 nm, which is observed for the ZnS (inset). This green broad-band can be assigned to the radiative electron transfer from sulfur vacancies to interstitial sulfur states.^[9,39] The strong blue PL from the ZnS:Eu²⁺ films consists of a broad emission centered at 455 nm, with a full-width at half-maximum (FWHM) of approximately 94 nm. We performed additional PL measurements [figure 2.5 (e)] at different excitation wavelengths, as expected the

PL intensity increases as the excitation wavelength rises from 250 to 332 nm. It worth mentioning, that the position of the peak is maintained around 455 nm (2.73 eV). The excitation spectrum (PLE) recorded at an emission wavelength of 455 nm is depicted in the inset of figure 2.5 (e). It corroborates that the maximum intensity of the PL peak at 455 nm is obtained for the excitation wavelength of $\lambda_{\text{exc}}=332$ nm. This excitation wavelength corresponds to photons with energy equal to 3.75 eV, i.e., the band gap of the ZnS:Eu²⁺. Therefore, we concluded that band-to-band absorption from the VB to the CB of the host lattice of ZnS first takes place to later efficiently be transferred to the Eu²⁺ activator.^[40]

According to the compilation made by P. Dorenbos on the d-f emission spectra of Eu²⁺ in inorganic compounds, there are three distinguishable emissions for Eu²⁺. Namely, (1) normal broad band dipole and spin allowed d-f emission, (2) ff narrow, and (3) “anomalous” Eu²⁺ emission.^[13] To determinate the governing mechanism of our system ZnS:Eu²⁺, a quantitative study was recently performed. The full study can be found elsewhere.^[41] Our findings suggest that the emission of Eu²⁺ mainly arises from 5d →4f transitions. As the 5d electronic level is not shielded from the surrounding ligands, its energy is reduced by the combined effect of the centroid shift and the crystal field splitting of the 5d states. The centroid shift by nephelauxetic effect is the lowering of the 5d states average energy compared to a free ion. The centroid shift is large when Eu is coordinated by S ions because the S²⁻ ligands are at the end of the nephelauxetic series and have better tendency for covalent bonds. We found that the total redshift of the gap energy between 5d and 4f levels with respect to those of the free Eu²⁺ in vacuum (E_g=4.2 eV) is owing to the crystal effect (0.32 eV), nephelauxetic (0.65eV), and stoke shift (0.5 eV). These results support the blue PL emission at 2.73 eV, derivate from Eu²⁺ ions when are incorporated in a host matrix of ZnS films. Based on the experimental results and our calculations, we built the simplified energy band and energy levels diagram depicted in figure 2.6, which helps to model the excitation-emission mechanisms of the luminescence of the Eu²⁺ ions incorporated in the ZnS films.

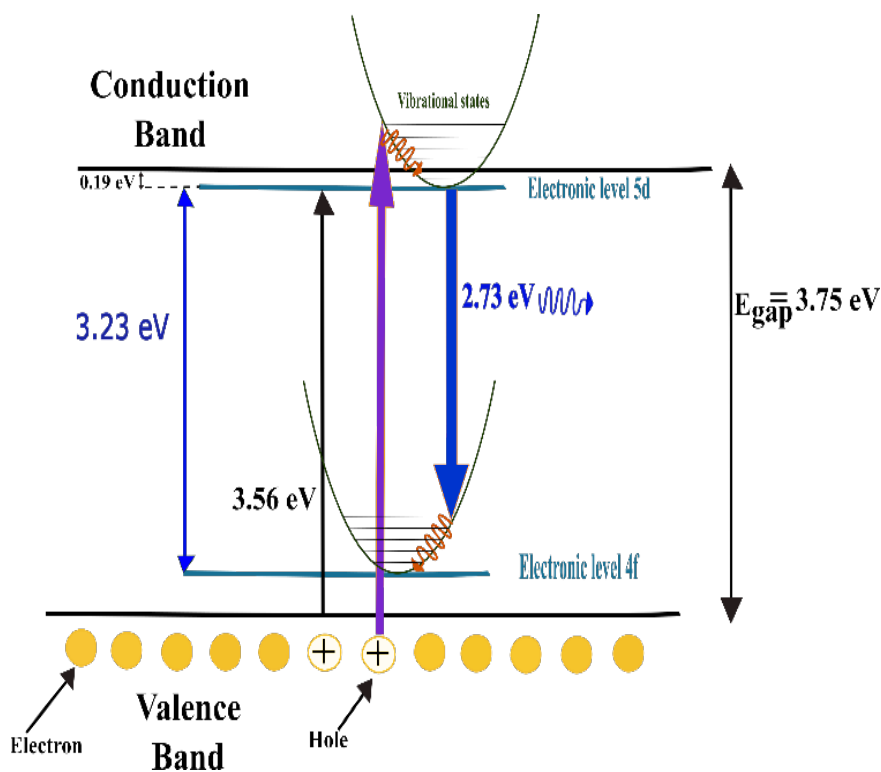


Figure 2.6 Simplified energy band and energy levels diagram for Eu^{2+} ions incorporated in ZnS films.

2.4 Conclusions

ZnS:Eu²⁺ thin films with an intense blue PL at room temperature have been successfully synthesized by a simple and fast ultrasonic spray pyrolysis method. The as-deposited ZnS:Eu²⁺ films are composed of hexagonal wurtzite nanocrystals with an average size of ~ 28 nm, which agglomerate to form hexagonal facet nanobars. The incorporation of the Eu dopant atoms in the valence state Eu²⁺ was confirmed by ESR measurements. These measurements along with the absorption and PL characteristics of the films indicate that the efficient blue luminescent comes from intra-ion transitions of Eu²⁺ ions incorporated in the wurtzite ZnS matrix. The high intensity and the emitting color of these ZnS:Eu²⁺ films, deposited by this relatively simple and cheap pyrolysis technique, ensures their potential application as ideal candidates for modern flat panel electroluminescent displays.

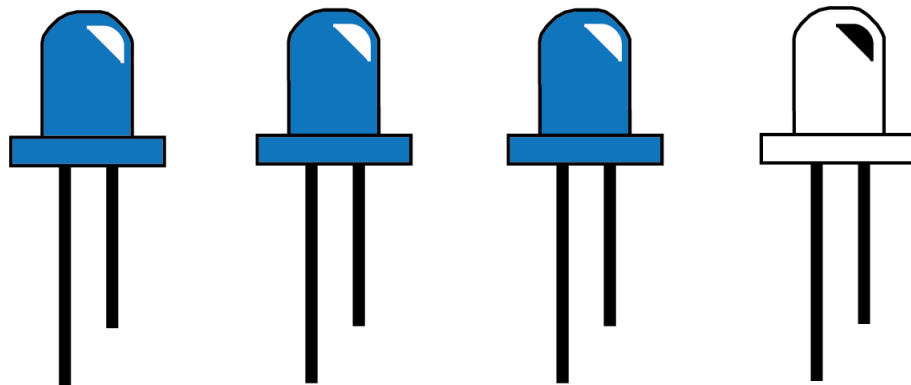
2.5 References

- [1] G. Li, Y. Tian, Y. Zhao, J. Lin, *Chem. Soc. Rev.* **2015**, *44*, 8688.
- [2] B. Park, S. J. Kim, J. Lim, S. Some, J. Park, S. Kim, C. Kim, T. J. Lee, S. C. Jun, *J. Mater. Chem. C* **2015**, *3*, 4030.
- [3] Z. C. Wu, H. H. Fu, J. Liu, S. P. Kuang, M. M. Wu, J. G. Xu, X. J. Kuang, *RSC Adv.* **2015**, *5*, 42714.
- [4] J. Hao, M. Cocivera, *Appl. Phys. Lett.* **2001**, *79*, 740.
- [5] Z. Tao, Y. Huang, P. Cai, S. Il Kim, H. J. Seo, *Opt. Mater. (Amst)*. **2014**, *37*, 287.
- [6] S. J. Gwak, P. Arunkumar, W. Bin Im, *J. Phys. Chem. C* **2014**, *118*, 2686.
- [7] X. Zhang, F. Meng, W. Li, H. J. Seo, *Ceram. Int.* **2013**, *39*, 8975.
- [8] X. Yang, T. S. Tiam, X. Yu, H. V. Demir, X. W. Sun, *ACS Appl. Mater. Interfaces* **2011**, *3*, 4431.
- [9] X. Zhang, L. Wang, *Chalcogenide Lett.* **2015**, *12*, 435.
- [10] H. Zhu, Y. Liu, D. Yan, H. Bian, S. Li, C. Liu, C. Xu, X. Wang, *Opt. Mater. (Amst)*. **2014**, *36*, 1771.
- [11] K. Miura, Y. Arai, O. Hanaizumi, *Mater. Sci. Appl.* **2015**, *06*, 676.
- [12] J. Hao, J. Gao, M. Cocivera, *Appl. Phys. Lett.* **2003**, *82*, 2778.
- [13] P. Dorenbos, *J. Lumin.* **2003**, *104*, 239.
- [14] M. Godlewski, D. Hommel, *Phys. Status Solidi* **1986**, *95*, 261.
- [15] K. Swiatek, M. Godlewski, D. Hommel, H. Hartmann, *Phys. Status Solidi* **1989**, *114*, 127.
- [16] K. Swiatek, M. Godlewski, D. Hommel, *Physical Rev. B* **1990**, *42*, 3628.
- [17] S. J. Xu, S. J. Chua, B. Liu, L. M. Gan, C. H. Chew, G. Q. Xu, *Appl. Phys. Lett.* **1998**, *73*, 478.
- [18] S. Liu, H. Q. Guo, Z. H. Zhang, F. Q. Liu, Z. G. Wang, *Chinese Phys. Lett.* **2000**, *17*, 609.

- [19] W. Chen, J.O. Malm, V. Zwiller, Y. Huang, S. Liu, R. Wallenberg, J.-O. Bovin, L. Samuelson, *Phys. Rev. B* **2000**, *61*, 11021.
- [20] W. Chen, J. O. Malm, V. Zwiller, R. Wallenberg, J. O. Bovin, *J. Appl. Phys.* **2001**, *89*, 2671.
- [21] G. Sharma, S. Do Han, S. P. Khatkar, V. B. Taxak, Y. W. Rhee, *ECS Trans.* **2006**, *1*, 7.
- [22] S. Y. Lee, Y. H. Shin, Y. Kim, S. Kim, S. Ju, *J. Lumin.* **2011**, *131*, 1336.
- [23] K. Ashwini, C. Pandurangappa, B. M. Nagabhushana, *Phys. Scr.* **2012**, *85*, 065706.
- [24] K. Ashwini, Yashaswini, C. Pandurangappa, *Opt. Mater. (Amst)*. **2014**, *37*, 537.
- [25] L. Ma, K. Jiang, X. T. Liu, W. Chen, *J. Appl. Phys.* **2014**, *115*, 103104.
- [26] B. Cheng, Z. Wang, *Adv. Funct. Mater.* **2005**, *15*, 1883.
- [27] S. J. Lyle, W. A. Westall, *Thermochim. Acta* **1983**, *68*, 51.
- [28] P. A. Lawson, N. A. Stump, *Spectrosc. Lett.* **2011**, *44*, 412.
- [29] T. A. Antonenko, L. Y. Alikberova, D. V. Albov, *Acta Crystallogr. Sect. E Struct. Reports Online* **2012**, *68*, E68, m110.
- [30] R. D. Archer, W. N. Mitchel, in *Inorg. Synth.* (Ed.: E.I. Muetterties), McGraw-Hill International, **1967**, pp. 77–79.
- [31] Y. Q. Jia, *J. Solid State Chem.* **1991**, *95*, 184.
- [32] B. Y. R. D. Shannon, M. H. N. H. Baur, O. H. Gibbs, M. Eu, V. Cu, *Acta Crystallogr. Sect. A* **1976**, *32*, 751.
- [33] M. Pham-Thi, N. Ruelle, E. Tronc, D. Simons, D. Vivien, *Jpn. J. Appl. Phys.* **1994**, *33*, 1876.
- [34] H. C. Ong, R. P. H. Chang, *Appl. Phys. Lett.* **2001**, *79*, 3612.
- [35] T. Yamamoto, S. Kishimoto, S. Iida, *Phys. B Condens. Matter* **2001**, *308–310*, 916.
- [36] G. S. Harish, P. Sreedhara Reddy, *Phys. B Condens. Matter* **2015**, *473*, 48.
- [37] B. Bodo, D. Prakash, P. K. Kalita, A. X. R. D. Study, *Int. J. Appl. Phys. Math.* **2012**, *2*, 181.
- [38] P. Dorenbos, *J. Lumin.* **2008**, *128*, 578.

- [39] X. Wang, J. Shi, Z. Feng, M. Li, C. Li, *Phys. Chem. Chem. Phys.* **2011**, *13*, 4715.
- [40] G. Blasse, *J. Alloys Compd.* **1995**, *225*, 529.
- [41] V. H. López-Lugo, M. J. Rivera-Medina, J. C. Alonso-Huitrón, *Mater. Res. Express* **2021**, *8*, 036406.

Chapter 3



AC-driven electroluminescent devices: White-emission from the phosphor ZnS:Eu

Alternating current (AC)-driven electroluminescent devices have the potential advantage of being able to be directly integrated into the AC input household power supplies without the need for complicated back-end electronics involving power converters and rectifiers.

This chapter reports on the white light electroluminescence (EL) from metal-insulator-semiconductor-insulator-metal (MISIM) alternating current thin-film electroluminescent (AC-TFEL) devices fabricated by the low-cost and relatively fast and straightforward ultrasonic spray pyrolysis technique. It presents the EL modulation by varying the amplitude of the applied voltage at a fixed 10KHz sinusoidal frequency. It examines the colorimetric characteristic dependent on the variation of the electric field. Our results are closed to the standard D65 CIE¹ illuminant, which correspond to natural noon daylight. Finally, it explores the origin of white light EL by proposing an emission mechanism.

This chapter is based on the publication *Rivera-Medina M.J. et al. Mater. Chem. Phys.* **2021**, 270, 124866.

¹ CIE is the acronym in French for International Commission on Illumination. System created to mathematically represent the distribution of wavelengths in the electromagnetic spectrum as perceived by the human eye.

3.1 Introduction

The solid-state lighting and display technology scientific communities seem to be no longer interested in electroluminescent (EL) devices powered by the alternating current. A scarce number of publications have been made in the past twenty years. Perhaps this trend is because DC-driven EL devices have been successfully established as bright and efficient light sources.^[1-6] Whilst for displays, many AC-driven electroluminescent (AC-EL) technology is apparently restricted to a monochromatic emission with poor brightness performance. The truth is that there is a recent boost to develop new approaches to fabricate multicolored and white-emitting devices operated through AC inputs.^[7-14] Contrary to DC-driven EL devices, AC-EL can hold higher electric fields even with thinner and wider emission areas thanks to the capacitor-like device architecture. Among the different structures developed for AC-EL devices, thin-film AC-EL (AC-TFEL) devices have been successfully incorporated in flat panel displays required to stand extreme conditions.^[7,15-18] As described in the introductory chapter, a typical AC-TFEL structure is arranged in a MISIM configuration, where the phosphor (S) is sandwiched between two insulating layers (I) connected by a metallic and a transparent electrode (M). The phosphor layer consists of a high band gap semiconductor which serves as a host for luminescent centers. As studied in the previous chapter, ZnS is an excellent candidate as a semiconductor phosphor to host impurities of ions of rare-earth metals, such as Eu^{2+} and transition metals.^[19-22]

The fabrication of monochromatic and full-color AC-TFEL devices has been the subject of interest for more than three decades by implementing different doped-chalcogenides and oxides as phosphors.^[7,17,18,23-27] The vast majority of these AC-TFEL devices were fabricated by atomic layer deposition (ALD), RF sputtering, and electron beam evaporation. In the past, AC-TFEL devices were limited due to their low brightness performance and required expensive fabrication techniques. Additionally, white-emitting EL in AC-TFEL has been explored, resulting in an unbalanced color contrast favored by either the blue or red components. i.e., the cold-white and warm-white.^[17,18,28-31] This chapter presents the white-EL of AC-TFEL devices fabricated by a simple solution-processable method as ultrasonic spray pyrolysis. We use the blue-emitting ZnS:Eu^{2+} phosphor as our active layer in a MISIM structure.^[32,33] The colorimetric characteristics are investigated by varying the amplitude of the applied voltages at a constant 10

kHz frequency. The emission of our devices is composed of wide and narrow bands with peaks corresponding to blue, green, and red light, which together produce the resulting white light. According to the colorimetric analysis, our white light is close to the standard D65 CIE illuminant, with a minimal dominant blue component. The variation in voltage amplitude induces small changes in the visual characteristics of the EL emission. The white-EL emission of these MISIM devices is attributed to the electron-impact excitation and subsequent relaxation of the excited levels of Eu^{2+} and Eu^{3+} impurities and defect levels in the sublayer regions adjacent to the ZrO_2 - ZnS:Eu interfaces.

3.2 Experimental section

3.2.1 Materials, ultrasonic spray coating conditions and fabrication of the MISIM AC-TFEL

A 15 mm by 30 mm antimony-doped tin oxide (ATO) substrate with a sheet resistance of 96 Ω/sq was used as our transparent electrode. The substrates were ultrasonically cleaned using a soapy solution, DI water, acetone, and isopropanol for 20 minutes in each solvent. All materials were purchased and used as received without any additional treatment. A 0.05 M in concentration solution was prepared by dissolving zirconium (IV) acetylacetonate (97%) in a mixture of 9:1 volumetric ratio of anhydrous methanol (99.8%) and diethylene glycol monobutyl ether (>98%). The solution was left under constant stirring for 1 hour at room temperature. The recipe for the preparation of the ZnS:Eu precursor solution is described in the previous chapter. Details of our deposition system can be found elsewhere.^[32] Air was the transporting gas used for all our experiments; an oil-free compressor provided it.

First, we preheated our ATO substrate up to 420 °C; briefly we transported the ZrO_2 precursor solution to the reaction chamber using a 2.5 L min^{-1} carrier gas flow and 0.84 mL min^{-1} directional gas flow. Second, a ZnS:Eu thin film was grown consecutively using a carrier and directional gas flow of 2.0 L min^{-1} and 0.8 mL min^{-1} , respectively. Third, a second ZrO_2 layer was deposited on top of the phosphor using similar conditions for the previous dielectric layer. Here the top dielectric layer was treated differently before starting the film deposition by

flushing air for 30 s through the directional flow duct. Finally, aluminum (99.999%) electrodes were thermally evaporated ($5\text{-}6 \times 10^{-6}$ Torr) using a patterned shadow mask. The active area of our AC-driven devices was determined by the radius of the rear electrode (1 mm in diameter).

3.2.2 Characterization of thin films and MISIM devices

Cross-sectional scanning electron micrographs were obtained using a field-emission ultrahigh-resolution Scanning Electron Microscope JEOL JSM-7800F. Before the scanning, the samples were manually polished using a tripod polisher (South Bay Technology model 590 TEM). The AC-TFEL devices were driven by applying 10 kHz sinusoidal voltages using a Wavetek function generator, model 182A, and a step-up transformer. All peak-to-peak voltages were measured using a Hewlett Packard 1741 oscilloscope. The EL signal was collected through an optical fiber coupled to a spectrofluorometer (Spex Fluoromax) in dark ambient conditions at room temperature.

3.3 Results and discussion

3.3.1 Device structure and composition

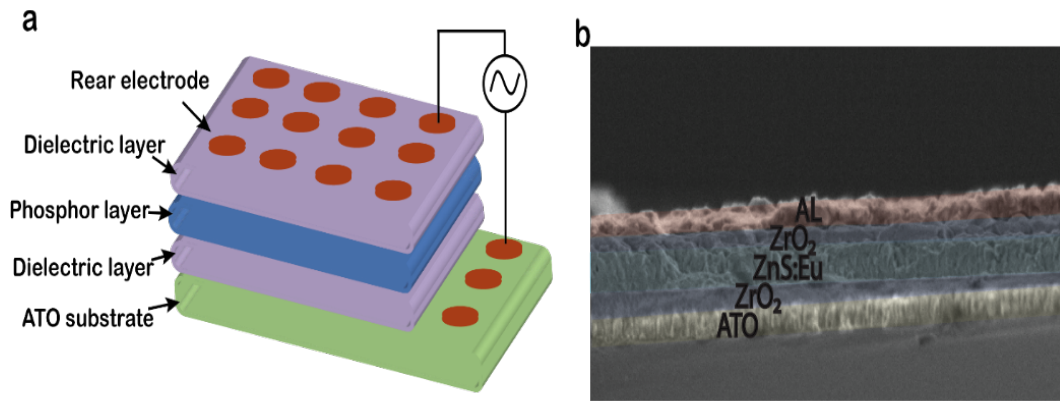


Figure 3.1 (a) Illustration of the AC-TFEL MISIM device fabricated by ultrasonic spray pyrolysis. (b) Cross-sectional image of the structure showing layer-by-layer stacking.

The fabrication of our AC-TFEL MISIM devices was carried out by the ultrasonic spray pyrolysis process, which is a rather straightforward technique. Figure 3.1 (a) shows a schematic diagram of our devices. As can be observed, aluminum electrodes were also deposited on top of the ATO substrate to ensure electrical contact properly. The device is a multilayered structure comprising of ATO (150 nm) / ZrO_2 (150 nm) / ZnS:Eu (200 nm) / ZrO_2 (150 nm) / Al (150 nm). The thicknesses were calculated by a profilometer through a systematic deposition of layer-by-layer, creating a step between each consecutive coming layer. Additionally, we performed cross-section FE-SEM measurements on one of our AC-TFEL, as depicted in figure 3.1 (b). This image reflects the imperfections, such as pinholes, impurities, particulates, etc., generally created on dielectric-phosphor-dielectric interfaces of our as-deposited devices. Since these imperfections cause micron and submicron-sized weak spots, which are susceptible to catastrophic breakdown at the voltages required for regular operation, we carried out a self-healing electrical process before acquiring the EL spectra.^[29,34] The healing process was carried out by applying rms-voltages in steps of 10 V for 10 min, from 0 V up to the threshold voltage.

3.3.2 EL modulation and colorimetric characteristics

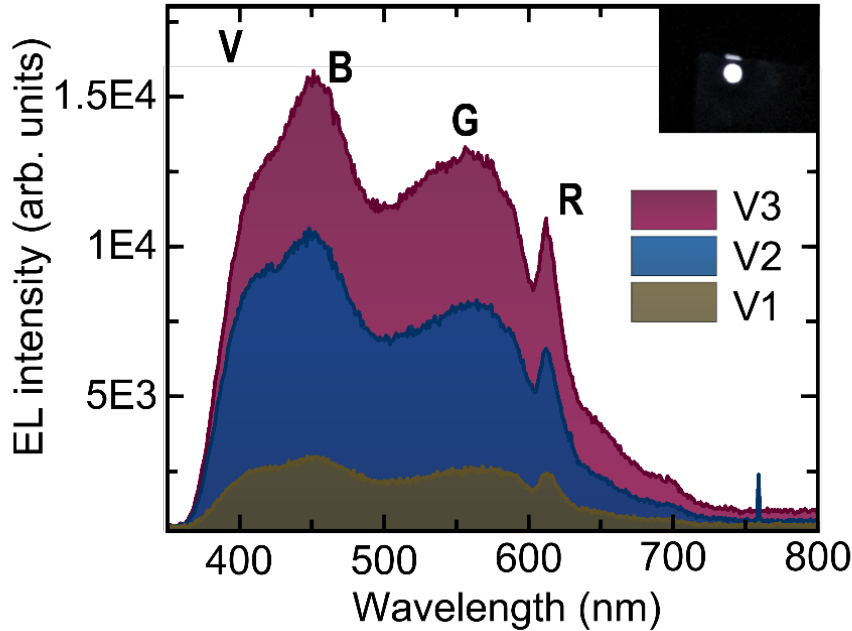


Figure 3.2 EL spectra of one of our AC-TFEL device incorporating ZnS:Eu^{2+} as phosphor. The rms-voltages are: $V_1=56\text{ V}$, $V_2=70\text{ V}$, and $V_3=77\text{ V}$. A photograph of our working device is display on the top right corner.

Figure 3.2 shows the EL spectra as function of the applied rms-voltages; $V_1=56\text{V}$, $V_2=70\text{V}$ and $V_3=77\text{V}$, in the spectral region from 350 to 800 nm. As we increase the applied rms-voltage, the overall EL emission rises. As can be observed from the spectrum corresponding to the highest voltage, the emission of our device is composed of several wide and narrow bands spanning from 400-700 nm, assigned to violet (V), blue (B), green (G), and red (R) light. The combination of all gives the resultant white EL, as illustrated in the top right corner of figure 3.2.

The white characteristics of the white EL device were analyzed employing the Commission Internationale de l'Eclairage (CIE) chromaticity coordinates. The CIE can quantitatively describe the color characteristics of any light source in terms of the three tristimulus values (X,

Y, and Z), and the corresponding mathematical relationships with the three-color matching functions \underline{x} , \underline{y} , and \underline{z} . These relationships are the following:^[35]

$$X = \int \underline{x}I(\lambda)d\lambda = \sum_{\lambda} \underline{x}I(\lambda)d\lambda \quad (1)$$

$$Y = \int \underline{y}I(\lambda)d\lambda = \sum_{\lambda} \underline{y}I(\lambda)d\lambda \quad (2)$$

$$Z = \int \underline{z}I(\lambda)d\lambda = \sum_{\lambda} \underline{z}I(\lambda)d\lambda \quad (3)$$

Where $I(\lambda)$ is the normalized spectral power distribution of the light source and λ is the wavelength of the equivalent monochromatic light. As the spectra shown in figure 3.2 are such that $I(\lambda)$ cannot be expressed analytically, the integration must be done graphically, numerically, or with mechanical methods. In our case, we used the CIE recommendation, where the integration shall be carried out by a discrete numerical sum. The computation was made using the datasheet for the CIE-1931 2-degree for color matching functions, \underline{x} , \underline{y} and \underline{z} , from Colour & Vision Research Laboratory, and a home-designed Python program. For the representation of the color in the 2D-space of the color diagram, the chromaticity coordinates x , y , and z were calculated from the following equations:

$$x = \frac{X}{X+Y+Z}; y = \frac{Y}{X+Y+Z}; z = \frac{Z}{X+Y+Z} \quad (4)$$

It must be noticed that $x+y+z=1$. Thus the color can be represented or expressed as two independent coordinates, i.e., (x,y) . The CIE coordinates corresponding to the light emitted by the AC-TFEL structure for the three applied voltages are denoted as the sample coordinates (x_s, y_s) given in table 3.1 and plotted on the CIE diagram (figure 3.3). As a

comparison, we plotted the white point $(x_i, y_i) = (0.31271, 0.32902)$ of the standard CIE illuminant D65,^[36] which is, in fact, that to the natural noon daylight for countries in Northwest Europe.

Table 3.1 CIE photometric and colorimetric characteristics of one of our AC-TFEL devices at operating rms-voltages: $V_1=56$ V, $V_2=70$ V, and $V_3=77$ V using the D65 illuminant as reference.

	x_s	y_s	Dominant λ (nm)	x_d	y_d	Color purity %	Relative Luminance Y(%)
V_1	0.298	0.314	483	0.080	0.165	5.3	74.2
V_2	0.283	0.303	482	0.080	0.162	9.6	67.8
V_3	0.290	0.317	486	0.066	0.210	10	75.5
D65	x_i	y_i	-	-	-		Y_0
	0.313	0.330				0	78.5

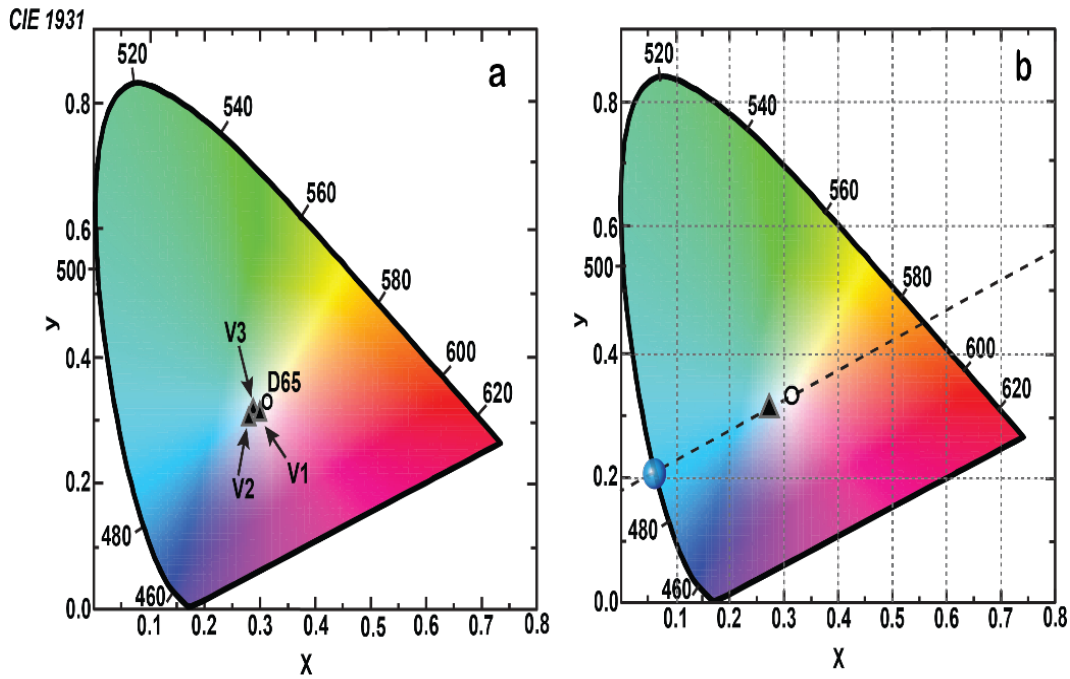


Figure 3.3 CIE chromaticity diagram of the color space coordinates of our AC-TFEL device. (a) Variation of the color coordinates as function of V_1 , V_2 , and V_3 rms-voltages with respect to the D65 illuminant. (b) Dotted line traced for the determination of the colorimetric properties at an applied rms-voltage of V_3 .

To further evaluate the visual characteristics of the white EL emission as a function of applied rms-voltage and how distant is our white-EL from the illuminant D65, we calculated the dominant wavelength and the color purity. The dominant wavelength is the single monochromatic wavelength at which the intersection occurs between the straight line starting from the white point D65, $(x_i, y_i) = (0.31271, 0.329202)$, passing through the sample point (x_s, y_s) and the locus curve with labeled hue wavelengths. The color coordinate of this dominant wavelength is denoted as (x_d, y_d) . The color purity is defined quantitatively as the ratio between the distance from the illuminant (x_i, y_i) to the point (x_s, y_s) and the distance from (x_i, y_i) to the point (x_d, y_d) corresponding to the dominant wavelength.^[37] Thus, the color purity can be calculated using the formula (5). The calculated dominant wavelength and color purity are summarized in table 3.1.

$$\text{Color purity} = \frac{\sqrt{(x_s - x_i)^2 + (y_s - y_i)^2}}{\sqrt{(x_d - x_i)^2 + (y_d - y_i)^2}} \times 100\% \quad (5)$$

Figure 3.3 (b) shows the CIE coordinates of the white point $(x_i, y_i) = (0.31271, 0.329202)$ (black hollow circle) and the sample point $(x_s, y_s) = (0.28981, 0.31687)$ (black triangle) corresponding to the white-EL light emitted by our AC-TFEL at the voltage V_3 . The intersection of the dotted line with the locus curve at the point $(x_d, y_d) = (0.06599, 0.21037)$ (blue circle) corresponds to the dominant wavelength of 486 nm. The white-EL light emitted by the AC-TFEL under the lowest rms voltage, $V_1 = 56V$, is shifted 5% from the D65 standard towards the blue, and the shift increases up to 10% as the voltage increases to $V_3 = 77V$. This behavior is consistent with the white-EL normalized spectra in figure 3.4, where the **G** band is enhanced.

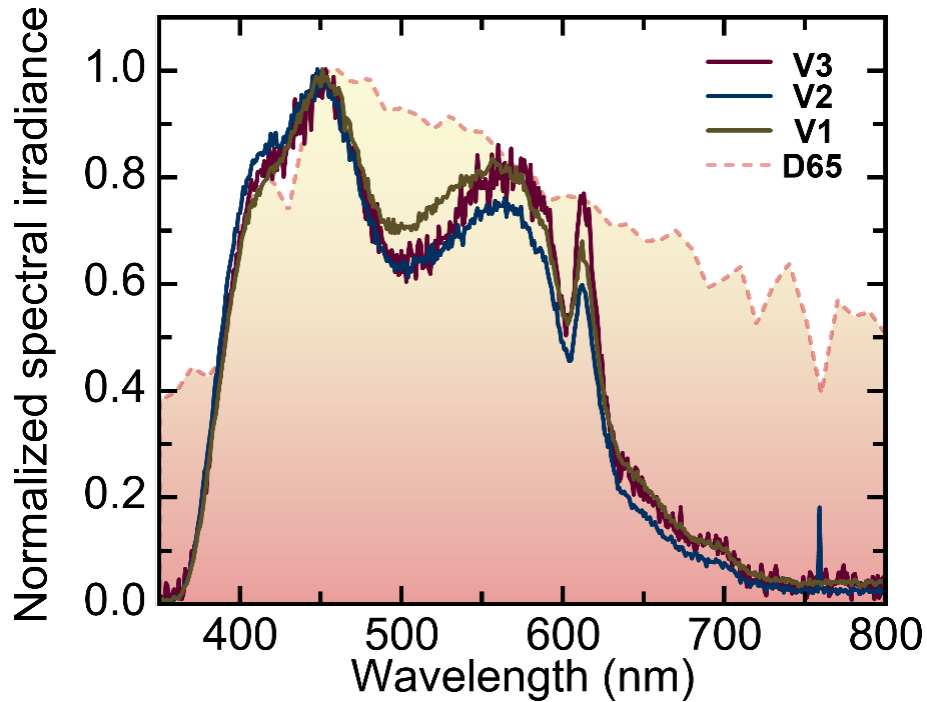


Figure 3.4 Normalized EL spectra of D65 illuminant and the three EL spectra at the corresponding operating rms-voltages of $V_1=56$ V, $V_2=70$ V, and $V_3=77$ V.

Since the luminous efficiency function is given by $y=V(\lambda)$, which describes the average *spectral sensitivity* of human visual perception of brightness, the tristimulus value Y (in equation 2) is directly proportional to the luminous power or flux of the light. Therefore, it provides information about the relative luminance or brightness. table 3.1 depicts the relative luminance Y of the EL device as a function of the three applied rms-voltages. For V_3 , there is a 3% mismatch in terms of the relative luminance. Our findings further corroborate the similarities between our AC-TFEL and the D65 illuminant. In figure 3.4, the normalized EL spectra for the three rms-voltages and the one for the D65 illuminant are shown. The EL are comparable in most of the spectral region from 400 nm to 600 nm. Above 600 nm, red but mainly infrared, is not perceptible for our white-EL device. This is consistent with the resultant blue shift concerning the illuminant, as depicted in table 3.1.

3.3.3 Origin of the white emission

The white-EL of our devices can be explained based on the four mechanisms that occur in this type of AC-TFEL, under the applied electric field, namely (1) tunnel emission (Fowler-Nordheim type) of electrons from interface states at the interface insulator-phosphor, (2) acceleration of electrons to high energy, (3) impact excitation or ionization of the luminescent centers housed in the phosphor, (4) de-excitation of the excited electrons by radiative and non-radiative recombination.^[17,38] With the change in polarity, these mechanisms are alternated from one to the other insulator-phosphor interface. Once the electrons are injected by step 1, they are accelerated under the action of the electric field (E) inside the phosphor which can be calculated in terms of the applied voltage (V) using the formula: $E = \frac{\epsilon_i}{\epsilon_i d_p + 2\epsilon_p d_i} V$ (from ref^[17]), where ϵ_i and ϵ_p are the dielectric constant of the insulating and phosphor layers and d_i and d_p are the thicknesses of the insulating and phosphor layers, respectively. Using the average values $\epsilon_i=21$ for ZrO₂ and $\epsilon_p=5.33$ for ZnS (obtained from references^{[39][40]}) and the thicknesses of the ZrO₂ ($d_i=150$ nm) and ZnS ($d_p=200$ nm) films in the MISIM structure, the resultant electric fields for the three rms applied voltages are $E_1=2.0$ MV/cm, $E_2=2.5$ MV/cm and $E_3=2.75$ MV/cm. If the injected electrons were to accelerate freely under these extremely high electric fields, over a distance x from the interface, they would acquire kinetic energy, $K=Eex$. Under these conditions an accelerated electron, even with the lowest electric field $E_1=2.0$ MV/cm, over a distance $x=15$ nm from the interface, would gain a kinetic energy of $E_1 = 3.0$ eV, which is enough to impact then excite electroluminescent centers with significant impact excitation cross-section in the violet 413 nm (3.0 eV), blue- 450 nm (2.75 eV), green-550 nm (2.25 eV) and red-612 nm (2.03 eV) regions. In the more realistic scenario, where the electrons scatter and lose energy by several high field mechanisms (such as optical and acoustic phonon scattering, impurities scattering, impact ionization, and excitation), there is an electron energy distribution that depends on the applied electric field. This electron energy distribution has been calculated for ZnS using Monte Carlo computer simulations, and the simulated results have shown that at the electric field of 2.0 MV/cm, the percentage of electrons with energies between 2.1 eV and 3.2 eV is approximately 54 %.^[41] Similar results have been found for ZnS using the more simplistic lucky-drift analytical model, which uses the electron mean free path to describe the

high field. Still, this model also shows that the energy relaxation length, or the distance that the electron propagates before it loses a substantial part of its energy, is 32 nm at 2.0 MV/cm. Once the electrons have been accelerated to the threshold energy the impact probability is primarily determined by the impact excitation cross-sections of the specific electroluminescent centers.^[42]

From the above discussion on the electroluminescence mechanisms, it is inferred that the EL emission of our AC-TFEL devices is not only determined by the bulk of the phosphor ZnS:Eu film, but it is also significantly influenced by the chemical and electronic properties of the region of the phosphor and the luminescent centers incorporated close to the ZrO₂-ZnS:Eu interfaces. The ZnS:Eu film used in our devices was deposited under the same conditions used in our previous work for depositing these films on glass substrates;^[32,33] herein, we explain the PL emission band in the blue region as originated from the radiative 4f⁶5d → 4f⁷ transitions of Eu²⁺ ions substituting Zn²⁺ in the hexagonal-wurtzite phase of the ZnS:Eu film. On the other hand, during deposition of the ZnS:Eu film onto the ZrO₂ nano-crystalline film, several chemical processes and homogeneous and heterogeneous reactions can occur. Such as, the leaching of zirconium from the ZrO₂ film might lead to the formation of ZnO sublayers and surface functionalization with ZnS adjacent monolayers. As well as possible incorporation of Eu impurities like Eu³⁺ in the ZnO and ZnS growing layers and on the surface of the ZrO₂ nano-crystalline film.^[43-45] During the deposition of the ZrO₂ onto the ZnS:Eu films, the formation of ZnO sublayers and incorporation of Eu³⁺ on the ZnO surface growing layer and on the surface of the ZrO₂ nanocrystals is also feasible. The shape of the peaks and the prominent edges in the red and green region of the EL spectra (figure 3.2) correspond accordingly to the intra ion ⁵D₀ → ⁷F_J (J=0, 1, 2, 3, 4) 4f-transitions of Eu³⁺ ions incorporated in ZnS, ZnO and ZrO₂ nanocrystals or thin films,^[26,35,46-48] in the region of the ZnS:Eu phosphor film, close to the ZrO₂-ZnS:Eu interface.

It is well known that corresponding ranges of wavelengths of these Eu³⁺ transitions in different compounds are: 570-585 nm (J=0), 585-600 nm (J=1), 610-630 nm (J=2), 640-660 nm (J=3), 680-710 nm (J=4), where the ⁵D₀ → ⁷F₂ transition at 612 nm is dominant. Yet, the intensity and width are dependent on the chemical environment.^[7,49] Since the doping of the ZnO sublayers with Eu³⁺ produces intrinsic defects, such as interstitial zinc and oxygen vacancies,

the broad green-yellow emission centered around 560 nm present in the EL spectra (figure 3.2) can be assigned to radiative transitions between charged oxygen vacancies and the photo-excited holes in the valence band of the ZnO sublayers.^[46] Studies on the electronic interface of ZnO and ZnS submonolayers suggest surface functionalization of these two direct bandgap materials larger than 3.4 eV results in an effective surface band gap narrowing from 3.4 eV until 2.8 eV.^[44] Based on this, we can assume that photons generated from ZnO-ZnS interband transitions could contribute to the prominent edge observed in the UV region of the spectra of the AC-TFEL devices.

3.4 Conclusion

In summary, we have demonstrated white-EL in a MISIM AC-TFEL device fabricated by ultrasonic spray pyrolysis. We used ZnS:Eu as the semiconducting phosphor layer and ZrO₂ as the insulating layers. The device exhibited a white-EL emission with slightly more blue component compared to green and red. The shade of the white light was determined from the CIE chromaticity coordinates, and it resulted close to the illuminant D65. The variation of the applied voltage induces small changes in CIE coordinates. The white-EL emission of these AC-TFEL devices is attributed to the electron-impact excitation and subsequent relaxation of the excited levels of Eu²⁺ and Eu³⁺ impurities, and intrinsic point defect levels in the sublayer regions adjacent to the ZrO₂-ZnS:Eu interfaces.

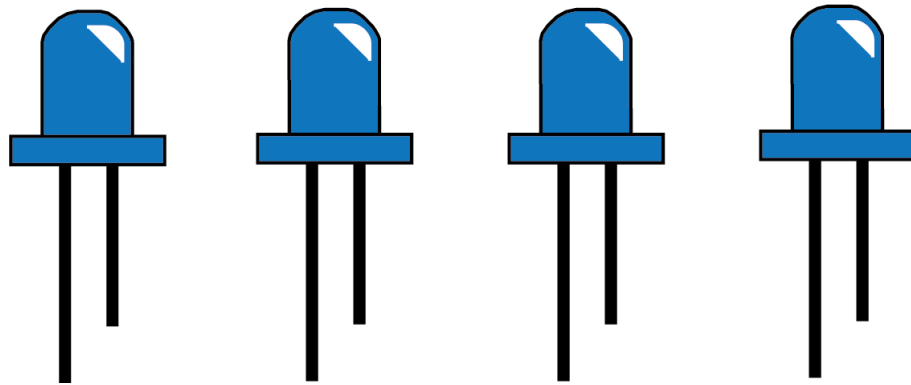
3.5 References

- [1] C. Qi, Y. Zhou, X. Tao, H. Chen, Y. Ouyang, X. Mo, *J. Lumin.* **2020**, *224*, 117230.
- [2] J. Zhang, B. Ren, S. Deng, J. Huang, L. Jiang, D. Zhou, X. Zhang, M. Zhang, R. Chen, F. Yeung, H. Kwok, P. Xu, G. Li, *Adv. Funct. Mater.* **2020**, *30*, 1907074.
- [3] C. Ruan, Y. Zhang, M. Lu, C. Ji, C. Sun, X. Chen, H. Chen, V. L. Colvin, W. W. Yu, *Nanomaterials* **2016**, *6*, 13.
- [4] J. Song, H. Lee, E. G. Jeong, K. C. Choi, S. Yoo, *Adv. Mater.* **2020**, *32*, 1907539.
- [5] M. A. Johar, H. G. Song, A. Waseem, M. A. Hassan, I. V. Bagal, Y. H. Cho, S. W. Ryu, *Appl. Mater. Today* **2020**, *19*, 100541.
- [6] Y. Shirasaki, G. J. Supran, M. G. Bawendi, V. Bulović, *Nat. Photonics* **2013**, *7*, 13.
- [7] J. Rosa, M. J. Heikkilä, M. Sirkiä, S. Merdes, *Materials (Basel)*. **2021**, *14*, 1505.
- [8] J. Zhang, H. Tsai, W. Nie, B. Hu, *Nano Energy* **2021**, *79*, 105413.
- [9] D. Zhao, J. Qian, S. Ye, Y. Li, J. Wang, *Opt. Express* **2020**, *28*, 14176.
- [10] Y. He, M. Zhang, N. Zhang, D. Zhu, C. Huang, L. Kang, X. Zhou, M. Hu, J. Zhang, *Sensors* **2019**, *19*, 4607.
- [11] L. Wang, L. Xiao, H. Gu, H. Sun, *Adv. Opt. Mater.* **2019**, *7*, 1801154.
- [12] J. D. Slinker, J. Rivnay, J. A. Defranco, D. A. Bernards, A. A. Gorodetsky, S. T. Parker, M. P. Cox, R. Rohl, G. G. Malliaras, S. Flores-Torres, H. D. Abruña, *J. Appl. Phys.* **2006**, *99*, 074502.
- [13] J. Junpeng, I. F. Perepichka, J. Bai, D. Hu, X. Xu, M. Liu, T. Wang, C. Zhao, H. Meng, W. Huang, *Nat. Commun.* **2021**, *12*, 54 .
- [14] A. Perumal, M. Fröbel, S. Gorantla, T. Gemming, B. Lüssem, J. Eckert, K. Leo, *Adv. Funct. Mater.* **2012**, *22*, 210.
- [15] C. Tsakonas, S. Wakeham, W. M. Cranton, M. Thwaites, G. Boutaud, C. Farrow, D. C. Koutsogeorgis, R. Ranson, *IEEE J. Electron Devices Soc.* **2016**, *4*, 22.
- [16] M. R. Fernández, E. Z. Casanova, I. G. Alonso, *Sustain.* **2015**, *7*, 10854.
- [17] P. D. Rack, P. H. Holloway, *Mater. Sci. Eng. R Reports* **1998**, *21*, 171.

- [18] Y. A. Ono, *Electroluminescent Displays*, World Scientific Publishing Co. Pte. Ltd., Singapore, **1995**.
- [19] P. F. Smet, I. Moreels, Z. Hens, D. Poelman, *Materials (Basel)*. **2010**, *3*, 2834.
- [20] V. Lahariya, M. Ramrakhiani, *Luminescence* **2020**, *35*, 924.
- [21] C. D. Brubaker, K. N. Newcome, G. K. Jennings, D. E. Adams, *J. Mater. Chem. C* **2019**, *7*, 5573.
- [22] Y. Zuo, X. Shi, X. Zhou, X. Xu, J. Wang, P. Chen, X. Sun, H. Peng, *Adv. Funct. Mater.* **2020**, 2005200.
- [23] E. B. Ramírez, M. Bizarro, J. C. Alonso, *Thin Solid Films* **2013**, *548*, 255.
- [24] D. Li, B. L. Clark, D. A. Keszler, P. Keir, J. F. Wager, *Chem. Mater.* **2000**, *12*, 268.
- [25] M. Aozasa, H. Chen, K. Ando, *Thin Solid Films* **1991**, *199*, 129.
- [26] M. K. Jayaraj, C. P. G. Vallabhan, *J. Electrochem. Soc.* **1991**, *138*, 1512.
- [27] M. Leskelä, M. Mattinen, M. Ritala, *J. Vac. Sci. Technol. B* **2019**, *37*, 030801.
- [28] Q. Z. Gao, J. Mita, T. Tsuruoka, M. Kobayashi, K. Kawamura, *J. Cryst. Growth* **1992**, *117*, 983.
- [29] A. Kitai, Ed., In *Luminescent Materials and Applications*, **2008**, pp. 223–248.
- [30] E. I. Anila, M. K. Jayaraj, *J. Lumin.* **2010**, *130*, 2180.
- [31] K. Ohmi, K. Yamabe, H. Fukada, T. Fujiwara, S. Tanaka, H. Kobayashi, *Appl. Phys. Lett.* **1998**, *73*, 1889.
- [32] M. J. Rivera-Medina, J. Hernández-Torres, J. L. Boldú-Olaizola, J. Barreto-Rentería, J. M. Hernández-Alcántara, V. Jancik, J. C. Alonso-Huitrón, *RSC Adv.* **2016**, *6*, 107613.
- [33] V. H. López-Lugo, M. J. Rivera-Medina, J. C. Alonso-Huitrón, *Mater. Res. Express* **2021**, *8*, 036406.
- [34] J. C. Alonso, F. A. Pulgarín, B. M. Monroy, A. Benami, M. Bizarro, A. Ortiz, *Thin Solid Films* **2010**, *518*, 3891.
- [35] S. J. Yoon, J. W. Pi, K. Park, *Dye. Pigment.* **2018**, *150*, 231.
- [36] A. K. R. Choudhury, In *Principles of Colour and Appearance Measurement*, Woodhead Publishing Limited, Amsterdam, **2014**.

- [37] Y. Shi, Y. Wen, M. Que, G. Zhu, Y. Wang, *Dalt. Trans.* **2014**, 43, 2418.
- [38] W. A. D. M. Jayathilaka, A. Chinnappan, J. N. Tey, J. Wei, S. Ramakrishna, *J. Mater. Chem. C* **2019**, 7, 5553.
- [39] D. Panda, T. Y. Tseng, *Thin Solid Films* **2013**, 531, 1.
- [40] A. Goswami, A. P. Goswami, *Thin Solid Films* **1973**, 16, 175.
- [41] K. Bhattacharyya, S. M. Goodnick, J. F. Wager, *J. Appl. Phys.* **1993**, 73, 3390.
- [42] E. Bringuier, *J. Appl. Phys.* **1991**, 70, 4505.
- [43] F. Forte, L. Yurramendi, J. L. Aldana, B. Onghena, K. Binnemans, *RSC Adv.* **2019**, 9, 1378.
- [44] J. Lahiri, M. Batzill, *J. Phys. Chem. C* **2008**, 112, 4304.
- [45] T. T. Ngoc Van, A. S. Ansari, B. Shong, *J. Vac. Sci. Technol. A* **2019**, 37, 020909.
- [46] H. V. S. Pessoni, L. J. Q. Maia, A. Franco, *Mater. Sci. Semicond. Process.* **2015**, 30, 135.
- [47] Y. P. Du, Y. W. Zhang, L. D. Sun, C. H. Yan, *J. Phys. Chem. C* **2008**, 112, 12234.
- [48] S. Gao, H. Zhang, R. Deng, X. Wang, D. Sun, G. Zheng, *Appl. Phys. Lett.* **2006**, 89, 67.
- [49] K. Binnemans, *Coord. Chem. Rev.* **2015**, 295, 1.

Chapter 4



Metal-halide perovskites as emitters: Bright blue-emitting PeLEDs through the incorporation of small spacer cation

Metal halide perovskites are considered the next generation of light emitters. The ease of tuning their band gap, spanning all the visible spectrum, by changing the halide composition or reducing the size of the crystals through solution-processable techniques makes them the front-runners for displays and large-area illumination technologies.

This chapter reports the fabrication of blue perovskites light-emitting diodes (PeLEDs) using layered perovskites, namely Ruddlesden-Popper (RP). Upon the addition of a small spacer cation as isopropylammonium to $\text{PEA}_2(\text{Cs}_{0.75}\text{MA}_{0.25})\text{Pb}_2\text{Br}_7$, their optical properties are enhanced, resulting in relatively high values of photoluminescence quantum yields (PLQYs) on PEDOT:PSS substrate. Furthermore, transient spectroscopy and grazing-incidence structural techniques unveil that crystallization favors for nominal $n=3$ small crystallites in a random orientation embedded with higher dimensional phases. This was further confirmed through morphological techniques. This behavior helps us to explain why we could fabricate blue-emitting devices without hampering the electrical properties, achieving an EL average of 483 nm with efficiencies up to 6% and color purity up 88%.

This chapter is based on a manuscript in preparation.

4.1 Introduction

Metal halide perovskites are a class of solution-processable semiconductors that have, in the last 10 years, revolutionized the research in optoelectronic devices. While the first achievement has been to reach values of power conversion efficiency values in solar cells close to the one of single crystalline silicon,^[1,2] the interest in their light-emitting properties and their application in electroluminescent devices, have also considerably increased. This interest is propelled by several of the material's physical properties, among them: i) the easy tunability of the emitted color mainly achieved by halide engineering; ii) the possibility for high quantum yield; iii) and good color purity thanks to generally narrow emission spectra; iv) the good transport properties.

In recent years electroluminescence quantum efficiency above 20% has been reported both for the green^[3,4] and infrared,^[5] while the efficiency for sky blue has been lagging behind with values of 12.3%.^[6]

We can distinguish at least three major approaches for the composition of the active layer, namely: i) the 3D perovskite; ii) the two-dimensional and the Ruddlesden-Popper (RP) phases, and iii) the nanocrystal approach. The first approach has the advantage of the good transport properties of the 3D perovskites. However, in bulk materials, the quantum yield of photoluminescence and electroluminescence are often limited, as they are affected by the large trapping non-radiative channels. In contrast, the RP phases have the advantage of tuning the color by changing the dimensionality of the phase. Furthermore, they can reach very high quantum yields due to the recombination in domains experiencing quantum confinement. These advantages come with several challenges: to control the phase distribution and their orientation to favor charge transport (*vide infra*). The last strategy is the one based on perovskite nanocrystal. Due to the confinement of these nanostructures, this approach has similar advantages as the RP phases, even if, in the case of the QDs, the confinement is generally weak, and the color tunability is obtained rather with the variation of the halide, and not varying the dimensionality.^[7] The nanocrystals can achieve quantum yields (QY) higher than 80%^[8] thanks to the passivation of the surface with ligands and the weak confinement. However, the ligands

at the surface are also one of the biggest challenges of this strategy as they are a strong hindrance for charge carrier transport.

In this chapter, we report the fabrication of blue perovskite light-emitting diodes using the RP strategy. To achieve emission in the wavelength range between 480-500 nm, we used the RP system of nominal composition $\text{PEA}_2(\text{Cs}_{0.75}\text{MA}_{0.25})\text{Pb}_2\text{Br}_7$, by using isopropylammonium as an additive, PLQYs as high as 64% were achieved when depositing the material on a PEDOT:PSS coated substrate. Cross-correlation of the optical and structural investigation indicates that the active layer comprises of domains of $n=3$ phases surrounded by higher dimensionality phases, which allow the efficient transport of charge carriers towards the low dimensional domains. Interestingly, the funneling of the photoexcitations towards the low dimensional phases is blocked when the additive is used, which allows obtaining LEDs emitting at an average wavelength of 483 nm, with FWHM of the electroluminescence of 25 nm and an external quantum efficiency up to 6%.

4.2 Experimental section

4.2.1 Chemicals

The methylammonium bromide (MABr), the small cation isopropylammonium bromide (iPAmBr), and PbBr_2 were purchased from Tokyo Chemical Industry (TCI). Phenylethylammonium bromide (PEABr), cesium bromide (CsBr), fused lithium fluoride (LiF), and metal aluminium pieces were purchased from Sigma-Aldrich. The chemicals 2,2',2''-(1,3,5-benzinetriyl)-tris(1-phenyl-1-H-benzimidazole) (TPBi), poly(3,4-ethylenedioxythiophene) polystyrene sulfonate (PEDOT:PSS), toluene, and dimethyl sulfoxide (DMSO) were purchased from Ossila, Heraeus, Acros Organics, and Alfa Aesar, respectively. All chemicals were used as received without any further purification.

4.2.2 Preparation of thin films

All precursor solutions were prepared using 0.5 M of Pb. PbBr_2 , PEABr, MABr, CsBr, and iPAmBr were dissolved in DMSO under continuous stirring for 90 min at room temperature. Solutions were mixed respecting the required final stoichiometry, iPAm was used as an additive and added in 50% molar with respect to the Pb. The solutions were spin-coated on fused quartz or ITO/PEDOT:PSS substrates through a one-step process at 6000 rpm for 60 s. At the 20th second after the beginning of the spin process, 275 μL of toluene was dripped as antisolvent. Subsequently, films were annealed for 10 min at 85°C to ensure the removal of residual solvent.

4.2.3 Optical spectroscopy

The absorbance of the thin films has been measured in a UV-Vis-NIR spectrophotometer (Shimadzu UV-3600) in transmission mode, using an integrating sphere.

Absolute PLQYs were recorded using a Horiba FluoroMax Plus spectrofluorometer coupled through optical fibers to the Quanta-Phi integrated sphere. The excitation source is provided by a monochromatized Xe lamp.

Photoluminescence and time-resolved photoluminescence measurements have been performed in reflection geometry. The third harmonic (267 nm) of the emission from an ultrafast Ti:Sapphire laser (Coherent Mira 900) has been used to excite the samples with an average power of 50 μW . A 150 mm focal lens was used to focus the laser beam on the sample while the photoluminescence was collected through an achromatic doublet to a combined spectrograph, consisting of a monochromator with a 1200 1/mm grating and two detectors; one for steady-state and the second for time-resolved PL. Scattered light from the excitation beam was filtered with a 305 nm long-pass filter. Steady-state spectra were acquired with a spectral-calibrated EM-CCD camera (Hamamatsu C9100-13). Time-resolved PL was taken using a picosecond streak camera (Hamamatsu C5680-24) working in synchroscan mode, in a time range of 2 ns. Under the experimental conditions used for these measurements, a time resolution of 10 ps has been evaluated. For the PL measurements, samples were transferred from a glove box to

a sample holder without exposing them to air and then kept in a vacuum during the measurements.

Fast transient absorption spectroscopy has been performed at “Università di Cagliari” by prof. Andrea Mura. Samples for the measurements have been encapsulated by quartz glass and sealed with epoxy adhesive before shipping them. The measurements have been performed in a pump-probe configuration. The output of a regenerative amplifier (794 nm, 4 mJ, 1 kHz) with an integrated Ti:Sapphire oscillator (Coherent Libra) was used to seed an optical parametric amplifier (Light Conversion Topas 800) to generate the 100 fs long pulses at 360 nm used as a pump. The probe was a white light supercontinuum (390-850 nm), generated inside a transient absorption spectrometer (Ultrafast Systems Helios) by focusing a small part of the regenerative amplifier output into a rotating CaF₂ crystal. The pump was focused on the sample with a spot size of 150 μm , and the fluence was adjusted to 3 nJ for all the measurements. Two custom CMOS spectrometers individually acquired the probe transmitted through the sample and a reference spectrum to compensate for white-light oscillations. A chopper on the optical path of the pump allowed recording of the sample absorption with and without pump excitation. In the time, the pump-probe time delay was controlled, modifying the optical path of the probe through a delay line. Time delays as high as 8 ns have been probed.

4.2.4 Structural measurements

X-ray diffraction patterns were recorded by a Bruker D8 Advance Diffractometer using Cu K α source ($\lambda = 1.54 \text{ \AA}$) and a LynxEye detector. Grazing incidence wide-angle X-ray scattering (GIWAXS) measurements on perovskite thin films using a MINA X-ray scattering instrument built on a Cu rotating anode source ($\lambda = 1.5413 \text{ \AA}$) following the procedure reported in our previous work.^[9] SEM images were recorded on an FEI NovaNano SEM 650 microscope through a CBS detector and with an acceleration voltage of 18kV. AFM micrographs were recorded by ScanAsyst mode using a Bruker Dimension Icon microscope and analyzed through Gwyddion software.

4.2.5 Fabrication of the PeLEDs

Our PeLEDs were fabricated using ITO patterned substrates with four different active areas of 0.1, 0.16, 0.36, and 1.0 cm². These substrates were ultrasonically cleaned using a hot soapy solution, rinsed with DI water, acetone, and isopropanol. A 35 nm PEDOT:PSS film was achieved by a two-step spin coating process followed by an annealing process at 140 °C in air for 20 min. During the first spin-step process, PEDOT:PSS solution was dripped carefully to fully cover the substrate at 500 rpm for 5 s. Sequentially, the second step began at 3000 rpm for 60 s. Next, the perovskite active layer was deposited on top of the PEDOT:PSS film in a N₂ glovebox following the process described above. Finally, TPBi and LiF/AL electrodes were thermally evaporated in vacuum with pressure as low as 10⁻⁸ mbar through a patterned shadow mask to determine the active areas as the ITO and AL overlapping section electrode. For this investigation, more than 60 PeLEDs were fabricated and characterized.

4.2.6 Characterization of the PeLEDs

Our PeLEDs were characterized through a calibrated integrated sphere with barium sulfate coating from Newport. A 2400 Keithley power source supplied the applied bias. The EL spectra were recorded through an Ocean Optics spectrometer (USB2000) coupled to the optical fiber (QP400-2-UV-Vis), and the radiant flux was collected by a silicon photodiode (Hamamatsu S2281-01). In addition, a 6514 Keithley electrometer registered the generated photocurrent. Both the detectors were residing on the wall of the integrated sphere at about 90° from the light source. The colorimetric characteristics were calculated through a designed Python program when feeding our EL spectra.

4.3 Results and discussion

4.3.1 Perovskite active layer and their physical properties

Figure 4.1 shows the schematics of the Ruddlesden-Popper (RP) $n=2$ phases used in this study. On the left of the figure, the system of composition $\text{PEA}_2(\text{Cs}_{0.75}\text{MA}_{0.25})\text{Pb}_2\text{Br}_7$ to which in the following we will refer as *neat*, and on the right, the system obtained with the addition of isopropylammonium, to which we will refer as *iPAm-modified*. Thin films of the two systems including other control samples, as the pure 2D system ($\text{PEA}_2\text{PbBr}_4$) and the 3D perovskite ($\text{Cs}_{0.75}\text{MA}_{0.25}\text{PbBr}_3$), were deposited by spin-casting from DMSO solution using toluene as antisolvent (we refer to the experimental section for more details).

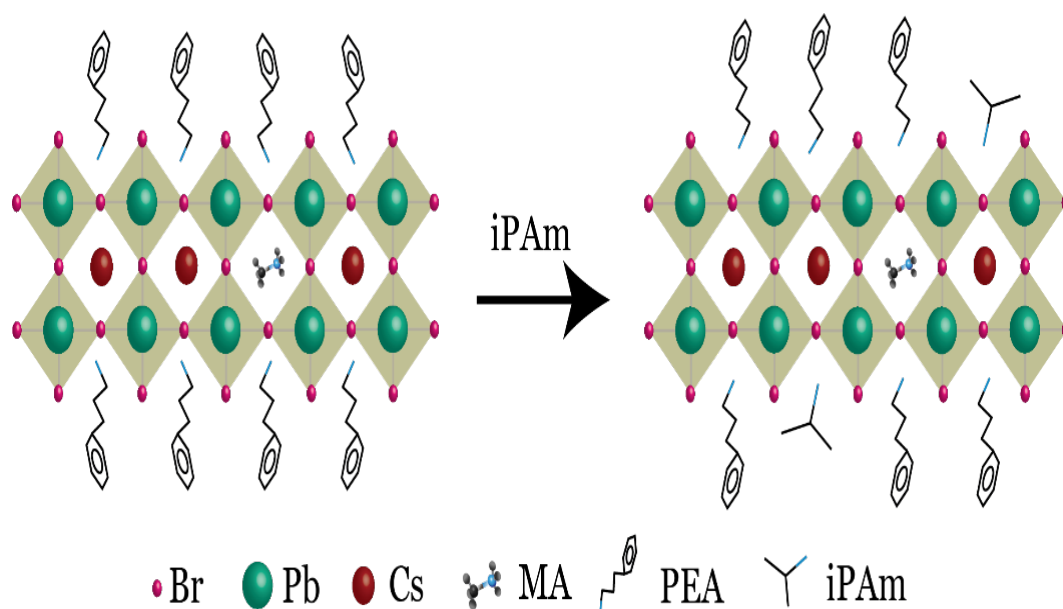


Figure 4.1 Schematic illustration of $\langle n=2 \rangle$ perovskite used as the active layer of the blue PeLED. On the left side is depicted the composition $\text{PEA}_2(\text{Cs}_{0.75}\text{MA}_{0.25})\text{Pb}_2\text{Br}_7$ [*neat*] and on the right side the composition $\text{PEA}_2(\text{Cs}_{0.75}\text{MA}_{0.25})\text{Pb}_2\text{Br}_7:\text{iPAm}$ obtained using isopropylammonium [*iPAm*] as an additive.

Figure 4.2 (a) reports the absorbance and the photoluminescence (PL) spectra of the 2D, the $\langle n \rangle = 2$, $\langle n \rangle = 3$ RP phases, and the 3D perovskite deposited on quartz substrates. The spectra of the 2D sample ($n=1$) with an absorption peak at 403 nm and an emission peak at 410 nm, are dominated by the excitonic behavior determined by dielectric and quantum confinement of carriers into the inorganic layers. The $\langle n \rangle = 2$ thin film shows absorbance and PL spectra indicating the presence of multiple phases. Additional to the $n=1$, the $n=2$ phase with an absorption peak at 433 nm and emission at 441 nm, and the $n=3$ phase with absorbance at 464 nm and emission at 475 nm are also visible in the spectra. Furthermore, the absorbance shows a low energy tail that is surely composed of a small amount of material of rather large n values (quasi-3D) as the PL spectra are prevailed by emission at 512 nm (note that the 3D absorbance is at about 520 nm and the emission of the 3D phase is at 530 nm). The strong $n=2$ absorbance and PL dominated by quasi-3D phases is a clear indication of an effective energy transfer mechanism in this sample. The optical properties of the $\langle n \rangle = 3$ sample are substantially very similar to the $\langle n \rangle = 2$ with the notorious presence of the quasi-3D phase in the absorbance spectra with a peak located around 516 nm, and the PL spectra govern by a broad emission also attributed to the quasi-3D phase. Figure 4.2 (b) reports the absorbance and the PL spectra of the same types of samples as in figure 4.2 (a), in which iPAm has been added to the precursor solution as an additive. Interestingly, while the addition of iPAm does not seem to have an influence on the optical properties of the 2D sample and only determines a small blue shift (5 nm) of both the absorption and emission peak in the 3D phase, it has a rather dramatic effect on the RP phases $\langle n \rangle = 2$ and $\langle n \rangle = 3$, with the almost total suppression of the larger n contributions. The PL of these two samples is now dominated by the high energy peaks corresponding to $n=1$, $n=2$ and $n=3$ emissions.

As our aim is to fabricate blue light-emitting diodes in the following, we concentrate on the samples with $\langle n \rangle = 2$ compositions. One of the most common hole transport layers (HTL) in perovskite light-emitting diodes is the conductive polymer PEDOT:PSS.^[10] As the energy landscape of RP phases is susceptible to many processing factors and to the surface where they are deposited,^[11,12] it is imperative to investigate the physical and structural properties of our samples when deposited on PEDOT:PSS.

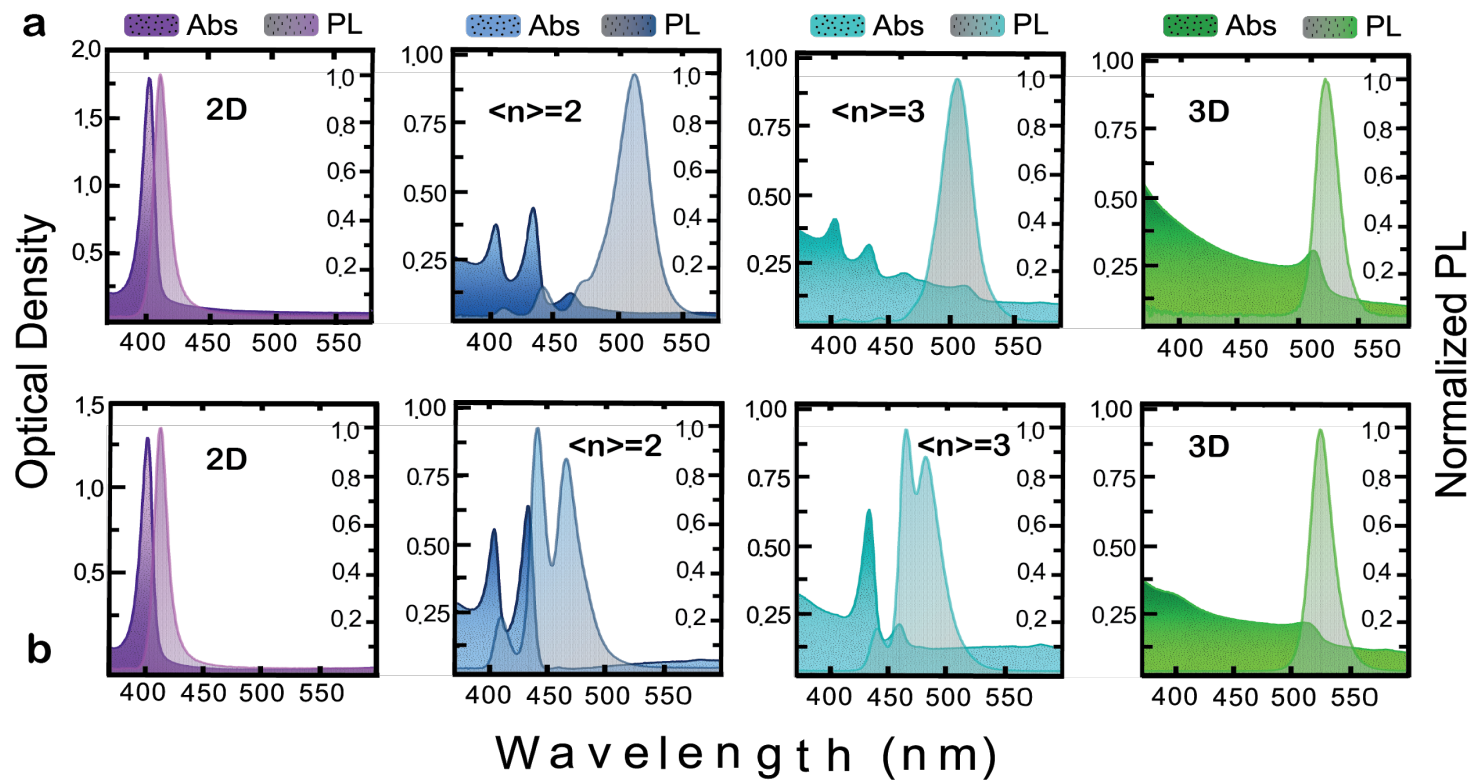


Figure 4.2 Steady-state optical characteristics of 3D ($\text{Cs}_{0.75}\text{MA}_{0.25}\text{PbBr}_3$), 2D ($\text{PEA}_2\text{PbBr}_4$), and quasi-2D perovskites deposited on quartz substrates. Absorbance (Abs) and photoluminescence (PL) spectra of thin films of different nominal $\langle n \rangle$ value for neat (a) and iPA-modified (b) perovskites.

Figure 4.3 shows the results of PL measurements on nominal $\langle n=2 \rangle$ thin films, neat and iPAm-modified, deposited on quartz and ITO/PEDOT:PSS substrates. By fitting the spectra, a total of five components have been identified in the emission of the RP films, which can be attributed to different n -phases, from 1 to ≥ 5 . In table 4.1, the corresponding emission peak wavelengths are reported, together with the values of their FWHM. No significant shift in the emissions is observed between different samples.

As seen previously, for the neat films [figure 4.3 (a)], the PL spectrum is governed by an emission at 510 nm, attributed to $n \geq 5$ phases. On both substrates, the spectra seem similar, although the emission peaks are represented with different intensities. For the film on PEDOT:PSS, the emission from low n -value phases is more intense concerning the main peak.

With the addition of iPAm [figure 4.3 (b)], the $n \geq 5$ phase emission is completely suppressed in the case of the quartz substrate, whereas for the film on PEDOT:PSS is present as one of the strongest emissions. The 475 nm, which corresponds to the $n=3$ phase, is the most intense on the quartz substrate, whereas for the PEDOT:PSS film, the 491 nm ($n=4$ phase) appears as dominant. As for the neat perovskite and the iPAm-modified samples, the deposition on PEDOT:PSS increases the relative intensity of the emission from low n -value phases, particularly from the $n=1$.

A comparison of the PL spectra of neat and iPAm-modified perovskites, both on PEDOT:PSS [(figure 4.3 (c)], reveals as an effect of the additive an enhancement in the emission of $n=2$ and $n=3$ phases. In contrast, the emission of the $n=1$ phase is diminished (see table 4.1). Most importantly, the PL quantum yield (QY) of films deposited on PEDOT:PSS [figure 4.3 (d)] is 2-fold for the iPAm-modified film with respect to the one of the neat films; a value as high as 64% was measured for the iPAm-modified sample. It is interesting to note that the QY of samples deposited on quartz does not overcome values of 7.2%.

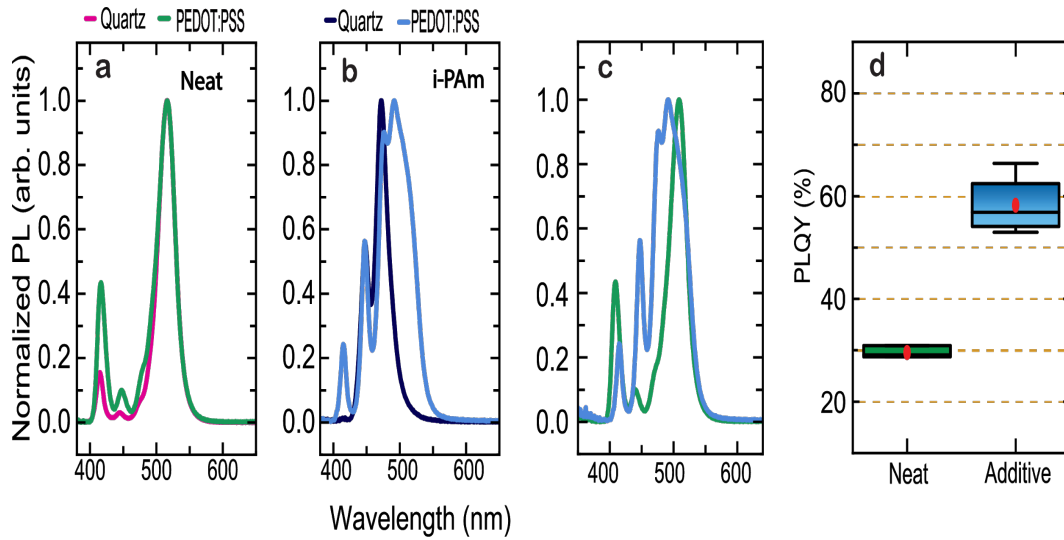


Figure 4.3 Photoluminescence characteristics of $\langle n=2 \rangle$ thin films deposited on quartz and PEDOT:PSS. (a) PL spectra of the $\langle n=2 \rangle$ [neat] films, and of (b) of iPAm-modified ones. (c) influence of PEDOT:PSS on neat (green color) and iPAm-modified films (blue color), and (d) PLQYs for the two samples on PEDOT:PSS.

Table 4.1 Photoluminescence peaks. Peak position and FWHM of the main emission signals in the steady state PL spectra reported in Figure 4.3. The values are obtained fitting the spectra with multiple gaussians components.

N phase	Peak position (nm)	FWHM
N=1	415	9
N=2	448	14
N=3	475	15
N=4	491	16
$N \geq 5$	510	30

4.3.2 Charge carrier dynamics

Figure 4.4 shows the results of time-resolved PL (TRPL) measurements on films of neat (left panels) and iPAm-modified perovskites (right panels) deposited on top of PEDOT:PSS. The time-resolved spectra of the neat film [figure 4.4 (a)] present the same features observed in steady-state PL. In addition, we observe that right after the excitation, the spectrum shows two high-intensity emissions from $n=1$ and $n=2$ phases, together with a broad emission peaked at 510 nm, which is given by the overlap of the emission from $n=3$, $n=4$, and $n\geq 5$ phases. By comparing the spectra at different time intervals after the excitation, the peaks from low n -value phases undergo a rapid decay, almost completely disappearing in the time scale of a few nanoseconds. In contrast, the broad emission peaked at 510 nm decays much slower. Nevertheless, it is still strong after more than 13 ns; namely, it is longer than the temporal difference between two consecutive pulses of our laser (repetition rate 76 MHz). Moreover, the broad emission appears to get narrower with time, with faster decay of the emission on the side of low wavelengths. We can then deduce the emission from $n=1$ and $n=2$ phases, plus the one from $n=3$ and $n=4$ have much rapid decay compared to the ones from the $n\geq 5$ phase. In figure 4.4 (c), the decays of the PL signal are reported at wavelengths corresponding to the peak positions extracted from the steady state (see table 4.1).

The decay dynamics were fitted using a multi-exponential function and the PL lifetimes obtained are reported in table 4.2. The lifetimes increase with the increase of the n -value, both in the time range of tens and hundreds of picoseconds. Additionally, the $n\geq 5$ phase emission is not only characterized by the slowest decay, but the calculated lifetimes are almost two-fold those of the emissions of the other n -value phases. The results suggest the presence, in the neat perovskite film, of efficient energy funneling from the phases with larger to phases with narrower band gap (i.e. from lower to higher n -value), which ends with the radiative recombination of the carriers in the $n\geq 5$ phase.

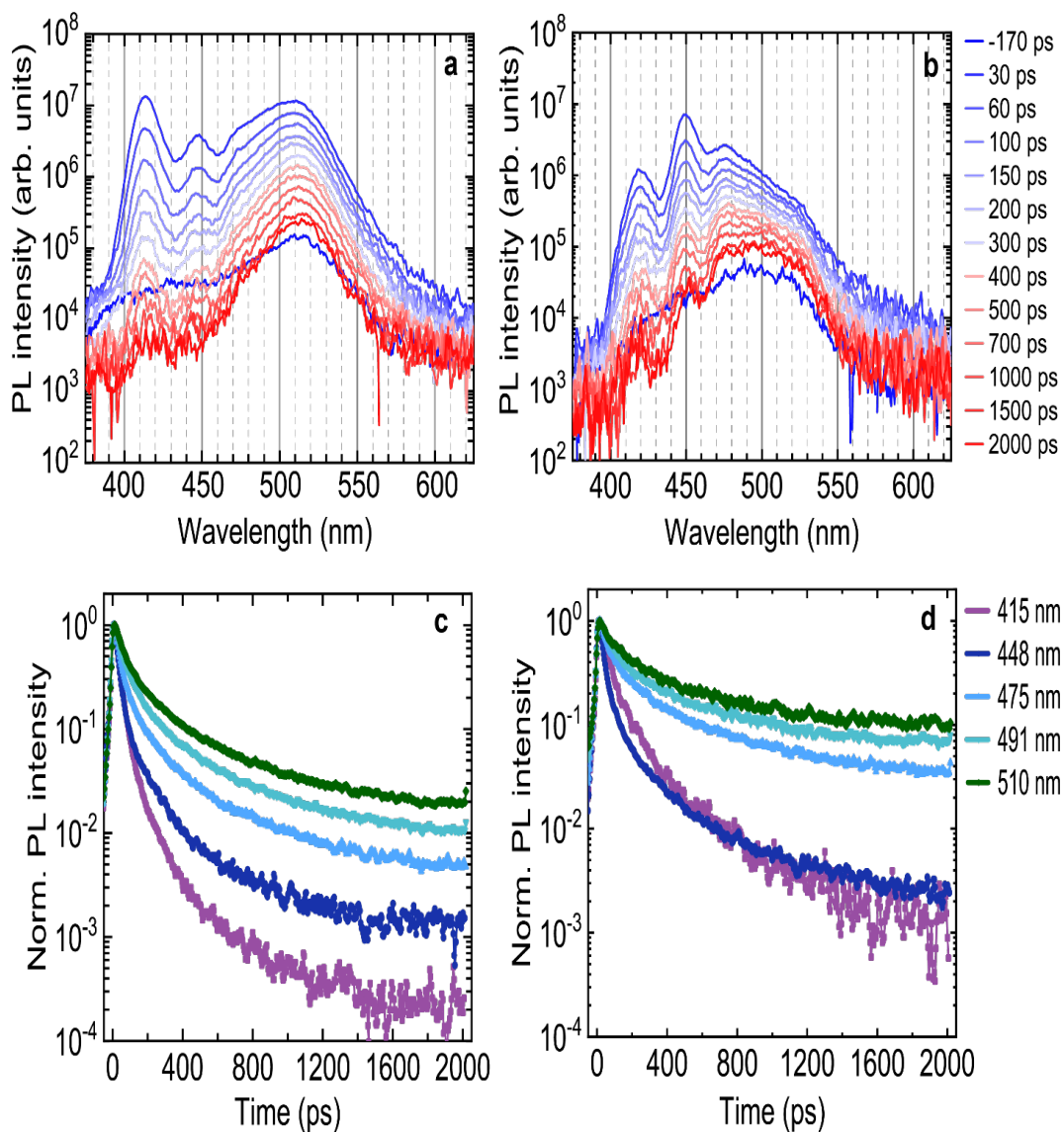


Figure 4.4 Time-resolved photoluminescence (TRPL) of $\langle n=2 \rangle$ thin films deposited on PEDOT:PSS. PL spectra at different times after excitation of (a) neat film and (b) films with the addition of iPA. PL decays measured at different wavelengths, corresponding to the emission of different N-phases, in (c) neat film and (d) film with the addition of iPA.

Table 4.2 PL lifetimes obtained by fitting with a multi-exponential decay function the time-resolved PL signal at different wavelengths for both neat and iPAm-modified films. For the film with the additive signals at 475, 491 and 510 nm show a long tail with a decay much longer than the time range of the measurements.

	Wavelength (nm)	τ_1 (ps)	τ_2 (ps)	τ_3 (ps)
Neat	415	26	77	264
	448	22	96	315
	475	25	98	381
	491	29	92	380
	510	44	160	521
iPAm-modified	415	39	125	484
	448	24	99	370
	475	49	329	/
	491	68	418	/
	510	71	401	/

Similarly, as discussed above, for the neat perovskite samples, the time-resolved spectra, for the iPAm-modified samples [(Figure 4.4 (b))], resembles its steady-state PL. However, by paying careful attention to the time evolution of the spectrum, we can notice some differences to the neat film. While an initial rapid decay still characterizes the emissions from $n=1$ and $n=2$ phases, they remain distinctly visible in the spectrum up to 2 ns. The steady-state PL broad band that includes the emission from $n=3$, $n=4$, and $n \geq 5$ phases, at short times after the excitation, appears peaked at 475 nm, showing the dominant contribution of the $n=3$ phase. After more than 13 ns (see the dark blue spectrum), the profile still shows components at high energy as if the energy funneling is partially hindered. This is remarkably distinct behavior as observed in the neat film.

Driving our attention to figure 4.4 (d) of the decay dynamics, an increase in PL lifetimes appears evident for the emission from all the n -value phases when iPAm is added to the

perovskite (see for the lifetimes in table 4.2). As mentioned in the analysis of the time-resolved spectra, the emission from $n=1$ and $n=2$ phases have decayed in the first tens of picoseconds, similar to that observed in the neat film. However, for the neat film, the emission results completely depleted in hundreds of picoseconds; whereas, in the iPAm-modified film, a significant part of the emission occurs in a nanosecond timescale. The differences between neat and iPAm-modified film are even more important for the emission from $n=3$, $n=4$, and $n\geq 5$ phases. These emissions became significantly longer by the additive, with lifetimes of tens or even hundreds of nanoseconds. Furthermore, for $n=3$ and $n=4$ phases, longer τ_1 lifetimes suggest hindering of the energy transfer mechanism to the $n\geq 5$ phase. In short, the analysis of the time-resolved PL points out that the addition of iPAm to the perovskite brings to a significant increase in the PL lifetimes of all the n -value phases in the film, pointing to a reduction of the energy funneling and of the non-radiative component. The last is in a good agreement with the very high quantum efficiency of the iPAm-modified films.

To better understand the effects of iPAm on the photophysics of the material, fast transient absorption spectroscopy measurements (FTAS) have been carried out on neat and iPAm-modified films. Such spectroscopic technique, in fact, allows investigating charge carrier dynamics in the firsts hundreds of femtoseconds after excitation, which is the typical timescale of charge and energy transfer mechanisms in solid materials.

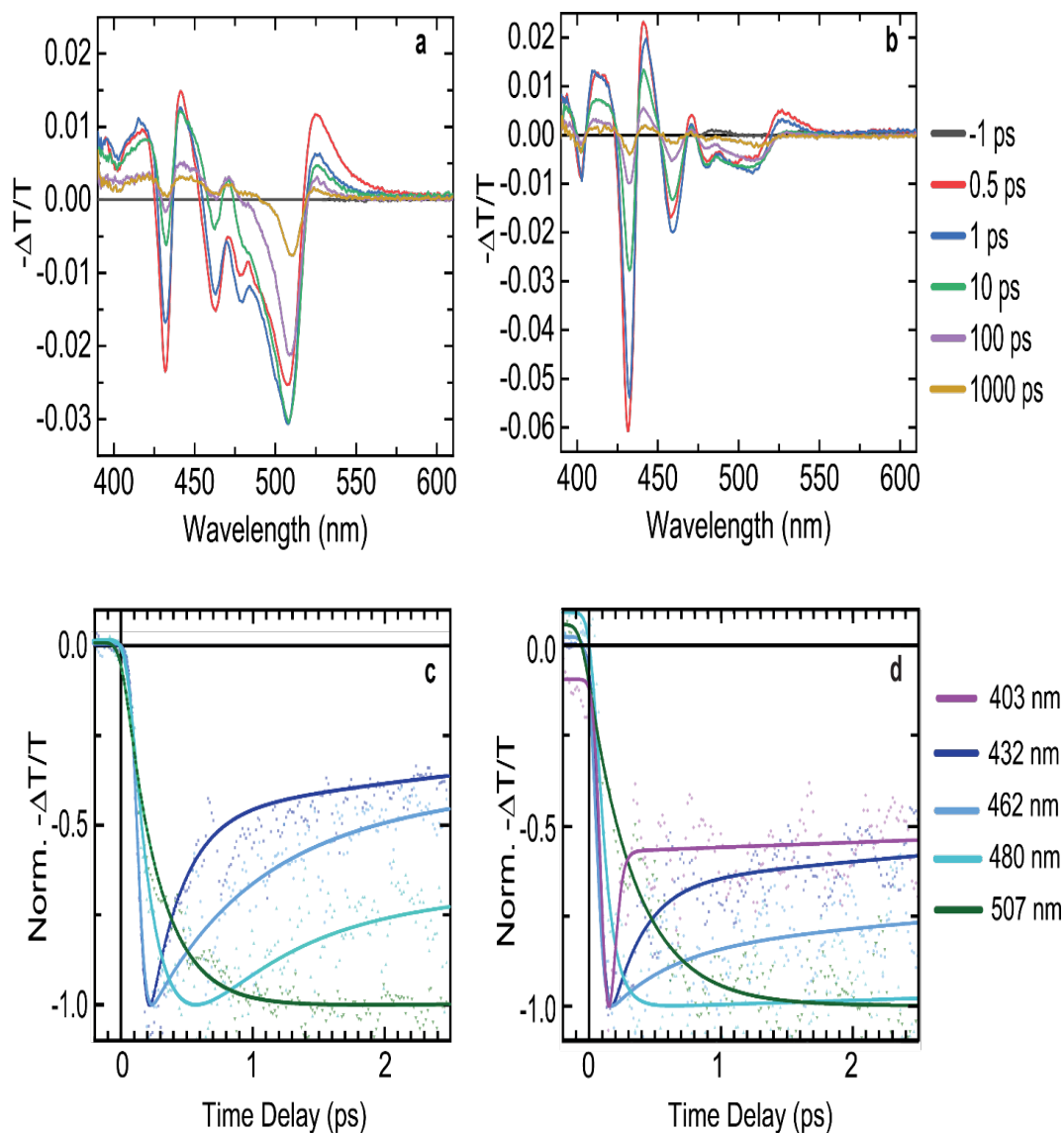


Figure 4.5 Fast transient absorption spectroscopy (FTAS) characterization of $\langle n=2 \rangle$ thin films deposited on PEDOT:PSS. Transient spectra at different delay times between pump and probe for (a) neat film and (b) film with the addition of iPA. Time dependence of the normalized FTAS signal at different wavelengths, corresponding to the main absorption bleaching features on the spectra, for (c) neat film and (d) film with the addition of iPA: experimental data (colored dots) and best fitting models (colored lines).

Table 4.3 FTAS fit results. Time constants obtained by fitting the dynamics of the main absorption bleaching features on the transient absorption spectra of both neat and iPAm-modified films. Signals fitted by a combination of exponential rising (τ_R) and decays (τ_1 , τ_2 and τ_3). Errors are evaluated considering the instrument response function of the experimental setup and the parameters used for the measurements.

	wavelength (nm)	τ_R (ps)	τ_1 (ps)	τ_2 (ps)	τ_3 (ps)
Neat	403	/	/	/	/
	432	/	0.2 ± 0.1	15 ± 2	/
	462	/	0.8 ± 0.1	14 ± 2	158 ± 2
	480	0.2 ± 0.1	0.7 ± 0.1	24 ± 2	128 ± 2
	507	0.3 ± 0.1	/	116 ± 2	680 ± 30
iPAm- modified	403	/	<0.1	41 ± 2	/
	432	/	0.2 ± 0.1	26 ± 2	730 ± 30
	462	/	0.5 ± 0.1	25 ± 2	620 ± 30
	480	0.1 ± 0.1	/	36 ± 2	640 ± 30
	507	0.4 ± 0.1	/	202 ± 2	1490 ± 30

Figure 4.5 depicts the result of the FTAS measurements for neat (left panels) and iPAm-modified film (right panels). As already done previously, we first focus on the neat film. The transient spectra of the neat film [Figure 4.5 (a)] show in the range of wavelengths between 400 and 550 nm several photobleaching features, following the pump excitation. Such features arise from the depopulation of the ground state caused by the absorption of the pump pulse. The photobleaching features on the spectra match well the absorption peaks observed in the steady-state in figure 4.2; thus, they can be correlated with the different n -value phases present in the film. A positive broadband signal, which corresponds to an increase in the absorption, namely a photoinduced absorption, is also overlapped to the photobleaching, making them not easy to observe at long time delays. Nonetheless, the transient spectra evidence a rapid decay dynamic for the photobleaching associated with $n=1$, $n=2$, $n=3$ and $n=4$ phases (signals at 403, 432, 462,

and 480 nm, respectively), whereas the signal correlated with $n \geq 5$ (507 nm) has a much longer lifetime, in perfect agreement with the TRPL results.

The decay dynamics of the photobleaching up to 8 ns can be fitted by a multi-exponential function. The results of the fits are reported in figure 4.5 (c) (close up on the first 2.5 ps) and in table 4.3. Unfortunately, due to its extremely fast decay and to the presence of a much stronger photoinduced absorption signal overlapped to it, it is not possible to fit the photobleaching of the absorption of $n=1$ phase (403 nm). Photobleaching related to the $n=2$ and $n=3$ phases (432 and 462 nm, respectively) has similar dynamics. An initial fast decay which halves the intensity of the signals in the time scale of hundreds of femtoseconds. Following that, the decay dynamics are comparable with the dynamics observed in TRPL, suggesting a carrier relaxation through radiative recombination. Also, the decay dynamics are analogous for the photobleaching related to the $n=4$ phase, except for two noteworthy differences. First, the signal does not have a sharp rising as the previous ones and it reaches its maximum in a time of hundreds of femtoseconds, which well matches the initial fast decay of the other two signals. Second, although this signal has an initial fast decay as the others, the decrease of intensity in the firsts picoseconds is minor. Most of the signal decays in tens of picoseconds. Focusing on the photobleaching associated with $n \geq 5$ phases, we observe an even longer rising of the signal followed by decay dynamics of nanoseconds. To summarize, the FTAS measurements on the neat perovskite film not only confirm the results of the TRPL but, by showing ultrafast decays for the signals related with low n -value and rising in the signals associated with high n -value phases, demonstrate beyond doubt the presence of efficient energy funneling in the system.

Following the same approach for the iPAm-modified film, we observe the same photobleaching features characterize the transient spectra in figure 4.5 (b) as for the neat film. Nonetheless, the photobleaching signals related to low n -value phases are higher in intensity, and their decay is significantly slower than in the neat film. The higher intensity can suggest a larger amount of the related phases in the sample or, more likely, a hindering of ultrafast decay processes, comparable or even shorter than the time resolution of the measurement (100 fs). The fit of the dynamics of the signals [figure 4.5 (d) and table 4.3] clearly shows the iPAm addition effects. Thus, while the initial fast decay of the signals associated with $n=1$, $n=2$, and $n=3$ phases

is still present, its effect on the intensity of the signals is largely reduced. Most of the photobleaching signal decays in a time range of a few nanoseconds, compatible with the radiative recombination for all these phases. The effects of the additive are even more remarkable on the signal related to the $n=4$ phase for which, after the rising, we do not observe any more a fast decay, as if the energy funneling to higher n -value phases is completely hindered. Lastly, the photobleaching associated with the $n \geq 5$ phases is still characterized by a pronounced rising, followed by prolonged decay, even longer than in the neat film and longer than the probed time range (8 ns).

Summarizing, the results of the FTAS measurements on the iPAm-modified perovskite film further prove a substantial hindering of the energy funneling and thus a higher chance to have radiative recombination of the excitons in the phase where they are generated. This is expected to enhance quantum yield and the color purity of the emission in light-emitting devices.

4.3.3 Structural and morphological characterizations

The next step is to understand the thin film quality and their crystallographic structure to comprehend if they are suitable for fabricating light-emitting diodes. The possibility to fabricate a light-emitting diode with the investigated samples is based on the ability to fabricate smooth and continuous thin films, as the overall device structure requires the possibility to deposit on top of the active layer other functional layers and the cathode without creating electrical shorts. Figure 4.6 shows the scanning electron microscope (SEM) and atomic force microscopy (AFM) micrographs of the neat and iPAm-modified samples. The neat sample displays, when measured with both techniques, a wrinkled structure. These types of structures are often obtained when using the antisolvent method and recently were explained as formed via a bilayer intermediate with a perovskite top layer on a viscous amorphous bottom layer.^[12] The iPAm-modified film does not show wrinkles but a rather smooth surface composed by relatively small and randomly oriented flat crystallites.

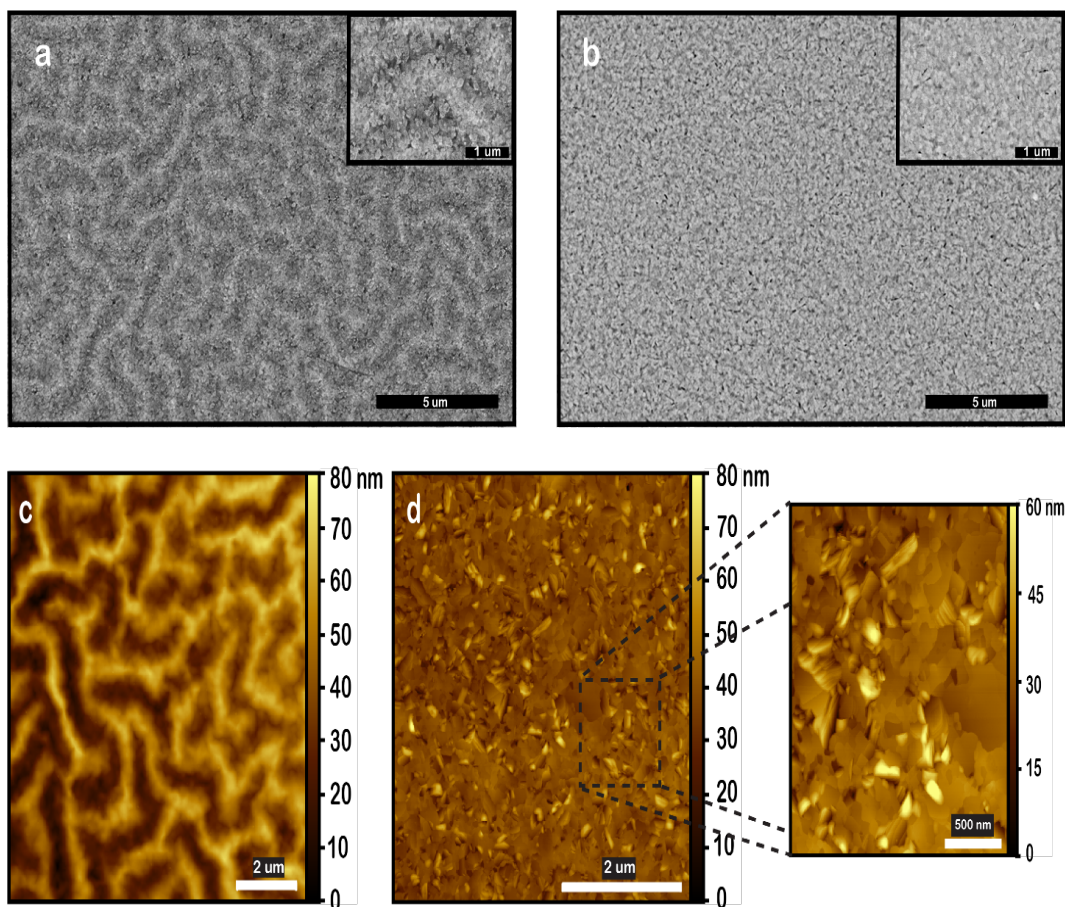


Figure 4.6. SEM and AFM micrographs of nominal $\langle n=2 \rangle$ samples. SEM micrographs of the (a) neat perovskite and (b) iPAm-modified films. The insets show magnification of the surface morphology. AFM micrograph of (c) neat film (scan size of $10 \mu\text{m} \times 10 \mu\text{m}$) and (d) iPAm-modified film (scan size of $5 \mu\text{m} \times 5 \mu\text{m}$). On the right-side of (d) is shown a zoom-in of the iPAm film (size $2 \mu\text{m} \times 2 \mu\text{m}$).

Figure 4.7 exhibits powder-XRD measurements carried out for nominal $\langle n=2 \rangle$ thin films and 2D as control film after adding the small spacer cation of iPAm for both quartz and PEDOT:PSS substrates. In general, no significant perturbation is observed for the 2D control-perovskite thin films after the addition of iPAm on both substrates. However, the perovskite crystallization appears to be influenced by the substrate. Two reflection peaks located at $2\theta=30.5^\circ$ and $2\theta=35.6^\circ$ appear only when films are grown on PEDOT:PSS. In nominal $\langle n=2 \rangle$ RP phases films, a combination of 2D and 3D phases coexist, with a dominance of the 2D, especially on quartz after incorporating iPAm, as shown in figure 4.7(b).

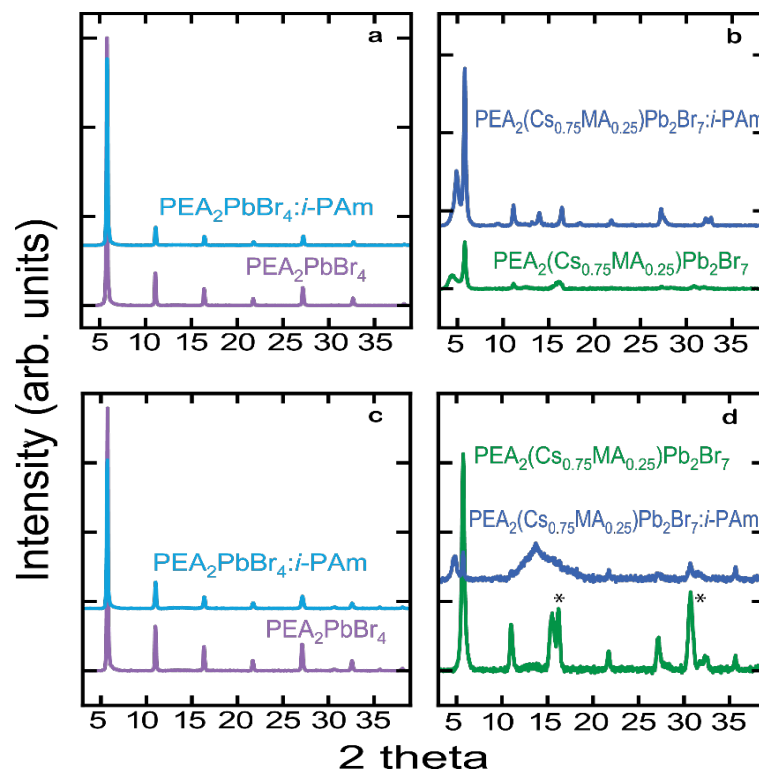


Figure 4.7 Powder X-ray diffraction patterns (XRD) of 2D and nominal $\langle n=2 \rangle$ layered perovskite thin films for neat and iPAm films. (a, b) Films deposited on quartz (c,d) and on PEDOT:PSS.

A particular situation occurs when the nominal $\langle n=2 \rangle$ films are crystallized on PEDOT:PSS. The mixture of 2D and 3D prevails for neat films, and both phases seem to be enhanced. The peaks, marked with a star on figure 4.7(d), located at $2\theta=16.20^\circ$ and 30.7° correspond to the 3D perovskite counterparts^[3]; the latter is also present in the iPAm-modified film, whereas the former is not observable. The iPAm-modified film shows very low crystallinity, with the emergence of broad features and remaining diffraction peaks typical of the 2D phase, including the low reflection peak at $2\theta < 5^\circ$.

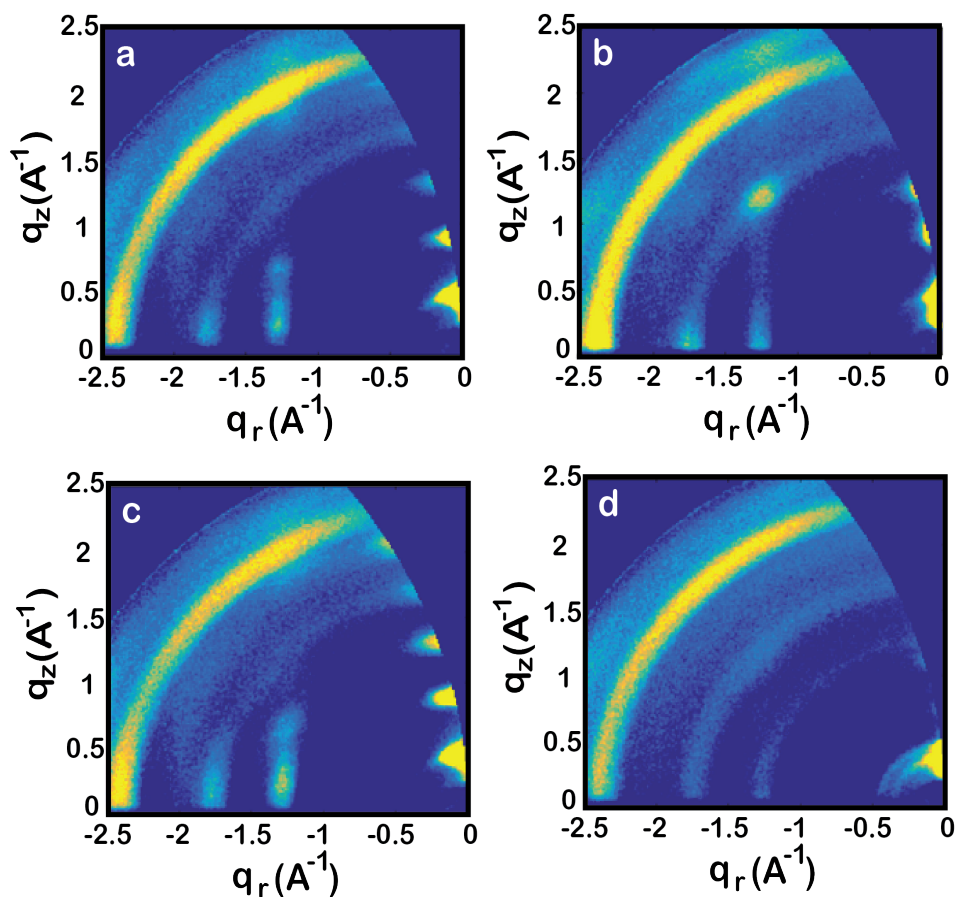


Figure 4.8. GIWAXS patterns of thin films of (a) $\text{PEA}_2\text{PbBr}_4$, (b) $\text{PEA}_2(\text{Cs}_{0.75}\text{MA}_{0.25})\text{Pb}_2\text{Br}_7$, (c) $\text{PEA}_2\text{PbBr}_4$:i-PAm and (d) $\text{PEA}_2(\text{Cs}_{0.75}\text{MA}_{0.25})\text{Pb}_2\text{Br}_7$:iPAm deposited on PEDOT:PSS.

The structure of the perovskite thin films deposited on PEDOT:PSS without and with the addition of the additive was further investigated by GIWAXS (see figure 4.8). GIWAXS patterns allow obtaining information about the packing adopted by the material and the preferred orientation of the perovskite crystallites.^[11,13,14] The GIWAXS pattern of the pristine 2D $\text{PEA}_2\text{PbBr}_4$ thin film can be described assuming a unit cell with a, b, and c axis of about 12 x 12.5 x 17.5 Å in agreement with XRD results and the reported crystal structure for $\text{PEA}_2\text{PbBr}_4$.^[15] The 00l peaks are highly aligned along the quasi vertical z-direction [see figure 4.7 (a)], indicating that the 2D crystallites align with the 00l planes parallel to the substrate, in agreement with what is commonly reported for other 2D Pb- and Sn-based perovskites using PEA cations. The films show a high degree of order as up to 5 00l reflections are visible along

the z-direction. The addition of iPAm to the $\text{PEA}_2\text{PbBr}_4$ system does not significantly alter the structure, increasing the order slightly as the 005 reflection is evident [see figure 4.8 (c)]. This result proves that the iPAm can be well tolerated within the 2D crystal structure.

Inspection of the intensity cuts along the q_z direction reveals the simultaneous presence of different phases for the $\text{PEA}_2(\text{Cs}_{0.75}\text{MA}_{0.25})\text{Pb}_2\text{Br}_7$ ($\langle n=2 \rangle$) neat film, with $n=1$ and $n=3$ being the most abundant (see figure 4.9). Similar to the 2D phase, the $\text{PEA}_2(\text{Cs}_{0.75}\text{MA}_{0.25})\text{Pb}_2\text{Br}_7$ film is also composed of crystallites strongly orientated with their 00 l planes parallel to the substrate [figure 4.8 (b)]. However, contrary to what was observed for the 2D phase, the $\langle n=2 \rangle$ phase structure is strongly perturbed by the addition of iPAm. Two main effects are observed when iPAm is added to the $\langle n=2 \rangle$ neat film. A change in the relative composition of the different phases is detected, as revealed by the change in the 001-peak intensity for the phases with different n observed along the q_z direction [(figure 4.9 (b)]. The addition of the iPAm causes a decrease in the $n=1$ and $n=3$ phases, in agreement with PL data. Furthermore, a significant increase of the fraction of crystallites with a random orientation upon addition of the iPAm is observed from the appearance of the Debye-Scherrer rings in the GIWAXS pattern of figure 4.8 (d). The crystallites with random orientation are mostly composed of $n=1$ and $n=3$ structure, while the $n=2$ retain high orientation.

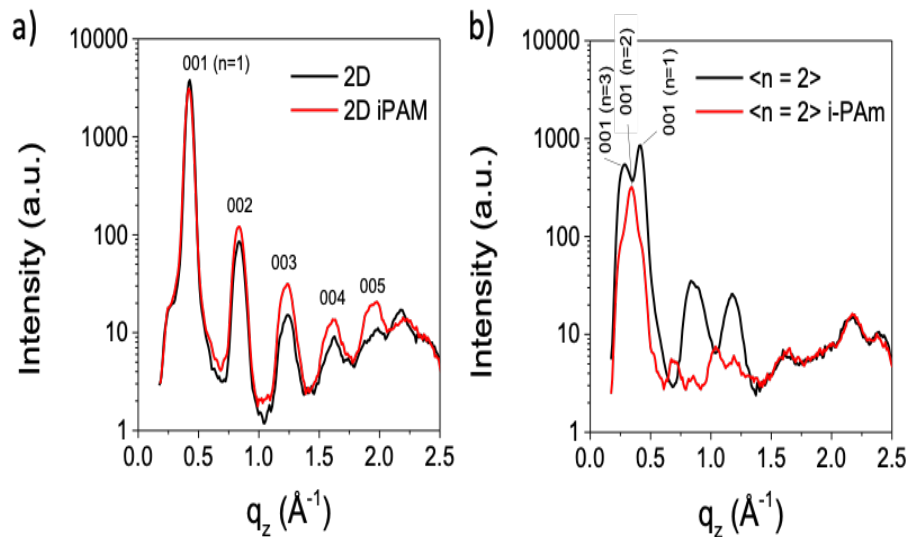


Figure 4.9 Comparison of the GIWAXS intensity cuts along the quasi vertical q_z direction for the 2D and the $\langle n=2 \rangle$ thin films without and with the iPAm addition.

It has been reported that crystallites with random orientation can improve the charge transport in the direction perpendicular to the perovskite film and, thus, led to higher efficiencies in light-emitting devices^[16] On the other hand, has also been shown that high orientation can be beneficial to enhance the radiative recombination of the carriers.^[17] Therefore, the results of the morphological characterization, together with those of the optical spectroscopies, suggest the possibility to have better device performance using the iPAm-modified perovskite film instead of the neat film for blue light-emitting diodes.

4.3.4 Device performance

Motivated for the results obtained from the optical, structural and morphological characterization, we then decided to fabricate PeLEDs .

PeLEDs with the $\langle n=2 \rangle$ iPAm-modified perovskites were fabricated using a device structure composed by ITO/PEDOT:PSS (35 nm) /quasi-2D perovskite (125 nm) /TPBi (40 nm) / LiF (1nm) /Al (80 nm) as depicted schematically in figure 4.10 (a). The energy alignment of the different materials composing the devices is depicted in figure 4.10 (b). The energy level for the quasi-2D perovskite was estimated according to previous reports on bromide-based multi-cation quasi-2D perovskites^[15]. It is also important to underline that the active layer is not a pure phase but a mixture of phases of different band-gap. As a reference, we also fabricated devices with neat $\langle n=2 \rangle$ RP phases with the aim of better understand the effect of the iPAm addition. The details of the device fabrication process can be found in the experimental section.

Devices' performances are summarized in figure 4.11. The colorimetric characteristics of several devices are calculated based on the EL spectra and plotted in the CIE 1931 color space diagram using as a reference the standard illuminant E [figure 4.11 (a)]. The current density–applied bias–luminance (JVL) characteristics for iPAm-modified and neat devices are displayed in figure 4.11 (b). Upon the addition of iPAm, the electrical properties of the diode are improved, with a decrease of the threshold voltage to 2.9 V with respect to 3.6 V of the neat sample and a general increase of the current in forward bias. Also, the luminance is practically one order of

magnitude higher for the iPAm LEDs with respect to the neat one. The maximum luminance reached for the iPAm device is 8260 cd m⁻² at an applied bias of 6.5 V (20.61mA/cm²) (at 7V JV is 24.85mA/cm²). After this point, the device experiences the typical roll-off behavior. For the neat PeLED, the maximum luminance reached is 2469 cd m⁻² at the tested bias of 7V (17.19 mA/cm²). The current efficiency at their maximum brightness of both devices was also evaluated as shown in figure 4.11(e), values of 38 cd/A (6.5 V) and 14.3 cd/A (7V) are obtained for iPAm-modified and neat PeLED, respectively. The EL spectra for the neat and iPAm-modified PeLEDs at 7V are in figure 4.11 (c), the electroluminescence for neat PeLED is located at 501 nm, while for the iPAm-modified relies on 481 nm. Small variations of the coordinates are obtained with slightly different deposition procedures as shown in figure 4.11 (a). The color coordinates, dominant wavelength, and color purity are resumed in table 4.4.

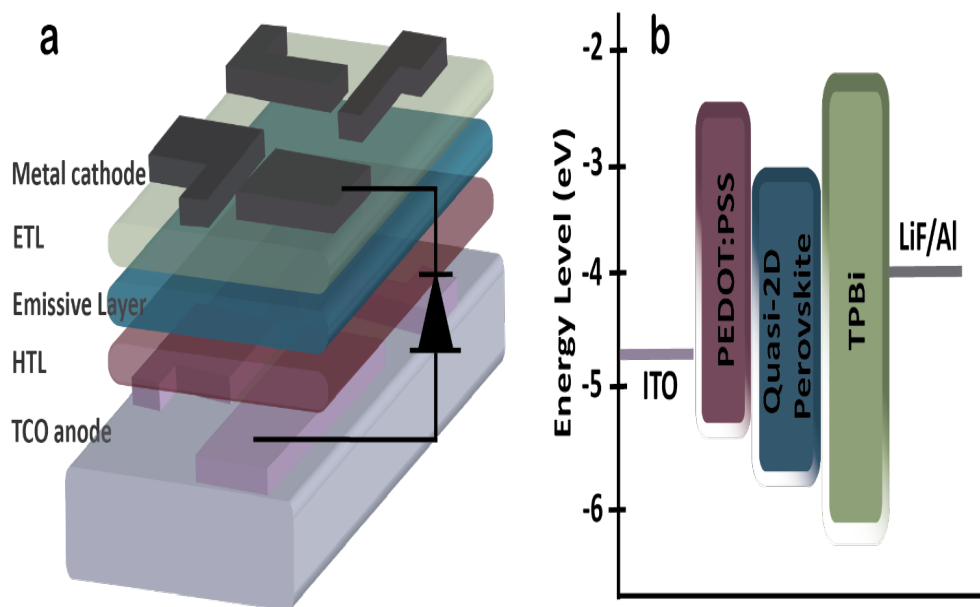


Figure 4.10. Schematic illustration of the structure of the perovskite LED (a) and the energy level alignment of the materials composing the device structure (b).

The *champion device* terminology is used for the samples that show the best efficiency performance, as it is not exclusively dependent on the emission properties but also on the electrical performances of the active layer. Our champion iPAm-modified PeLED displays the CIE chromaticity coordinates of $x=0.1092$ and $y=0.1738$, meeting the standard requirements

for the blue region, reaching a color purity of 88% in accordance with an FWHM of 25 nm. Furthermore, we have estimated a dominant-wavelength distribution color average for the evaluated iPAm PeLEDs [figure 4.11(a)]. The average dominant wavelength is 483 nm; it is represented by a blue dot at the locus curve. Similarly, the green dot at 501 represents the average wavelength of the neat perovskite PeLEDs. As mentioned earlier, while the neat devices show a very high reproducibility of color, the iPAm-modified one shows a larger variability, depending on the fabrication procedure.

Another important quality of LEDs is their color stability with different applied voltages. In figure 4.11 (d) are reported the EL spectra of one of the iPAm-modified champion devices at different applied bias, from 4.5 to 8 V, both the peak wavelength (481 nm), the shape, and the color purity of the electroluminescent is not perturbed. Importantly, the highest external quantum efficiency (EQE) reached by the iPAm PeLEDs is 5.2%. While the maximum EQE measured for the neat device is 1.5%.

The role of iPAm is essential to achieve high efficiency, as mentioned above the addition of this organic cation has the fundamental role of hindering the energy transfer, which clearly has the expected effect in the blue EL spectra (483 nm average) respect to the (501 nm average) of the neat device. However, it appears to have also a very important role in the electrical behavior of the active layer. Structural investigations demonstrated that iPAm breaks the crystallization and scramble the orientation of the crystallites of large n values, this improves the transport of the active layer and allows recombination to occur in the low dimensional domains. In conclusion, it is important to underline that our iPAm-modified device is among the highest EQE blue PeLEDs demonstrated up until now, with color purity of 88% and record luminance of 8260 cd m⁻² at 6.5 V.

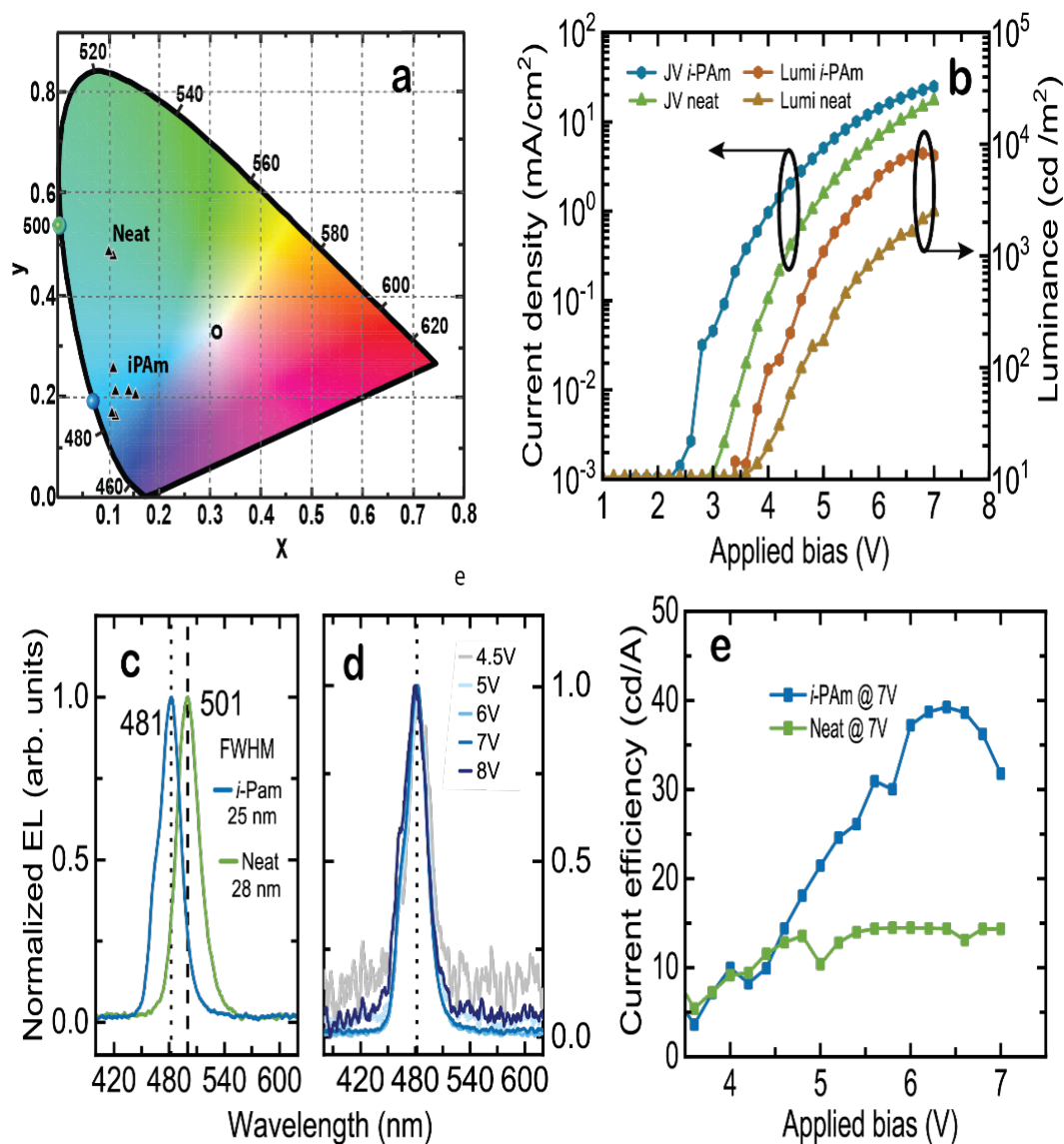


Figure 4.11 Performance of PeLEDs. (a) CIE color coordinates of different types of devices investigated (b) JVL curves of one the best performing devices (c) EL of PeLEDs using as emissive layer $\langle n=2 \rangle$ neat and with iPAm the spectra are recorded with the device bias at 7V, (d) EL spectra of the blue-emitting LED at different bias, and (e) current efficiency of $\langle n=2 \rangle$ neat and with iPAm PeLEDs.

The role of iPAm is essential to achieve high efficiency, as mentioned above the addition of this organic cation has the fundamental role of hindering the energy transfer, which clearly has the expected effect in the blue EL spectra (483 nm average) respect to the (501 nm average) of the neat device. However, it appears to have also a very important role in the electrical behavior

of the active layer. Structural investigations demonstrated that iPAm breaks the crystallization and scramble the orientation of the crystallites of large n values, this improves the transport of the active layer and allows recombination to occur in the low dimensional domains. In conclusion, it is important to underline that our iPAm-modified device is among the highest EQE blue PeLEDs demonstrated up until now, with color purity of 88% and record luminance of 8260 cd m⁻² at 6.5 V.

Table 4.4 Colorimetric characteristics for neat and iPAm-modified PeLEDs using as reference the standard illuminant E.

PeLED	Coordinates	Dominant wavelength	Color purity
Neat champion	(0.1105,0.4710)	501 nm	66%
Neat (ii)	(0.1003,0.4679)	500 nm	70%
iPAm champion	(0.1092, 0.1738)	481 nm	88%
iPAm (ii)	(0.1096,0.2675)	488 nm	79%
iPAm (iii)	(0.1576, 0.2030)	481 nm	69%
iPAm (iv)	(0.1148, 0.2146)	484 nm	82%
iPAm (v)	(0.1415, 0.2148)	483 nm	73%

4.4 Conclusions

Rudlesden-Popper perovskite phases of nominal composition PEA₂(Cs_{0.75}MA_{0.25})Pb₂Br₇ with and without, the addition of the isopropylammonium additive were demonstrated to emit in the wavelength range around 480 nm and 500 nm, respectively. The sample with isopropylammonium, when deposited on a PEDOT:PSS coated substrate, displays an exceptional PLQY as high as 64%. Cross-correlation of the optical and structural investigations indicate that the RP phase is composed of domains of $n=3$ phases surrounded by higher dimensionality phases, which allow the efficient transport of charge carriers towards the low dimensional domains. Interestingly, the funneling of the photoexcitations towards the low

dimensional phases is blocked in samples using the isopropylammonium additive, mostly due to the random orientation of very small crystalline domains. All these features of this new RP phase allowed us to fabricate LEDs emitting at an average wavelength of 483 nm, with FWHM of the electroluminescence of 25 nm and an external quantum efficiency up to 6%.

Our results demonstrate an opportunity to achieve high-efficiency LEDs in the blue spectra range by engineering Ruddlesden-Popper phases.

4.5 References

- [1] O. Almora, D. Baran, G. C. Bazan, C. Berger, C. I. Cabrera, K. R. Catchpole, S. Erten-Ela, F. Guo, J. Hauch, A. W. Y. Ho-Baillie, T. J. Jacobsson, R. A. J. Janssen, T. Kirchartz, N. Kopidakis, Y. Li, M. A. Loi, R. R. Lunt, X. Mathew, M. D. McGehee, J. Min, D. B. Mitzi, M. K. Nazeeruddin, J. Nelson, A. F. Nogueira, U. W. Paetzold, N. G. Park, B. P. Rand, U. Rau, H. J. Snaith, E. Unger, L. Vaillant-Roca, H. L. Yip, C. J. Brabec, *Adv. Energy Mater.* **2021**, *11*, 2002774.
- [2] NREL's Best Research-Cell Efficiencies Chart, **2021**.
- [3] K. Lin, J. Xing, L. N. Quan, F. P. G. de Arquer, X. Gong, J. Lu, L. Xie, W. Zhao, D. Zhang, C. Yan, W. Li, X. Liu, Y. Lu, J. Kirman, E. H. Sargent, Q. Xiong, Z. Wei, *Nature* **2018**, *562*, 245.
- [4] Y. H. Kim, S. Kim, A. Kakekhani, J. Park, J. Park, Y. H. Lee, H. Xu, S. Nagane, R. B. Wexler, D. H. Kim, S. H. Jo, L. Martínez-Sarti, P. Tan, A. Sadhanala, G. S. Park, Y. W. Kim, B. Hu, H. J. Bolink, S. Yoo, R. H. Friend, A. M. Rappe, T. W. Lee, *Nat. Photonics* **2021**, *15*, 148.
- [5] Y. Cao, N. Wang, H. Tian, J. Guo, Y. Wei, H. Chen, Y. Miao, W. Zou, K. Pan, Y. He, H. Cao, Y. Ke, M. Xu, Y. Wang, M. Yang, K. Du, Z. Fu, D. Kong, D. Dai, Y. Jin, G. Li, H. Li, Q. Peng, J. Wang, W. Huang, *Nature* **2018**, *562*, 249.
- [6] Y. Dong, Y. K. Wang, F. Yuan, A. Johnston, Y. Liu, D. Ma, M. J. Choi, B. Chen, M. Chekini, S. W. Baek, L. K. Sagar, J. Fan, Y. Hou, M. Wu, S. Lee, B. Sun, S. Hoogland, R. Quintero-Bermudez, H. Ebe, P. Todorovic, F. Dinic, P. Li, H. T. Kung, M. I. Saidaminov, E. Kumacheva, E. Spiecker, L. S. Liao, O. Voznyy, Z. H. Lu, E. H. Sargent, *Nat. Nanotechnol.* **2020**, *15*, 668.
- [7] L. Protesescu, S. Yakunin, M. I. Bodnarchuk, F. Krieg, R. Caputo, C. H. Hendon, R. X. Yang, A. Walsh, M. V. Kovalenko, *Nano Lett.* **2015**, *15*, 3692.
- [8] S. Gonzalez-Carrero, L. Francés-Soriano, M. González-Béjar, S. Agouram, R. E. Galian, J. Pérez-Prieto, *Small* **2016**, *12*, 5245.
- [9] S. Shao, J. Liu, G. Portale, H.-H. Fang, G. R. Blake, G. H. ten Brink, L. J. A. Koster, M. A. Loi, *Adv. Energy Mater.* **2018**, *8*, 1702019.
- [10] L. Zhang, C. Sun, T. He, Y. Jiang, J. Wei, Y. Huang, M. Yuan, *Light Sci. Appl.* **2021**, *10*, 6.
- [11] Q. Wang, S. Shao, B. Xu, H. Duim, J. Dong, S. Adjokatse, G. Portale, J. Hou, M. Saba, M. A. Loi, *ACS Appl. Mater. Interfaces* **2020**, *12*, 29505.

- [12] L. N. Quan, Y. Zhao, F. P. García De Arquer, R. Sabatini, G. Walters, O. Voznyy, R. Comin, Y. Li, J. Z. Fan, H. Tan, J. Pan, M. Yuan, O. M. Bakr, Z. Lu, D. H. Kim, E. H. Sargent, *Nano Lett.* **2017**, *17*, 3701.
- [13] J. Dong, S. Shao, S. Kahmann, A. J. Rommens, D. Hermida-Merino, G. H. ten Brink, M. A. Loi, G. Portale, *Adv. Funct. Mater.* **2020**, *30*, 2001294.
- [14] S. Shao, H. Duim, Q. Wang, B. Xu, J. Dong, S. Adjokatse, G. R. Blake, L. Protesescu, G. Portale, J. Hou, M. Saba, M. A. Loi, *ACS Energy Lett.* **2020**, *5*, 39.
- [15] K. Shibuya, M. Koshimizu, F. Nishikido, H. Saito, S. Kishimoto, *Acta Crystallogr. Sect. E Struct. Reports Online* **2009**, *65*, m1323.
- [16] H. Lee, H. Kim, H. Cho, W. Cha, Y. Hong, Y. Kim, A. Sadhanala, V. Venugopalan, J. S. Kim, J. W. Choi, C. Lee, D. Kim, H. Yang, R. H. Friend, T. Lee, *Adv. Funct. Mater.* **2019**, *29*, 1901225.
- [17] L. Lei, D. Seyitliyev, S. Stuard, J. Mendes, Q. Dong, X. Fu, Y. Chen, S. He, X. Yi, L. Zhu, C. Chang, H. Ade, K. Gundogdu, F. So, *Adv. Mater.* **2020**, *32*, 1906571.

Curriculum Vitae

Personal Details

Born Martha Judith Rivera Medina
2 June 1989
In Veracruz, Mexico

Education

Nov 2018 – Mar 2021 Ph.D. Candidate
Photophysics and Optoelectronics group
Zernike Institute for Advanced Materials
University of Groningen, the Netherlands

Ago 2016 – Sep 2021 Ph.D. Candidate
Condense matter and Cryogenics department
Materials Research Institute
National Autonomous University of Mexico, Mexico

Feb 2014 – Jul 2016 M.Sc. Materials Engineering
Condense matter and cryogenics Department
Materials Research Institute
National Autonomous University of Mexico, Mexico

Aug 2008 – Dec 2012 B.Sc. Chemical Engineering
Faculty of Engineering
Veracruz University, Mexico

Conferences Attended

2020 Virtual MRS Spring/Fall Meeting (Talk)

2020 Dutch Physics Congress: Physics @ Veldhoven, the Netherlands (Talk)

2018 Student Chapter of the Mexican Material Research Society – UNAM Annual reunion, CDMX Mexico (Talk)

2017 International Material Research Congress, Cancun Mexico (Poster)

- 2017 Next-Gen: PV materials conference, Groningen the Netherlands (Attendance by invitation)
- 2017 Student Chapter of the Mexican Material Research Society – UNAM Annual reunion, CDMX Mexico (Talk)

Publications

1. **M.J. Rivera-Medina**, L. Di Mario, G. Portale, S. Kahmann, A. Mura, J. Xi, J.C. Alonso-Huitrón, M.A. Loi (In preparation).
2. **M.J. Rivera-Medina**, A. Carillo-Verduzco, A. Rodríguez-Gómez, M.A. Loi, J.C. Alonso-Huitrón, *Mater. Chem. Phys.* 2021, 270, 124866.
3. S. Kahmann, H. Duim, H.H. Fang, S. Adjokatse, **M.J. Rivera-Medina**, M. Pitaro, P. Plochocka, M.A. Loi, *Adv. Funct. Mater.* 2021, 2103778.
4. V.H. López-Lugo, **M.J. Rivera-Medina**, J.C. Alonso-Huitrón, *Mater. Res. Express* 2021, 8, 036406.
5. B. Juárez-García, J. González-Gutiérrez, **M.J. Rivera-Medina**, A. García-Valenzuela, J.C. Alonso-Huitrón, *Appl. Opt.* 2019, 58, 5179.
6. **M.J. Rivera-Medina**, J. Hernández-Torres, J.L. Boldú-Olaizola, J. Barriento-Rentería, J.M. Hernández-Alcántara, V. Jancik, J.C. Alonso-, *RSC Adv.* 2016, 6, 107613.
7. **M.J. Rivera-Medina**, E.B. Ramírez, B. Juárez-García, J. González-Gutiérrez, J.M. García-León, J.C. Alonso-Huitrón, *Thin Solid Films* 2016, 605, 108.